INAUGURAL - DISSERTATION

zur

Erlangung der Doktorwürde

der

Naturwissenschaftlich - Mathematischen

Gesamtfakultät

der Ruprecht - Karls - Universität

Heidelberg

vorgelegt von

Master-Physiker

Ahmed Aboud Mahmoud Mohamed El Gendy

geboren in Alexandria - Ägypten

Tag der mündlichen Prüfung: 15.06.2011

Carbon-coated Nanomagnets:

Synthesis, Characterization And Feasibility

For Magnetic Hyperthermia

Gutachter:

Prof. Dr. Rüdiger Klingeler

Prof. Dr. Günter Reiss

Kohlenstoff-ummantelte Nanomagnete: Synthese, Eigenschaften und Potenzial für magnetische Hyperthermie:

Die Arbeit beschäftigt sich mit der Entwicklung neuer Synthesemethoden zur Herstellung Kohlenstoff-ummantelter nanoskaliger Magnete und der detaillierten Charakterisierung dieser Materialien hinsichtlich ihrer Struktur, Morphologie und magnetischen Eigenschaften. Für die Synthese wurde die Methode der Chemischen Gasphasenabscheidung unter hohem Druck (HPCVD) eingesetzt, wobei core/shell Materialien mit unterschiedlichen magnetischen Kernen wie Fe, Co, Ni, FeRu, CoRu, NiRu, NiPt und CoPt hergestellt wurden. Die genaue strukturelle und morphologische Charakterisierung der Materialien erfolgte mittels Transmissionselektronenmikroskopie, Energiedispersiver Röntgenspektroskopie sowie Röntgendiffraktometrie. Einen Schwerpunkt der Arbeit bildet die Untersuchung der magnetischen Eigenschaften der Materialien und der Zusammenhänge der Materialparameter wie z.B. dem Durchmesser der magnetischen Kerne oder im Falle von Legierungen ihrer Zusammensetzung. Durch die geeignete Wahl der Syntheseparameter konnten diese Eigenschaften und somit die magnetischen Funktionalitäten gezielt eingestellt werden. Ein Vorteil der Kohlenstoffhüllen besteht in dem Oxidationsschutz für die ummantelten Kerne, so dass sich die hier hergestellten Materialien besonders für Anwendungen in biologischen Umgebungen eignen. In der Arbeit wurde daher die Eignung der Materialien für die magnetische Hyperthermie als einer wichtigen Anwendung magnetischer Nanopartikel untersucht.

Carbon-coated Nanomagnets: Synthesis, Characterization and Feasibility for magnetic Hyperthermia:

This work addresses the development of novel synthesis procedures for carbon-coated magnetic nanoparticles and their detailed characterization regarding structure, morphology, and magnetic properties. To be specific, the high pressure chemical vapour deposition technique (HPCVD) has been applied to successfully produce carbon-coated nanoparticles with various magnetic core materials, such as Fe, Co, Ni, FeRu, CoRu, NiRu, NiPt, and CoPt. The morphological and structural characterization of the materials has been done by means of transmission electron microscopy, energy dispersive X-ray spectroscopy and X-ray diffraction. Particular emphasis has been given to the investigation of the magnetic properties and its dependence on, e.g., core size and stoichiometry of the core alloys, which can be tailored by adjusting the synthesis conditions. A particular advantage of carbon-coated nanomagnets is oxidation protection of the magnetic core material which implies feasibility for biomedical applications. Here, the feasibility for magnetic hyperthemia therapies is exploited by investigating induced heating under applied alternating magnetic fields.

Contents

Introduction

Small is beautiful and powerful. This conclusion is evident if one considers the aim of developing smaller and hence more efficient devices. The most fascinating and promising aspects of materials and devices becoming smaller, however, are not associated with mere size reduction only but are related to fundamentally novel physical properties and effects appearing when decreasing the lengths scales of materials down to the nanometer scale. In this sense, reducing the dimensions of well-known bulk materials opens completely new fields in basic and applied research. It is the fundamentally different physical and chemical properties of nano-sized materials which not only promise new nanotechnological applications but also attract scientists' attention to their fundamental scientific importance. In recent years, great progress has been made in this respect and nano-sized materials with novel properties have already found or exhibit at least a great potential for applications in the fields of, e.g., optics, magnetism, electricity, catalysis, and biomedicine.

Based on all these developments, in the last decades, new expressions with the prefix 'nano' have been added into the scientific dictionary such as nanoparticle, nanostructure, nanotechnology, nanomaterial, nanocluster, nanochemistry, nanocolloids, and nanoreactor. Furthermore, a series of new journals are devoted particularly to this subject. Articles with the corresponding names have appeared, 'nano'-specialised institutes and laboratories have been founded; and numerous conferences

are held. A precondition for all these developments is the ability to fabricate, to investigate and to handle such nano-sized entities. Indeed, there have been a number of significant developments that enabled scientists to explore the world of nanoscale objects. These developments include various types of microscopes, techniques for nanomanipulation, and methods of nanofabrication.

Currently, unique physical properties of nanoparticles are under intensive research. One of the materials properties strongly affected by size reduction is the magnetic response. For example, the magnetization (per atom) and the magnetic anisotropy of Co nanoparticles [1] can be greater than their related bulk specimens. The enhancement in the magnetization can be ascribed to the surface atoms which become the dominant phase as size decreases and for which the electronic structure can be varied because of the different symmetry compared to the bulk. In addition, the surface anisotropy is the responsible for the enhancement of the magnetic anisotropy of the magnetic nanoparticles, i.e. the lower symmetry of surface atomic sites leads to an enhanced anisotropy.

As a result of their novel magnetic properties, magnetic nanoparticles offer attractive potentials not only for fundamental science value but also for technological innovations. One possible field of application of magnetic nanomaterials is their usage in biology and medicine. One example is the well-established field of magnetic resonance imaging (MRI), where effects of nanoscaled magnets on the proton susceptibility are exploited to increase the contrast in nuclear magnetic resonance imaging. The applicability of such methods relies on the fact that magnetic fields only very weakly interact with organic materials and do not cause known side effects. On the other hand, once magnetic nanoparticles are internalized in a particular organic environment such as, e.g., the human body, external magnetic fields can be applied in order to address these magnetic agents. In general, in addition to imaging methods mentioned above, external static magnetic fields can fix ferromagnetic nanoparticles at a precise position, gradient fields can move them and alternating magnetic fields

will yield heating of the nanoparticles. It is the latter effect that opens a completely new route for anti-cancer therapies: Once internalized in tumor tissue, such a heating effect can be utilized for so-called 'hyperthermia', i.e. a therapeutic anti-cancer treatment which raises the temperature of tumor tissue in-vivo. This method applies the fact that a cancer cell-killing effect is caused when a temperature above 41-42 °C is maintained in the target volume. At higher temperatures, the effect is called 'thermoablation'. One outstanding example of the use of ferromagnetic nanoparticles is 'magnetic fluid hyperthermia' (MFH). In MFH therapy, magnetic nanoparticles are infiltrated deep into tumor tissue and inductively heated by applying alternating magnetic fields [2-7].

When aiming at realizing the promises of applied nanoscience, however, the production of uniform nanoparticles with controlled particle size is still one of the main challenges. Therefore, the thesis at hand focuses on the synthesis of such nanoparticles. Any application in biological environment (but also others) however demands that the material is particularly protected against oxidation and degradation. One promising approach is the encapsulation of the functional materials inside carbon shells. Carbon shells strongly protect encapsulates and tend to be bio-compatible. Moreover, biomedical applications demand the functionalization of the nanoparticles' outer shells either in order to disperse them in aqueous solutions or to attach e.g. entities with additional functionalities such as antigens. The work at hand hence presents novel techniques for fabrication of core/shell magnetic nanoparticles, their detailed structural, morphological and magnetic characterization, as well as studies on their feasibility for magnetic hyperthermia.

The work contains seven chapters. In chapter 1, the fundamentals of magnetic nanoparticles starting from a general overview on their magnetic behaviour is introduced. In particular, ferromagnetic and superparamagnetic properties as well as single domain theory, magnetic anistropy and interparticle interaction are explained. In the second chapter, an overview about the synthesis methods for nanoparticles

along with a discussion of advantages and disadvantages of the respective methods is presented. In addition, the thermodynamics of nanoparticles growth in the gas phase is introduced. Chapter 3 highlights briefly applications of magnetic nanoparticles with a focus on magnetic hyperthermia/thermoablation which is the main application addressed in this work. The fourth chapter covers the experimental setup which is used for synthesis and characterization of the samples in this thesis.

The following chapters include the results and their discussion. Chapter 5 contains the synthesis and detailed investigation of carbon coated Fe, Co, and Ni nanoparticles, i.e. Fe@C, Co@C, and Ni@C. These investigations reveal formation of spherical magnetic core of Fe, Co, and Ni nanoparticles coated with defined carbon shells with average particle size in the range of 20-30 nm. In addition, the magnetic properties of the synthesized samples under direct or alternating magnetic field are studied.

The sixth chapter focuses on the synthesis and the characterization of carbon coated FeRu, CoRu, and NiRu nanoalloys. Here the effect of the synthesis pressure variation on the properties of the samples is examined resulting in production of different alloy compositions and carbon to metal ratios without any observed change in the particle size. The formation of spherical carbon coated nanoalloys with small size core in the range of 6-13 nm is observed. In addition, the magnetic properties for all synthesized samples are investigated.

The seventh chapter is devoted to the synthesis of NiPt@C and CoPt@C nanocapsules. In this chapter, the effect of synthesis sublimation temperature variation on the properties of the synthesized materials is studied. The results imply the formation of spherical nanocapsules with different alloy composition, carbon to metal ratio and particle size within range of 2-20 nm plus narrow size distribution. In addition, the magnetic properties are revealed for all synthesized NiPt@C and CoPt@C nanocapsules.

Finally the thesis ends with the summary, the references, and the list of publications.

Chapter 1

Magnetic nanoparticles

Nanoparticles can be defined as ultrafine particles with a size at the nanometer scale. The origin of the prefix nano comes from the Greek word for *dwarf*, and hence nanoscience (the commonly used term nowadays for nanoscale science) deals with the study of atoms, molecules and nanoscale particles in a world that is measured in nanometres or 10^{-9} m. The development of nanoscience can be traced to the time of the Greeks and Democritus in 5th century B.C., when people thought that matter could be broken down to an indestructible basic components called atoms.

The modern origins of nanotechnology are commonly attributed to R. Feynman, who on December 29th 1959 at Caltech, delivered his talk 'There´s Plenty of Room at the Bottom'. He described the possibility of putting a tiny 'mechanical surgeon' inside the blood vessel that could locate and do corrective localized surgery. He predicted that the principles of physics should allow the possibility of manipulating things atom by atom. Feynman described such atomic scale fabrication as a bottom-up approach. In contrast, he described the top-down approach that is commonly used in manufacturing. For example in silicon integrated circuit (IC) fabrication, tiny transistors are built up and connected in complex circuits starting from a bare silicon wafer. Such top-down methods in wafer fabrication involve processes such as thin film deposition, lithography, and etching. Using such methods, the researchers

have been able to fabricate a remarkable variety of electronics devices and machinery. Therefore, one can conclude a definition for nanotechnology which can be the design and fabrication of materials, devices and systems with control at nanometer dimensions, typically having dimensions of up to 100 nm.

Because of the widespread applications of magnetic nanoparticles, in biomedical, biotechnology, engineering, material science and environmental areas [1-8], much attention has been paid to the preparation of different kinds of magnetic nanoparticles. The first nano-sized magnetic particles (Fe_3O_4) were developed in 1960 by NASA [8]. The particles were made by ball milling in the presence of a surface-active agent (surfactant) such as transformer oil, water or kerocene and the liquid carrier. Such obtained dispersions are called magnetic fluids or ferrofluids [8]. The term ferrofluid is derived from the 'ferromagnetic' behavior of fluids containing magnetic nanoparticles when exposed to a magnetic field.

Generally, magnetic nanoparticles are inside us and everywhere around us, interstellar space, lunar samples, and meteorites contain magnetic nanoparticles. For example the most common iron storage protein ferritin $(FeOOH)_n$ containing magnetic nanoparticles is present in almost every cell of plants, animals and humans. The human brain contains over 10^8 magnetic nanoparticles of magnetite-maghemite per gram of tissue [9].

The chapter at hand provides an overview for fundamentals of magnetism and a description of important issues relative to magnetism on the nanoscale represented by superparamagnetism, single domain, inter-particle interaction and magnetic anisotropy.

1.1   Fundamental of magnetism

There are two atomic origins of magnetism which contribute to the magnetization of magnetic substances: orbital motion and the spin of electrons. The volume magneti-

zation M is defined as the magnetic moment per unit volume. In free space (vacuum) no magnetization occurs. When a material is placed in a magnetic field H, the flux density (or magnetic induction B) is given by

$$B = \mu_0 (H + M) \tag{1.1}$$

where $\mu_0 = 4\pi \times 10^{-7}$ H/m is the permeability of free space. In the special case that the magnetization is parallel to the external magnetic field, the material is called linear material and the ratio between M and H is called the magnetic susceptibility χ of the material as given by [12],

$$M = \chi H. \tag{1.2}$$

By means of the magnetic susceptibility, the magnetic behavior of any material can be classified into diamagnetic, paramagnetic, ferromagnetic, ferrimagnetic, and antiferromagnetic according to the arrangement of their magnetic moments in the absence and presence of an external magnetic field (Fig. 1.1) [10]. These different types of magnetism can be described briefly as following:

Diamagnetism is a weak effect. The relative magnetic susceptibility of such a diamagnetic material is negative ($\chi < 0$) and small. For a diamagnetic substance, a magnetic field induces a magnetic moment which opposes the applied magnetic field that caused it (Fig. 1.1). The mechanism by which the magnetization is induced opposite to the magnetic field is the acceleration of the orbital electrons by electromagnetic induction caused by the penetration of the external magnetic field to the orbit. According to Lenz's law, the magnetic flux produced by this acceleration of an orbital electron is always opposite to the change in the external magnetic field, so that the susceptibility is negative. Diamagnetism is present in all materials, but it is a weak effect which can be ignored in the presence of larger effects such as ferromagnetism [11, 12].

In the **Paramagnetic** regime where no long magnetic order occurs (Fig. 1.1), the magnetic response is described in terms of the so-called Curie-Weiss law, $\chi =$
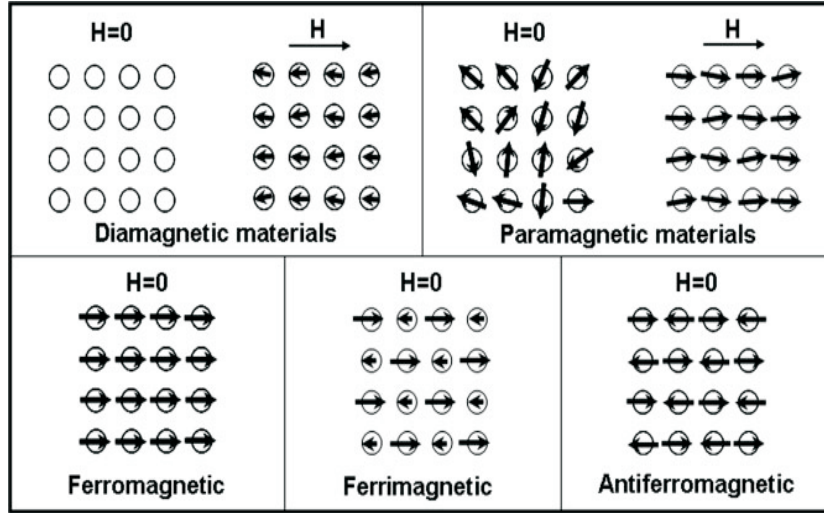
Figure 1.1: Schematic which illustrates the arrangements of magnetic moments for five different magnetic behaviors in the absence or presence of an external magnetic field (H) [10].

$C/(T-\theta)$, where C is the Curie constant and the Curie-Weiss constant θ is a measure for the magnetic interactions [12].

In contrast to diamagnetism and paramagnetism, there exist several ordering patterns which specify the vector arrangement of magnetic moments. The interatomic exchange between magnetic moments localized on individual atoms is well described by the Heisenberg interactions J_{ij} between atomic spins. Depending on the respective positive or negative sign of the J_{ij}, the exchange favors a parallel or antiparallel alignment of neighboring spins, which often translates into **ferromagnetic**, **ferrimagnetic**, or **antiferromagnetic** order, respectively (Fig. 1.1) [11, 12].

The ferromagnetic materials investigated in the thesis at hand are metallic but as will be pointed out below, exchange interaction yields spin polarization and long-range ferromagnetic order

1.2   Exchange interaction

Exchange interaction is the most important and relevant interaction between the magnetic moments in a solid and potentially causing various ordering phenomena. The exchange interaction actually arises from the quantum mechanics. This interaction usually lies at the heart of long-range magnetic order. The nature and magnitude of the exchange interaction between neighboring magnetic ions usually determines how the individual moments will align. For explaining the exchange interaction let us consider two electrons which have spatial coordinates r_1 and r_2, each one being described by the single electron state, $\psi_a(r_1)$ and $\psi_b(r_2)$, respectively, so that the joint wave function may be expressed as the product of those individual electron states $\psi_a(r_1)\psi_b(r_2)$. Since the Pauli principle forbids the double occupancy of any orbital by electrons of parallel spin, electrons with parallel spins are likely to be further apart in space than those with antiparallel spins. The joint wave function has to be antisymmetric upon the exchange of any two electrons. This means that only those allowed states corresponding to the antisymmetric singlet state ($\uparrow\downarrow$) and the symmetric triplet state ($\uparrow\uparrow$), in the spin part of the wave function, must be associated to the symmetric and antisymmetric real-space of the wave function. The wave functions for the singlet and triplet case including spatial and spin part take the form:

$$\Psi_S \sim [\psi_a(r_1)\psi_b(r_2) + \psi_a(r_2)\psi_b(r_1)] \tag{1.3}$$

$$\Psi_T \sim [\psi_a(r_1)\psi_b(r_2) - \psi_a(r_2)\psi_b(r_1)] \tag{1.4}$$

The exchange is estimated by comparing the total energies for the singlet and triplet two-electron wave functions. Evaluating the energy, $E = \int \Psi^\star H \Psi dr_1 dr_2$, for Eq. 1.3 and 1.4, the exchange constant $J = (E_S - E_T)/2$ points out the energetically most favorable state in the system. A positive J means $E_S > E_T$ and favors ferromagnetic spin coupling ($\uparrow\uparrow$), while a negative J value with $E_S < E_T$ gives account of antiferromagnetic coupled spins ($\uparrow\downarrow$). Considering here that the magnetic moment

is caused by spin motion of electrons, the Hamiltonian for the coupling of two spins reads $\mathcal{H} = AS_1 \cdot S_2$, and the equivalence of A in terms of the difference between singlet and triplet states [11], the spin dependent term in the effective Hamiltonian can be written as:

$$\mathcal{H}^{spin} = -(E_S - E_T)S_1 \cdot S_2 = -2JS_1 \cdot S_2 \tag{1.5}$$

Although this apparently simple equation becomes more complex when generalizing to a many-particles system, in the early days of quantum mechanics, it was shown by Heisenberg (1928) that this quantum-mechanical exchange interaction might be extended to all nearest neighbours atomic spins in the crystal lattice. This then favors the creation of an internal magnetic field. The generalization is given by:

$$\mathcal{H} = -\sum_{ij} J_{ij} S_i \cdot S_j \tag{1.6}$$

where J_{ij} is the exchange constant between the ith and j^{th} spins. The factor 2 is omitted because the summation includes each pair of spin twice. Often J_{ij} has the same magnitude for all nearest-neighbour spins and is zero otherwise. This allows to assume a constant value $J_{ij} = J$ for the exchange in Eq. 1.6.

1.3   Ferromagnetism

The microscopic theory of ferromagnetism started with Weiss [11] who in 1907 postulated his famous molecular field model. Although formulated before the advent of quantum mechanics, he already assumed discrete energy levels associated with respective values for magnetic moments (angular momenta). To explain the spontaneous alignment of the elementary magnetic moments, he postulated the existence of an internal (molecular) field which should represent the unknown interaction between these moments. Later this interaction was found to be the exchange interaction which is of entirely quantum-mechanical origin.

In ferromagnets, magnetic moments at neighboring sites point into the same direction. This effect is generally due to the exchange interactions which has been discussed in the previous section. When the ferromagnet is put in an applied magnetic field, the suitable hamiltonian to solve is

$$\mathcal{H} = 2\sum_{ij} J_{ij} S_i \cdot S_j + g\mu_B \sum_j S_i \cdot B, \tag{1.7}$$

and the exchange constants for the nearest neighbors will be positive in this case. The first term on the right is the Heisenberg exchange energy. The second term on the right is the Zeeman energy where g is a constant known as the g-factor. For simplification, let us assume a system in which there is no orbital angular momentum.

Making an approximation for Eq. 1.7, a definition of an effective molecular field at the ith site is given by

$$B_{mf} = 2\sum_j J_{ij} S_j. \tag{1.8}$$

However, the exchange interaction can be replaced by an effective molecular field B_{mf} produced by the neighbouring spins. Therefore, the effective Hamiltonian can now be written as:

$$\mathcal{H} = g\mu_B \sum_i S_j \cdot (B + B_{\text{mf}}). \tag{1.9}$$

From Eq. 1.9 the Hamiltonian looks like that for a paramagnet in a magnetic field $B + B_{\text{mf}}$. For a ferromagnet the molecular field will act so as to align neighboring magnetic moments. This is because the dominant exchange interactions are positive. Since the molecular field includes the effects of all spins j$\neq$ i on S_i, one can assume that $B = \lambda M$ where λ is a constant which parametrizes the strength of the molecular field as a function of the magnetization. For a ferromagnet, $\lambda > 0$, and due to the large Coulomb energy involved in the exchange interaction, the molecular field is often found to be extremely large in ferromagnets. At low temperature, the moments can be aligned by the internal molecular field, even without any applied field being present. As the temperature is raised, the thermal fluctuations begin to

progressively destroy the magnetization and at a critical temperature the order will be destroyed. The critical temperature is known as Curie temperature T_C and the magnetic susceptibility is described by the Curie Weiss law ($\chi = C/(T - \theta)$).

1.4   Itinerant ferromagnetism

In the previous section the properties of isolated and localized magnetic moments have been discussed. But this is not always the case in the transition metal materials which are the focus of this thesis. In the transition metals ($3d$ series), the magnetic moments observed in these elements, their compounds, and alloys, generally differ markedly from those of the free atoms or isolated ions. The reason is that the valence electrons now propagate throughout the material, and their wave functions are very different from those in the isolated atom. Metals exhibit conduction electrons which are delocalized. These electrons (so-called itinerant electrons) can move nearly free inside the metal [11, 12].

For example, the magnetic moment of iron per iron atom in the solid state amounts to $2.2\mu_B$. It is not possible to understand the non-integral value on the basis of localized magnetic moments. This situation can be described by band or itinerant ferromagnetism in which the magnetization is due to spontaneously spin split bands. One approach for the explanation is given by the molecular field theory. All spins are influenced by an average exchange field λM which is produced by all their neighbors. In a metal, the molecular field can magnetize the electron gas because of the Pauli paramagnetism χ^{Pauli}. The resulting magnetization of the electron gas M can be responsible for the molecular field. This positive feedback may lead to spontaneous magnetization if the λ and χ^{Pauli} are both large enough. Thus, one has to look whether it is possible to reduce the energy of a system if it becomes ferromagnetic without applying an external magnetic field. This situation can be realized by a shift of electrons at the Fermi surface from spin down into spin
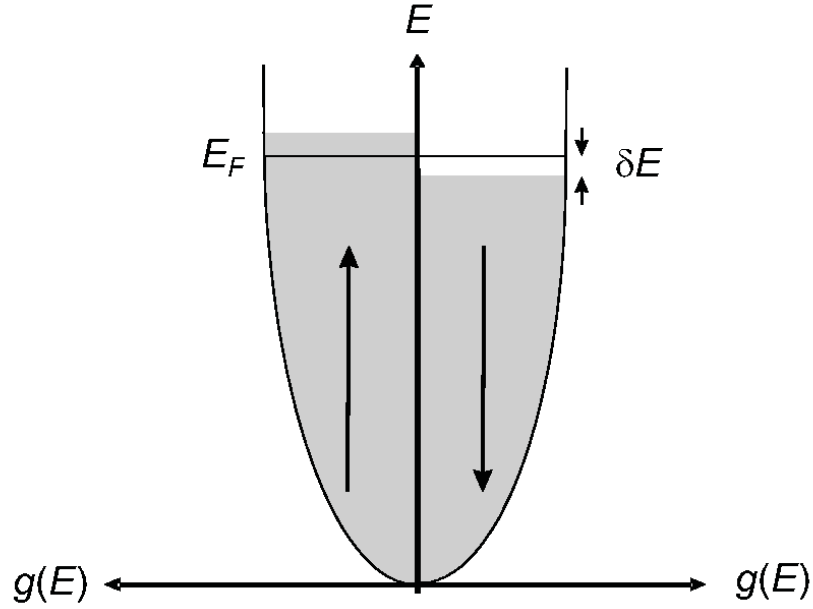
Figure 1.2: Density of states for spin up and spin down electrons exhibiting a spontaneous spin splitting without applying an external magnetic field [12].

up bands. This means that spin down electrons with energies between E_F-δE and E_{F} (Fermi energy) must perform a spin-flip placing them in the spin up band with energies between $E_{\mathrm{F}}+\delta E$ and E_{F} (Fig. 1.2). The energy gain per electron amounts to δE and the number of moved electrons is $g(E_{\mathrm{F}})\delta E/2$. Therefore, the increase of kinetic energy is given by:

$$\Delta E_{\mathrm{K.E}} = \frac{1}{2}g(E_{\mathrm{F}})(\delta E)^2 \tag{1.10}$$

This situation does not look favorable but it is possible that the increase of kinetic energy can be overcompensated due to the interaction of the magnetization with the molecular field as shown in the following. After the spin flip, the number of spin up and spin down electrons are given by:

$$n_{\uparrow} = \frac{1}{2}(n + g(E_{\mathrm{F}})\delta E) \tag{1.11}$$

$$n_{\downarrow} = \frac{1}{2}(n - g(E_{\mathrm{F}})\delta E) \tag{1.12}$$

where n is the number of electrons at the Fermi energy in the paramagnetic case. By assuming that each electron has a magnetic moment of $1\mu_B$ the magnetization can be written as: $M = \mu_B(n_\uparrow - n_\downarrow)$. The potential or molecular field energy amounts to:

$$\Delta E_{\text{P.E}} = -\frac{1}{2}\mu_0 M \cdot \lambda M = -\frac{1}{2}\mu_0\mu_B^2\lambda(n_\uparrow - n_\downarrow)^2 \qquad (1.13)$$

Introducing $U = \mu_0\mu_B^2\lambda$ which is a measure of the Coulomb energy, one gets:

$$\Delta E_{\text{P.E}} = -\frac{1}{2}U \cdot (g(E_F)\delta E)^2 \qquad (1.14)$$

The total change in energy amounts to

$$\Delta E = \Delta E_{\text{K.E}} + \Delta E_{\text{P.E}} = \frac{1}{2}g(E_F)(\delta E)^2(1 - Ug(E_F)) \qquad (1.15)$$

Therefore, a spontaneous ferromagnetism is possible if $\Delta E < 0$, i.e. $Ug(E_F) > 1$ which is known as *Stoner criterion* for ferromagnetism. Values of U, $g(E_F)$, and $U \cdot g(E_F)$ are shown in Fig. 1.3 for some of metals such as Fe, Co, Ni, and Pd.

From Fig. 1.3, only Fe, Co, and Ni exhibit a value of $U \cdot g(E_F) > 1$. This condition for the ferromagnetic instability requires that the Coulomb effects are strong and also that the density of states at the Fermi energy is large. If there is spontaneous ferromagnetism, the spin-up and spin-down bands will be split by an energy Δ, where Δ is the exchange splitting, in the absence of an applied magnetic field.

For $U \cdot g(E_F) < 1$ no spontaneous magnetization is present but nevertheless the magnetic susceptibility may be different from the paramagnetic value. In this case χ is larger than the expected χ^{Pauli} without the presence of Coulomb interactions by factor $(1 - Ug(E_F))^{-1}$ which is called *Stoner enhancement*. It is responsible for the enhanced Pauli susceptibility measured in the metals Pd and Pt which can both be thought of as systems on the verge of ferromagnetism; they have a large enough value of the parameter $Ug(E_F)$ to cause a significant enhancement of the magnetic susceptibility but not large enough (i.e. not sufficiently close to 1) to cause spontaneous ferromagnetism.
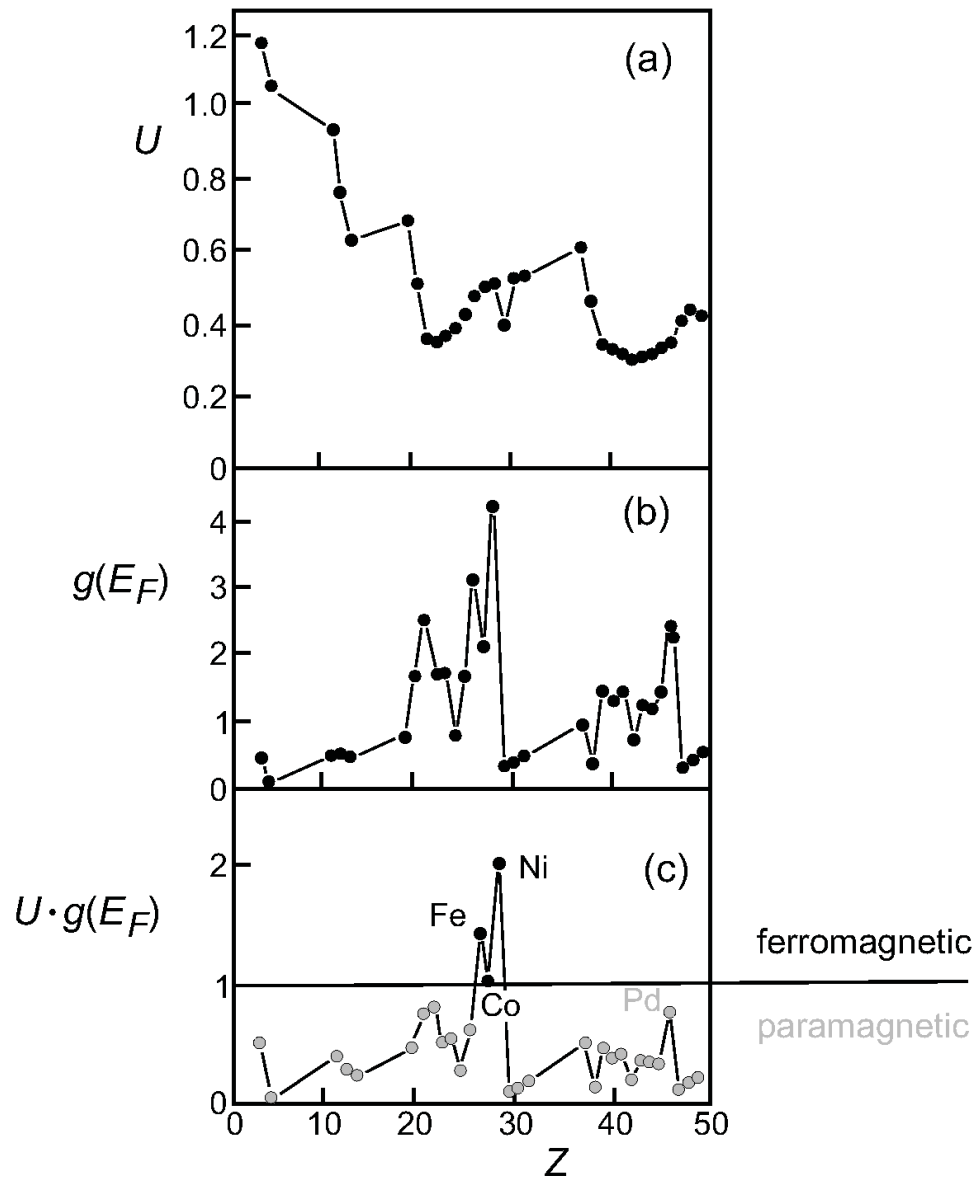
Figure 1.3: Values of the Stoner parameter U , density of states per atom $g(E_F)$ at the Fermi energy, and $U \cdot g(E_F)$ as a function of the atomic number Z. Only the elements Fe, Co, and Ni fulfill the Stoner criterion and are ferromagnetic [12].

1.5 Superparamagnetism

Superparamagnetism is a phenomenon in which magnetic materials may exhibit a behavior similar to paramagnetism at temperatures below the Curie or the Néel temperature but with a giant magnetic moment, as there is still a well-defined magnetic order. Magnetic properties of suparparamagnets are based on the single domain theory.

1.5.1 Single domain theory

In a ferromagnet, magnetic domains are ensembles of aligned individual magnetic moments of the atoms all pointing in the same direction and acting cooperatively. The magnetic domains are separated by domain walls, which have a characteristic width and energy associated with their formation and existence. Domain walls are interfaces between regions in which all spins point into the same direction while the magnetization direction changes from domain to domain. Within the wall, the magnetization must change direction from that in one domain to that in the other domain and the magnetization reversal occurs through the alinement of the magnetization vectors in a domain and the movement of the domain walls. The width of the Domain walls is determined principally by exchange and magnetocrystalline energy. The exchange energy tends to make the wall as wide as possible whereas the anisotropy tends to make the wall as thin as possible. As a result of this competition between exchange and anisotropy energies, the domain wall has a finite width (in the order of 100 nm) and surface energy. The interplay between long range and short range effects results in the domain states being grain-size dependent. As the grain size decreases, a critical size will be reached where the grain can no longer accommodate a wall. Below this critical size, the grain contains a single domain in which the magnetization reversal may occur by coherent rotation of spins, curling, or quantum tunneling of the magnetization vector. Therefore, the size reduction in magnetic ma-
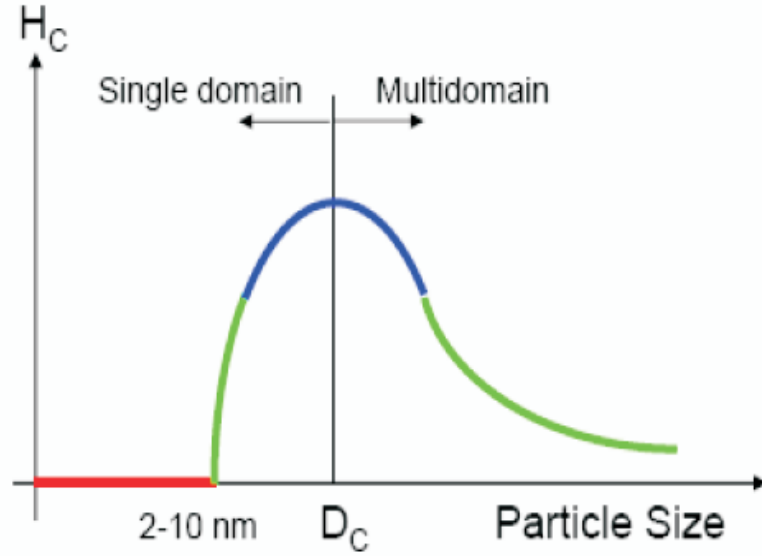
Figure 1.4: Schematic illustration of the dependence of coercivity on particle size, where D_{C} is the critical diameter which distinguishes between multi domain and single domain [10].

terials (multi-domain materials) results in the formation of single domain particles [13-15].

In addition, reducing the grain size in general is expected to create more pinning sites of the domain walls and to increase the coercivity H_{C} (the required energy to allow the walls to continue moving). This is true for larger grain sizes, but below a certain value, H_{C} decreases rapidly (Fig. 1.4). This threshold is the maximum size, D_{C}, for which coherent magnetization reversal of a single magnetic domain is feasible. As shown in Fig. 1.4, the maximum coercivity of a given material as a function of particle diameter actually falls in the single domain range. Therefore, the critical diameter for a magnetic particle to reach the single domain limit is equal to [15]

$$D_{\mathrm{C}} = \frac{18\sqrt{AK}}{\mu_0 M_s^2} \tag{1.16}$$

where A is the exchange constant, K is the effective anisotropy constant and M_{S} is the saturation magnetization. For most magnetic materials, this diameter is in the

range 10-100 nm, though for some high anisotropy materials the single domain limit can be several hundred nanometers [16].

From Fig. 1.4 one also can observe two important types of magnetic behavior in the single domain regime for magnetic nanoparticles, namely single domain ferromagnetic (FM) nanoparticles and superparamagnetic (SPM) nanoparticles. Like bulk ferromagnets, an array of single domain magnetic nanoparticles can exhibit hysteresis in the magnetization versus field dependence. However, in an array of single domain particles, the moment of each particle interacts with its neighbors and the field to align in the field direction [14, 17, 18].

1.5.2 Basics of superparamagnetism

For a single domain particle, the amount of energy required to reverse the magnetization over the energy barrier from one stable magnetic configuration to the other is proportional to $KV/k_\mathrm{B}T$ where V is the particle volume, k_B is Boltzmann's constant and T is the temperature [19]. If the thermal energy is large enough to overcome the anisotropy energy $(E = KV)$, the magnetization direction is no longer stable and the particle is said to be superparamagnetic (SPM). This means an array of nanoparticles each with its own moment can be easily saturated in the presence of a field, but the magnetization returns to zero upon removal of the field as a result of thermal fluctuations (i.e. both M_r and H_C are zero) [20]. The temperature at which the thermal energy can overcome the anisotropy energy of a nanoparticles is referred to as the blocking temperature, T_B [19]. For an ensamble of nanoparticles with a distribution in volume, T_B represents an average characteristic temperature and can be affected by inter-particle interactions as well as the time scale over which the measurement is performed due to the magnetic relaxation of the particles [21]. Fig. 1.5 shows a schematic illustrating the difference in the magnetization versus field behavior of an ensemble of single domain magnetic nanoparticles in the blocked state (Fig. 1.5(a)) and an array of SPM nanoparticles (Fig. 1.5(b)) [22].
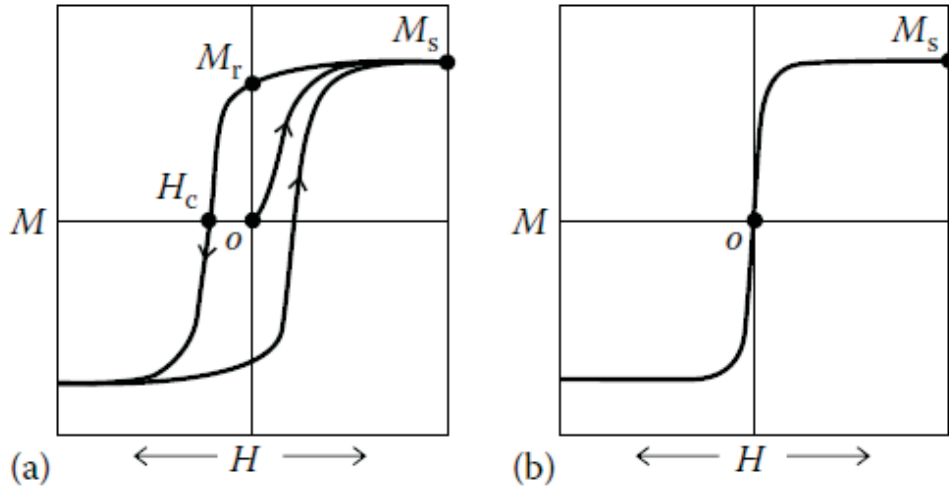
Figure 1.5: Schematic illustration of (a) a typical hysteresis loop of an array of single domain ferromagnetic nanoparticles and (b) a typical curve for a superparamagnetic material [22].

On the other hand in 1948, Stoner and Wohlfarth [23] described theoretically the case of the magnetization reversal through the coherent rotation of the magnetization vector for an assembly of single-domain particles. The Stoner-Wohlfarth model has described the magnetization curves of an aggregation of single-domain particles with uniaxial anisotropy either as a result of particle shape or from the magnetocrystalline anisotropy. The main assumptions of the model were: (i) coherent rotation of the magnetization vector from one magnetic easy axis to another via a magnetically hard direction and (ii) negligible interaction between the particles.

For more explanation let us consider an assembly of uniaxial, single-domain particles, each with an anisotropy energy $\Delta E = KV sin^2\theta$, where θ is the angle between the magnetization and the easy axis, K is the anisotropy constant and V is the volume of the particle. For a particle, the energy barrier ($\Delta E_{\rm B} = KV$ where $E_{\rm B}$ is the energy barrier needed for the rotation of the magnetization) separates two energy minima at $\theta = 0$ and $\theta = \pi$ corresponding to the magnetization parallel or antiparallel to the easy axis as shown in Fig. 1.6 [24]. However, if the single-domain particles become small enough, KV would become so small that thermal energy
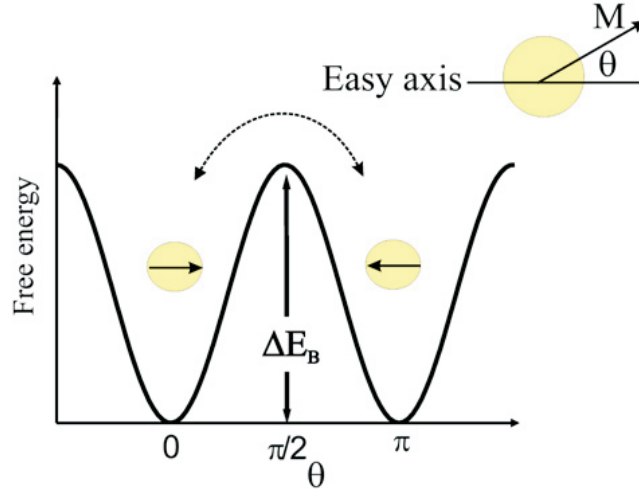
Figure 1.6: Schematic picture of the energy of a single-domain particle with uniaxial anisotropy as a function of magnetization direction. E_B is the energy barrier needed for the rotation of the magnetization and θ is the angle between the magnetization M and the easy axis [24].

fluctuations could overcome the anisotropy energy and spontaneously change the direction of magnetization of the entire crystallite. Hence, the magnetization will fluctuate between the two energy minima as shown in Fig. 1.6. The direction of the magnetization then fluctuates with a frequency f or a characteristic relaxation time, $\tau^{-1} = 2\pi f$. It is given by the Néel-Brown expression,

$$\tau = \tau_0 \exp\left[\frac{KV}{k_{\mathrm{B}}T}\right] \tag{1.17}$$

where $\tau_0 \sim 10^{-10}$ sec is the inverse attempt frequency [25, 26]. The fluctuations thus slow down (τ increases) as the sample is cooled to lower temperatures (Fig. 1.7) and the system appears static when τ becomes much longer than the experimental measuring time τ_{m}, then the particle is said to be blocked (frozen) as shown in Fig. 1.7(a). In contrast, at temperature above T_{B}, the particle moments appear free (Fig. 1.7(b)). Using Eq. 1.17 one obtains

$$T_{\mathrm{B}} \approx \frac{KV}{k_B \ln(\frac{\tau_{\mathrm{m}}}{\tau_0})}. \tag{1.18}$$

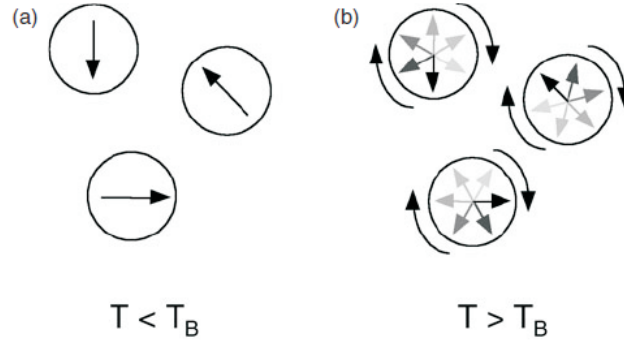Figure 1.7: Illustration of the concept of superparamagnetism, where the circles depict three magnetic nanoparticles, and the arrows represent the net magnetization direction in those particles. In case (a), at temperatures well below the blocking temperature T_B of the particles, the net moments are quasi-static. In case (b), at a temperature well above T_B, the moment reversals are so rapid that in zero external field the time-averaged net moment on the particles is zero [26].

The above equation is valid for individual particles or a system of non-interacting particles with the same size and anisotropy.

1.5.3   Non-monodisperse particles

If the particles are not monodisperse, the distribution of particle sizes results in a blocking temperature distribution. In practice, the relaxation of blocked magnetic nanoparticle ensembles is often studied within fundamental protocols by measuring the so-called zero field cooled (ZFC) magnetization and the field-cooled (FC) magnetization. In the ZFC process the system is cooled to a low temperature in zero magnetic field from a temperature, where the entire system shows superparamagnetic response. Then a small probing field is applied, and the induced magnetization is measured versus temperature during heating. In the FC process, which usually follows the ZFC one, the magnetization is measured as a function of temperature upon heating after cooling the sample in a field again from a sufficiently high temperature.

The data of the ZFC-FC magnetization [27, 28] and in particular its difference can provide information about the average blocking temperature, from which e.g. the mean particle diameter can be extracted by assuming the particles to have nearly spherical shape with a known anisotropy constant.

1.5.4 Magnetic anisotropy

The magnetic anisotropy describes the dependence of the internal energy on the direction of the spontaneous magnetization, creating easy and hard directions of magnetization. The total magnetization of a system will prefer to lie along the easy axis. The energetic difference between the easy and hard axis results from two microscopic interactions: the spin-orbit interaction and the long-range dipolar coupling of magnetic moments. The anisotropy energy arises from the spin-orbit interaction and the possibly partial quenching of the angular momentum. The spin-orbit coupling is responsible for the intrinsic (magnetocystalline) anisotropy, the surface anisotropy, and the magnetostriction, while the shape anisotropy is a dipolar contribution. Anisotropy energies are usually in the range $10^2 - 10^7$ Jm^{-3} [29]. This corresponds to an energy per atom in the range $10^{-8}-10^{-3}$ eV. The anisotropy energy is larger in lattices of low symmetry which contain magnetic ions of and smaller in lattices of high symmetry. In bulk materials, magnetocrystalline and magnetostatic energies are often the main source of anisotropy whereas in fine particles, thin films and nanostructures, other kinds of anisotropies such as shape and surface anisotropy are relevant in addition [29]. In the following we will discuss the magnetocrystalline anisotropy which is relevant for the materials studied in the work at hand.

1.5.4.1 Magnetocrystalline anisotropy

Generally the magnetic anisotropy energy term includes the crystal symmetry of the material, and is known as crystal magnetic anisotropy or magnetocrystalline anisotropy [30]. The simplest form of crystal anisotropies are the uniaxial ones. For

uniaxial symmetry the energy is given by

$$E_a^{\text{uni}} = K_1 V \sin^2_\Theta + K_2 V \sin^4_\Theta + ...$$ (1.19)

where K_1 and K_2 are anisotropy constants, V is the particle volume and θ is the angle between the magnetization and the symmetry axis. The anisotropy constants depend on temperature [31], but at temperatures much lower than the Curie temperature of the material they can be considered as constants. Usually in case of ferromagnetic materials, K_2 and other higher order coefficients are negligible in comparison with K_1 and many experiments may be analyzed by using the first term only. In the convention of Eq. 1.19, $K_1 > 0$ implies an easy axis. For single-domain particles with uniaxial anisotropy most of the calculations are performed also by neglecting K_2 and the magnetocrystalline anisotropy energy is written as

$$E_a^{\text{uni}} = KV \sin^2_\Theta$$ (1.20)

where K is usually considered as the uniaxial anisotropy constant. This expression describes two local energy minima at each pole ($\theta = 0$ and π) separated by an equatorial ($\theta = 90$) energy barrier KV as shown in Fig. 1.6. For crystals with cubic symmetry, the anisotropy energy can be expressed in terms of the direction cosines ($\alpha_1, \alpha_2, \alpha_3$) of the internal magnetization with respect to the three cube edges [32]

$$E_a^{\text{cubic}} = K_1 V (\alpha_1^2 \alpha_2^2 + \alpha_2^2 \alpha_3^2 + \alpha_3^2 \alpha_1^2) + K_2 V \alpha_1^2 \alpha_2^2 \alpha_3^2$$ (1.21)

where the α_i are defined through $\alpha_1 = \sin\theta\cos\phi$, $\alpha_2 = \sin\theta\sin\phi$ and $\alpha_3 = \cos\theta$ with θ the angle between the magnetization and the Z-axis and ϕ is the azimuthal angle.

1.5.5 Effects of inter-particle interactions

In all fine-particle systems, different kinds of magnetic inter-particle interactions exist and the interaction strength varies with the volume concentration. Inter-particle

interactions may arise from dipole-dipole interactions or exchange interactions between surface ions of neighboring particles. When a capping surfactant such as oleic acid, carbon, or silica etc., is used, the exchange interactions become negligible and the primary interaction is due to dipole-dipole coupling which is explained as following:

dipole-dipole interaction: Two magnetic dipoles μ_1 and μ_2 separated by a distance r will have potential energy [11, 33, 34]

$$E \; = \; \frac{\mu_0}{4\pi r^3}\left[\mu_1 \cdot \mu_2 - \frac{3}{2}(\mu_1 \cdot r)(\mu_2 \cdot r)\right]. \tag{1.22}$$

From Eq. 1.22, it is seen that the strength of this interaction depends on their distance and their degree of mutual alignment. One can easily estimate the order of magnitude of dipolar effects for two moments each of $\mu_1 \approx \mu_2 \approx 1\ \mu_B$ separated by r ≈ 0.1 nm to be $\mu^2/4\pi r^3 \sim 10^{-23}$ J, which is equivalent to about 1 K in temperature. Therefore the dipolar interaction is much too weak to account for the ordering of most magnetic materials, since most of the magnetic materials order at much higher temperature. Here note that in nanoparticle system μ can be large and dipole-dipole interaction would be relevant.

Note that also in the fine particles system, when the particles are separated far enough from each other, then inter-particle interactions can be neglected [11, 35, 36].

1.5.6 Superparamagnetism limitations for applications

The magnetic instability of small superparamagnetic nanoparticles has proven to be a challenge in the current design of magnetic data storage [37]. It has also been found that the ability to synthesize small nanoparticles with high coercivity and anisotropy could lead to significant improvements for the next generation of permanent magnets [38, 39]. On the other hand, the properties that characterize superparamagnetic nanoparticles namely high saturation magnetization accompanied by a low saturation field and no remnant magnetization have proven to be ideal for biomedical ap-

plications. The lack of prominent inter-particle interactions, which normally lead to aggregation of particles, enable the synthesis of nanoparticle dispersions (ferrofluids) which can be injected into biological systems and manipulated by external field gradients. Such dispersions are currently finding applications in site specific treatments such as targeted drug delivery, localized heating of cancerous cells (hyperthermia), and magnetic resonance imaging (MRI) contrast enhancement [40]. All these important applications of magnetic nanoparticles will be highlighted in chapter 3. But before introducing these applications, the synthesis and the growth mechanisms of the magnetic nanoparticles will be explained as presented in the following chapter.

Chapter 2

Synthesis of magnetic nanoparticles

During the last decades, great efforts have been done on the synthesis of magnetic nanoparticles due to their potential applications in many diverse fields. Before introducing applications for these particles , several successful approaches for the synthesis of magnetic nanoparticles were investigated, providing particles of controllable shapes and narrow size distributions [41-44]. Magnetic nanoparticles display a treasure of size dependent structural, magnetic, electronic, and catalytic properties [45-49]. Magnetic nanoparticles have been synthesized with a number of different compositions and phases, including the pure metals Fe, Co and Ni [26, 50, 51]; metal oxides, such as Fe_3O_4 and γ-Fe_2O_3 [52-54]; ferrites, such as MFe_2O_4 (M = Cu, Ni, Mn, Mg, etc.) [55, 56]; and metal alloys, such as FePt, CoPt [38, 46]. Usually, the synthesized magnetic nanoparticles have to be capped with a shell which prevents their agglomeration and oxidation in a colloidal solution. The shell composition also allows to tailor the chemical properties such as solubility, chemical reactivity, surface chemistry, and binding affinity. The shells could be formed by covalent attachment of small-molecule ligands, by adsorption of polymers [57, 58] or by encapsulation in block copolymer micelles [59, 60]. In addition to their effects on the surface chemistry, the shells increase the inter-particle spacing in nanoparticles in order to decrease the inter particle interaction. Here this chapter focuses on the synthesis of magnetic

nanoparticles using different methods.

2.1   Synthesis methods

Magnetic nano-structured materials include alloys, compounds and composites, that have or their components have nanometer sized structures in one or more dimensions [61]. According to the dimensions concept, magnetic nano-structured materials can be classified into three types:

1. Zero dimensional nano-structured magnetic materials, which have a nanometer sized structure in three dimensions, such as magnetic nanoparticles.

2. One dimensional nano-structured magnetic materials, which have nanometer sized structure in two dimensions, such as magnetic nanowires.

3. Two dimensional nano-structured magnetic materials, which have nanometer sized structure in one dimension, such as magnetic thin films or super lattices.

Recently a large portion of the published articles about magnetic nanoparticles have described efficient routes to attain shape-controlled, highly stable, and narrow size distributed magnetic nanoparticles. Up to date, several popular methods including co-precipitation, microemulsion, thermal decomposition, solvothermal, sonochemical, microwaveassisted, chemical vapour deposition, combustion synthesis, carbon arc, and laser pyrolysis synthesis have been reported for the synthesis of magnetic nanoparticles. Basically, most of the synthesis methods can be classified into two categories: either physical or chemical processes as shown in Fig. 2.1. The physical process, which is called physical vapor deposition process (PVD) [62], consists of two categories, one is the thermal evaporation process and the other is the sputtering process. The thermal process includes vacuum evaporation, laser evaporation, molecular beam epitaxy (MBE), ion plating, activated reactive evaporation (ARE), and ionized cluster beam deposition (ICBD). The chemical process also consists of
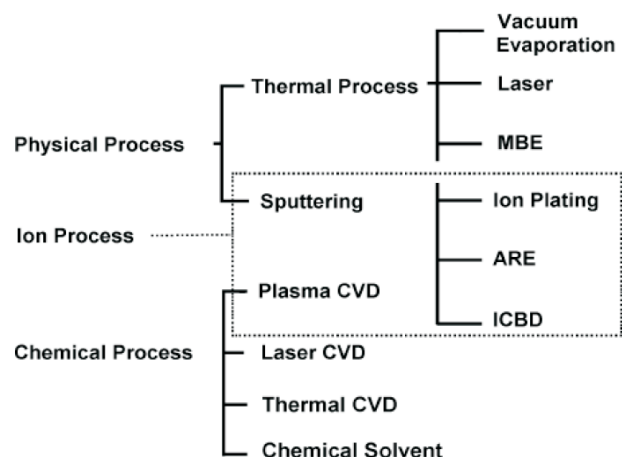
Figure 2.1: Synthesis methods of magnetic nano-structured materials [62].

two categories, one is the chemical vapor deposition (CVD) process and the other is the chemical solvent process. The CVD processes include plasma CVD, laser CVD and thermal CVD processes. Generally, all these methods are based on liquid, solid, gas phase synthesis processes as will be discussed in the following subsections:

2.1.1 Liquid phase synthesis

The effectiveness of liquid-phase synthesis routes for nanoparticles strongly depends on the resulting width of the particle size distribution. Agglomeration and non-uniformity in particle size and shape are typical problems, especially for nanoparticles on the smaller end of the nanometer range (1-10 nm). These problems can potentially be avoided by appropriately modifying the liquid-phase synthesis route, since various methods of this type yield unagglomerated and relatively monodisperse (with a relative standard deviation of $\sim 5\%$) nanoparticles [63]. The classic studies of LaMer and Dinegar [64] have shown that the production of monodisperse colloids requires temporal separation between nucleation and nanoparticle growth. Thus, in current preparation methods, the molecular precursors are rapidly added at high temperature into small batch reactors. The increase of the precursor concentration

above the nucleation threshold causes a short nucleation burst leading to the production of a large number of very small nanoparticles. There are many methods based on liquid phase synthesis which will be discussed in the following examples:

2.1.1.1 CO-Precipitation

CO-Precipitation method is the easy and convenient way to synthesize magnetic nanoparticles (metal oxides and ferrites) from aqueous salt solutions. The method usually applies the addition of a base under inert atmosphere at room temperatures or at elevated temperature and complete precipitation should be expected at a pH level to this solution between 8 and 14 [65]. In this method, the reaction temperature and time are lower than in other methods such as thermal decomposition and hydrothermal ones resulting in inhomogenious particle sizes and shapes. Hence, the size distribution in this method is relatively wide and the shape control is not good [66].

2.1.1.2 Microemulsion

The microemulsion method is commonly known as the water-in-oil (W/O) microemulsion method, which has been widely used to synthesize uniform sized magnetic nanoparticles [67-70]. The microemulsion is an isotropic and thermodynamically stable single-phase system that consists of three components: water, oil and an amphiphilic molecule, i.e. the surfactant. The surfactant molecule reduces the interfacial tension between water and oil resulting in the formation of a transparent solution. The water nanodroplets containing reagents, as a nanoreactor, undergo rapid coalescence allowing for a mixing, precipitation reaction and an aggregation processes for the synthesis of magnetic nanoparticles. The shape of the water pool is spherical and the surfactant molecules surround the nanodroplet wall. These walls act as cages for the growing particles and thereby reduce the average size of the particles during the collision and aggregation process. Thus, the size of the spherical

nanoparticles can be controlled and tuned by changing the size of the water pool. Microemulsion can be used to synthesize monodispersed nanoparticles with various morphologies. However, this method requires a large amount of solvent and also the yield of production of this method is low [71].

2.1.1.3   Thermal decomposition

The high-temperature decomposition of organometallic precursors can produce magnetic nanoparticles with a high level of monodispersity and size control. These precursors are, e.g., $[M^{n+}(acac)_n]$, (M = Fe, Mn, Co, Ni, Cr; n = 2 or 3, acac = acetylacetonate), $M_x(cup)_x$ (cup = N-nitrosophenylhydroxylamine) or carbonyl such as $Fe(CO)_5$) using organic solvents and surfactants such as fatty acids, oleic acid and hexadecylamine [72]. Thermal decomposition of organometallic precursors such as $Fe(CO)_5$ initially leads to a formation of metal nanoparticles but if followed by oxidation can lead to a high in quality monodispersed metal oxide [73, 74]. On the other hand, decomposition of precursors with cationic metal centers such as $Fe(acac)_3$ leads directly to metal oxide nanoparticles. The reaction temperature and time, as well as the aging period may also be crucial for the precise control of size and morphology [75]. Thermal decomposition seems the best method developed to date for size and morphology control of nanoparticles. Also, the yield of production is high and scalable. However, one of the major disadvantages of this method is the production of organic soluble nanoparticles only which limits the applicability in biological fields in addition to the needed surface treatment after synthesis. Also, thermal decomposition methods usually lead to complicated processes or require relatively high temperatures.

2.1.2   Solid phase synthesis

Solid phase approaches have been used for synthesis of carbon encapsulated magnetic nanoparticles (CEMNPs). For example, nanoparticles can be made by means of high

temperature annealing of materials such as Fe_2O_3 plus C powders [76], elementary Fe plus C powders [77], and Co nanoparticles plus copolymers [78]. However, for example in Ref. [78], the size and the magnetic properties of the final particles can hardly be controlled, and superparamagnetic particles were not be obtained as the initial formed particle size was usually much larger than 10 nm.

2.1.2.1 **Combustion Synthesis**

Combustion methods based on solid phase synthesis have been applied for the preparation of CEMNPs [79, 80]. Martirosyan et al. [81] produced crystalline cobalt ferrite, $CoFe_2O_4$ nanoparticles (50-100 nm) by using the carbon combustion synthesis of oxides (CCSO). In their combustion synthesis process, the exothermic oxidation of carbons generate a thermal reaction wave that propagates through the solid reactants mixture of CoO and Fe_2O_3 converting it to cobalt ferrite. They found that the extensive emission of CO_2 increased the porosity and friability of the product. Also, a complete conversion to ferrite $CoFe_2O_4$ structure was obtained only for carbon concentrations exceeding 12 %wt. Solid state interactions between CoO and FeO with the growth of the crystalline cobalt ferrite particles started in the early period of the combustion. As expected, the average particle size increased with increasing combustion temperatures. The advantage of this method that it is suitable for large-scale production.

2.1.3 **Gas phase synthesis**

Among all the synthesis methods of nano-structured materials, the gas phase synthesis process is one of the most important methods for both large scale production and fundamental research [82]. This results from the fact that the gas phase synthesis process not only is able to produce large quantities of nanoparticles but also provides a high level of control on particle properties, such as size, shape, phase etc. For a detailed overview, Ref. [83] shows that the gas phase methods depend on thermal

decomposition, reduction, hydrolysis, oxidation, or other reactions to cause precipitation of solid products from the gas phase. In the work at hand the used gas phase method depends on the thermal decomposition of the sublimated materials in the vapor phase. There are many processes based on gas phase synthesis which will be discussed in the following examples:

2.1.3.1 Chemical vapour deposition

In the chemical vapor deposition (CVD) process, the source materials are first vaporized and decomposed into atoms or molecules, then react with other vapors, gases or liquids, and finally yield the reaction product on the substrate [54]. Based on the use of different methods of enhancing the chemical reaction, the CVD process can be classified into plasma assisted CVD, laser assisted CVD, and thermally assisted CVD. Introducing plasma, laser or thermal effects into the CVD process helps to break the chemical bonds and to activate the chemical reaction. In the CVD process, a carrier gas stream with precursors is delivered continuously by a gas delivery system to a reaction chamber maintained under a slight vacuum at high temperature (≥ 900 °C) [84]. The CVD reactions take place in the heated reaction chamber and the products combine to form clusters of nanoparticles. Growth and agglomeration of the particles are reduced via the rapid expansion of the two-phase gas stream at the outlet of the reaction chamber. The subsequent heat treatment of the synthesized nanopowders in the various high-purity gas streams allows compositional and structural modifications, including particle purification and crystallization, as well as transformation into a desirable size, composition, and morphology [83, 84]. The CVD process has been employed to deposit iron oxide by the reaction of a halide, such as iron trichloride, with water at 800-1000 °C [85]. The success of this method depends on the low concentrations of the precursor in the carrier gas, as well as the rapid expansion and then quenching of the nucleated clusters or nanoparticles as they exit from the reactor [83, 84]. Recently, catalytically assisted chemical vapour

deposition (CCVD) has become increasingly important because of its potential for scalable production [86]. However, this potential could not be practically realized until some problems have been solved [87, 88], such as the relatively low productivity, the existence of complex phases, and the difficulty in separating carbon-encapsulated superparamagnetic nanoparticles (CESNs) from the impurities.

2.1.3.2 Arc discharge

Usually arc discharge methods are used for the synthesis of most carbon encapsulated magnetic nanoparticles (CEMNPs). The metal precursors are packed inside a cave drilled into a graphite electrode and then subjected to arc vaporization [56, 89, 90]. Magnetic metal carbides can be encapsulated into carbon using this method. The arc discharge method has also been proposed to coat metal nanoparticles with boron nitride (BN) [90]. Dravid and co-workers [89] modified the arc discharge method and successfully produced nanophase Ni encapsulated in graphitic shells. In this case, the product usually consisted of mixtures of different forms of Ni and carbon encapsulates including carbon nanotubes, carbon encapsulated metal particles and graphitic flakes. In addition, the metal particles had a wide size distribution. Sun et al. [56] also developed a modified arc discharge (carbon arc) method for synthesizing of carbon encapsulated Fe, Ni and Co nanoparticles with average sizes lower than 15 nm. The disadvantage of this method that it is not suitable for the coating of large quantities of nanoparticles which are needed for the industrial production due to its low production yields. In addition, it is difficult to control the particle sizes as well as the carbon coating thickness.

2.1.3.3 Laser Pyrolysis

Laser pyrolysis is a technique for the preparation of iron oxides nanostructures. It is used when ironpentacarbonyl-based mixtures and ethylene, as an energy transfer agent are employed using air, as an oxidant [91]. Laser light heats a gaseous mixture

of iron precursor and a flowing mixture of gases produces small, narrow sized, non aggregated nanoparticles. Usually this method is used for magnetite synthesis. In addition, this method has been used for the synthesis of magnetic nanoparticles in the liquid phase, too [92, 93].

2.2 Formation of nanoparticles in the gas phase

In this section, the thermodynamics of the formation of nanoparticles in the gas phase, including the nucleation and growth process will be described in detail.

2.2.1 Nucleation mechanism of nanoparticles in the gas phase

For understanding the basics of nanoparticle nucleation growth in the gas phase, the classical thermodynamics can be used [94, 95]. In fact the gas phase condensation process is a commonly seen phenomenon in nature, such as the formation of rain or snow. The basic process is: First a vapor of source materials is generated through an appropriate evaporation process. When the vapor pressure exceeds the supersaturation limit, small nuclei begin to form in the vapor gas. This nuclei formation process can be either heterogeneous if there are already some nucleation seeds existing in the vapor or homogeneous if no nucleation seeds are present in the vapor. After the formation, nuclei will grow into bigger particles through either surface growth or agglomeration, which depends on the vapor conditions and nuclei density. For the gas phase synthesis of nano-structued materials, the whole process happens in a high vacuum chamber, therefore the homogeneous process is preferred. For discussing a thermodynamic process, the changes of Gibbs free energy should be considered as [94, 95],

$$dG = vdP - sdT \tag{2.1}$$

Here G is the Gibbs free energy, v is the specific volume, P is the pressure, s is the specific entropy, and T is the temperature. In a vapor, by integrating dG along the

excess of specific Gibbs free energy:

$$\Delta G \;=\; RTln(P/\acute{P}) \tag{2.2}$$

where R is the ideal gas constant. For a nucleus, the Gibbs free energy will be:

$$\Delta G \;=\; -\frac{4}{3}\pi r^3 \rho RT \ln S + 4\pi r^2 \sigma \tag{2.3}$$

where r, ρ and σ are nucleus radius, density and surface free energy, respectively. $S = P/\acute{P}$ is defined as the supersaturation ratio. The first term in Eq. 2.3 is the bulk Gibbs free energy derived from Eq. 2.2. The second term is surface Gibbs free energy. As shown in Eq. 2.3, the supersaturation ratio S must be larger than 1 in order to allow the formation of nuclei. If $S < 1$, then $\Delta G > 0$, which means the formation of nuclei is not favored. Therefore $S > 1$ is a pre-required condition for the nucleus to form in a vapor.

Since the Gibbs free energy is a function of the nucleus radius r, we can use Eq. 2.3 to derive a critical value r_{C}, where the growth behavior changes:

$$r_{\mathrm{C}} \;=\; \frac{3\sigma}{\rho RT \ln S} \tag{2.4}$$

Therefore the critical value for the excess Gibbs free energy is:

$$\Delta G_{\mathrm{C}} \;=\; \frac{16\pi\sigma^3}{3(\rho RT \ln S)^2} \tag{2.5}$$

For $r = r_{\mathrm{C}}$, ΔG_{C} reaches its maximum value. When $r < r_{\mathrm{C}}$, $d\Delta G_{\mathrm{C}}/dr > 0$, which means ΔG_{C} increases with r_{C}. In contrast, in the case $r > r_{\mathrm{C}}$, $d\Delta G_{\mathrm{C}}/dr < 0$, which means that ΔG_{C} decreases up on increasing r_{C}. Therefore, if the formed nucleus radius is smaller than its critical value r_{C}, the nucleus will decrease its size to minimize the excess Gibbs free energy ΔG. Eventually the nucleus will vanish. If the formed nucleus radius is larger than the critical value r_{C}, the nucleus will increase its size to minimize ΔG. Hence, only nucleus with radius larger than the critical value will keep growing.

2.2.2   Growth mechanism of nanoparticles in the gas phase

In the previous section, the gas phase nanoparticle nucleation mechanism has been discussed. In this section, two basic particle growth mechanisms, surface growth and agglomeration, will be addressed. If the surface growth mechanism applies, particles keep growing through absorbing atoms from the atom vapor and adding atoms to the particle surface. Therefore surface growth is a homogenous process. The growth rate is expressed as [96]:

$$N \; = \; [n_{\mathrm{S}} \exp(\frac{-\Delta G_{\mathrm{C}}}{k_{\mathrm{B}}T})]4\pi r_{\mathrm{C}}^2 [\frac{\alpha(P_{\mathrm{v}} - P_{\mathrm{s}})N_{\mathrm{A}}}{\sqrt{2\pi M_{\mathrm{A}}RT}}] \tag{2.6}$$

where n_{S} is the number of available nucleation sites (number of atoms in the gas phase), ΔG_{C} is the change of Gibbs free energy for a nucleus with the critical size, $4\pi r_{\mathrm{C}}^2$ is the surface area of a nucleus with a critical radius r_{C}, α is the sticking coefficient (number of sticking atoms/number of impinging atoms), P_{v} is the vapor pressure of the supersaturated vapor, P_{s} is the vapor pressure on the nucleus surface, N_{A} is Avogadro's number and M_{A} is the atomic weight. According to Eq. 2.5 and 2.6, the main factors that influence the particle surface growth rate are:

1. n_{s}, the number of available nucleation sites. The growth rate is proportional to the number of available atoms in the vapor.

2. Supersaturation ratio S. The growth rate is higher for higher supersaturation ratios.

3. T, the temperature. The surface growth rate decreases upon increasing the temperature. At higher temperature, atoms in the vapor possess higher energy and it is less probable for them to be absorbed by the nucleii. The vapor also has higher supersaturation pressure at higher temperature which leads to a smaller supersaturation ratio S.

For the particle agglomeration or particle coalescence mechanism, the particles grow through the merging of several nuclei. In the gas phase, all nuclei are not stationary but, rather moving in a random manner (Brownian motion). Therefore in a vapor with a high concentration of nuclei, the probability of a collision of nuclei is very high. By means of this mechanism, nuclei can quickly increase their size by merging to other nuclei.

The growth mechanism has great influence on the properties of the particles formed. Particles grown by the surface growth mechanism usually have a smaller size, narrower size distribution, and better crystallinity. In contrast, those grown by the agglomeration or coalescence mechanism usually have relatively larger size and wider size distribution. The particles formed usually have poly-crystalline structure and the crystallinity is lower. The reason is that upon surface growth the particle size growth rate is lower. Hence, atoms have enough energy and time to self-organize on the particle surface to seek a low energy state, which will lead to a good crystalline structure. Which mechanism dominates in the particle growth process is determined by the vapor supersaturation ratio. High vapor supersaturation ratio causes both high nucleation rate and high nuclei concentration in the vapor [97]. In this case the agglomeration or coalescence mechanism will dominate the particle growth process. Contradictorily, at low vapor supersaturation ratio the surface growth mechanism dominates. In addition, the vapor supersaturation ratio is directly related to the vapor temperature. The vapor saturation pressure is proportional to the temperature for most materials. With the same vapor pressure, the vapor supersaturation ratio is higher at low temperature and lower at high temperature. Therefore for the vapor of a certain material with a certain pressure, the agglomeration or coalescence mechanism is dominating at low temperature while surface growth mechanism is favored at sufficiently high temperature.

2.2.3   Cooling processes for generating supersaturated vapor

As mentioned above, the vapor saturation pressure inversely depends on the temperature. Therefore a vapor cooling process will effectively generate supersaturated vapor [97]. Basically there are two ways of cooling the vapors:

1. The first one is inputting inert gas to cool the vaporized atoms through collisions in which energy is transferred from energized vapor atoms to low energy inert gas atoms.

2. The second method is to suddenly expand the vapor volume to cool down the vaporized atoms which is also called supersonic jet expansion.

The sudden volume expansion in the second method introduces a very fast particle nucleation and growth process, which is favorable for achieving a large quantity of the fabricated nanoparticles. However, the second method has a poor control of the particle nucleation and growth process compared to the first one as mentioned before.

2.3   Protection methods (core/shell structure)

Actually, magnetic nanoparticles are very sensitive to oxidation and agglomeration due their large specific surface area and are also high in its chemical reactivities. Under ambient conditions, rapid oxidation of the nanoparticles' surfaces occurs, leading to the creation of thin oxide layers that can dramatically change the particle properties. Natural agglomeration of nanoparticles into larger clusters is another problem that hinders the processing of such materials. In order to preserve their specific magnetic properties and to protect nanoparticles from both oxidation and agglomeration, the application of encapsulation procedures has been proposed. Encapsulation of nanoparticles has been successfully employed by using carbon, silica, precious

metals, metal oxides, organic polymers and surfactants as will be exemplified in the proceeding paragraphs.

2.3.1   Surfactants

When employing surfactants as covering shells, a dense coverage by the organic surfactant is crucial for preventing the particles from being oxidized by air. Sun and Murray [98] have demonstrated the synthesis of Co nanoparticles in the presence of an organic surfactant such as oleic acid, lauric acid, trioctylphosphonic acid and pyridine. They found that oleic acid is an excellent capping agent that can bind strongly to the surface of metals with native oxides through the carboxyl group. This approach has been used for the synthesis of colloidal nanoparticles for a large number of metals [98].

2.3.2   Polymers

Although the development of other types of shells, polymers coating shells are receiving more and more attention. Polymers can increase repulsive forces more than surfactants. In addition, a polymer coating on the surface and their dispersions offer a high potential of several applications such as increasing capacity for information storage or magnetic memory polymer stents as medical implants for biomedical applications [99]. It is known from the literature that both natural and synthetic polymers have been used for coating of magnetic nanoparticles. The most common natural polymers are dextran, chitosan, starch, gum arabic, and gelatine. The mostly used synthetic polymers are polyethylene glycol (PEG), polyvinyl alcohol (PVA), poly lactide acid (PLA), alginate, polyacrylic acid (PAA) and polymethylmethacrylate (PMMA). However, a thin polymer coating is not very suitable to protect extremely reactive magnetic nanoparticles. Metallic magnetic nanoparticles, which are stabilized by single or double layers of surfactants or polymers are not air stable, making

them easily leached by an acidic solution [100], resulting in the loss changes of their magnetic properties. Another disadvantage of polymer-coated magnetic nanoparticles is the relatively low intrinsic stability of their coating at higher temperatures, a problem which is even more enhanced by the possible catalytic action of the metallic cores. Therefore, the development of other methods for protecting magnetic nanoparticles is needed.

2.3.3   Metal oxides

One of the straightforward methods for protecting magnetic particles is to induce a controlled oxidation of a pure metal core. Bönnemann et al. [101] developed a mild oxidation method, using synthetic air to smoothly oxidize the outer surface of the synthesized cobalt nanoparticles to form a stable CoO which can protect the cobalt nanoparticles from further oxidation. When iron nanoparticles are exposed to aqueous solutions, immediately a shell which consists of mostly iron oxides and hydroxides will form on the outer surface of the iron core which can stabilize the iron nanoparticles against further oxidation. Another way for protection of magnetic nanoparticles can be via metal oxides coating. Some examples of this approach are the usage of metal oxides such as titanium oxide [102], zirconium oxide [103] and aluminum oxide [104] which have been reported as coatings for magnetic iron oxide nanoparticles.

2.3.4   Precious metals

Gold is a widely used coating material due to its specific surface derivative properties for subsequent treatment with chemicals or biomedical agents. For example, it is well established that Au nanoparticles surfaces can be functionalized with thiolated organic molecules for further applications [105, 106]. The most common techniques for deposition of precious metals on magnetic nanoparticles are reactions in microemul-

sion [107] and redox transmetalation [108]. Sun et al [109] showed that gold coating of iron nanoparticles preserves the magnetic properties of the iron core while enhancing its stability. Thus, the combination of magnetism, selectivity, trial fictionalizations and stability displayed in gold-coated iron oxide particles is promising in applications such as magnetic separation, controlled release, and targeted drug delivery.

2.3.5   Silica

Magnetic microspheres consisting of a magnetic core and a silica shell have attracted particular attention [110] due to their unique magnetic responsivity, low cytotoxicity, easy chemically modifiable surfaces and the easy control of interparticle interactions through the variation of the shell's thickness. However, the disadvantage regarding the synthesis of silica-coated magnetic nanoparticles is the difficulty or even impossibility to achieve a fully dense and nonporous silica coating. These problems render it difficult to maintain a high stability of these nanoparticles under hard conditions.

2.3.6   Carbon

In the last few years carbon encapsulated magnetic nanoparticles (CEMNPs) have received considerable attention because of their potential as small magnetic clusters for high density magnetic data storage, in ferrofluid applications, magnetic resonance imaging and implants for hyperthermia therapy of cancer treatment [111]. Carbon is one of the best solutions for encapsulation of metal nanoparticles because carbon is chemically and thermally stable, cheap, light and biocompatible. In addition, the carbon shell can be thinned/removed by hydrogen or oxygen gas if desired. Because of these advantages of carbon, various methods for preparing the carbon capsulated nanoparticles have been developed, such as arc discharge techniques, chemical vapor depositions, combustion, pulsed laser decomposition and pyrolysis of metal complexes. Park et al. [93] have synthesized CEMNPs using a solution contain-

ing various metalocenes dissolved in xylene is irradiated with a nanosecond pulsed ultraviolet laser at room temperature and atmospheric pressure. They tested the chemical stability of CEMNPs by sonicating in a 10 M HCl solution using an ultrasonic cleaner. After ultrasonication, only CEMNPs with complete carbon shell were observed while none of the remaining nanoparticles had imperfect carbon shells, e.g., there were no amorphous carbon coated Fe-C nanoparticles. In addition, CEMNPs with graphitic layers were still found in the HRTEM images. Park et.al [93] concluded that graphitic coatings have better chemical stability in acids at least as compared to amorphous coating. Generally, low graphitization of the carbon shell is observed at low laser energy conditions, which is considered to be due to the relatively low solution temperature. Thus, in recent years Fe, Ni and Co have received more attention in CEMNPs synthesis due to their ferromagnetic properties and their unique catalyzing ability in the transformation of amorphous carbon into graphitic carbon at sufficiently high temperatures [112].

In chapters 5, 6 and 7, it will be shown how these magnetic nanoparticles are synthesized by means of high pressure chemical vapor deposition technique and their properties will be described.

Chapter 3

Applications of magnetic nanoparticles

3.1 Industrial applications

As discussed in the previous chapters, magnetic nanoparticles have attracted great interest for many vital applications. These potential applications include development of high density magnetic data storage devices, xerography, electronics (recording media), catalysis, magnetic inks (for jet printing), magnetic refrigeration etc, [111, 113-115]. The most famous used magnetic nanoparticles are magnetite and hematite which have been used as catalysts for a number of industrially important reactions, including the synthesis of NH_3, the high temperature water gas shift reaction, and the desulfurization of natural gas. Other reactions include the dehydrogenation of ethylbenzene to styrene, the Fishere-Tropsch synthesis for hydrocarbons, the oxidation of alcohols, and the large scale manufacture of butadiene [116]. All three forms of magnetic iron oxide are commonly used as synthetic pigments in paints, ceramics, and porcelain [117]. They possess a number of desirable attributes for these applications because they display a range of colors with pure forms, high tinting strength, stability and they are resistant to acids and alkalis. Pigments based on hematite are red, those based on maghemite are brown, and magnetite-based pigments are black [118]. These pigments are widely used in water-repellent stains for wood as they

enable the wood grain to be seen while still providing protection against the damaging effects of sunlight. Pigments made from magnetite are also used in magnetic ink character recognition devices, and superparamagnetic magnetite particles are used in metallography for detecting defects in engines. In the magnetic recording media application, the encapsulation of magnetic nanoparticles is critical in reducing interparticle interactions. The interparticle interactions tend to undergo uncontrolled aggregation under common preparation conditions. Hence, this is undesirable in recording media applications where a natural separation would help to safely attain the highest possible packing density to obtain media with lower cost per bit of information and to improve the signal to noise ratio [119].

3.2   Environmental applications

Iron nanoparticles technology is considered to be among the first generation of nanoscale environmental technologies [120, 121]. It has received considerable attention for its potential applications in groundwater treatment and site remediation. The reason is recent studies have demonstrated the efficacy of zero-valent iron nanoparticles for the transformation of halogenated organic contaminants and heavy metals such as chlorinated organic solvents, organochlorine pesticides, organic dyes, various inorganic compounds and metal ions such as As(III), Pb(II), Cu(II), Ni(II) and Cr(VI) [120]. This iron nanoparticles could provide cost-effective solutions to some of the most challenging environmental cleanup problems [122]. Recently, permeable reactive barriers have been developed, as alternatives for the conventional pump-and-treat technology, used to treat ground-water contaminated by different pollutants [123].

3.3   Biomedical applications

Nowdays, the biomedical use of magnetic nanoparticles becomes one of the most important applications. From the material science point of view, two key factors play an important role for these applications: size control and surface functionality. Even without targeting surface ligands, superparamagnetic iron oxide nanoparticles (SPIOs) diameters greatly affect in vivo biodistribution. Particles with diameters of 10-40 nm, including ultra-small SPIOs (USPIOs), are optimal for prolonged blood circulation. They can cross capillary walls and are often phagocytosed by macrophages which traffic to lymph nodes and bone marrow [124].

3.3.1   Drug Delivery

Drug targeting has emerged as one of the modern technologies for drug delivery. The possibilities for the application of iron oxide magnetic nanoparticles in drug targeting have increased in the recent years [125, 126]. Magnetic nanoparticles in combination with an external magnetic field in principle allow the delivery of particles to the desired target area and fix them at the local site while the medication is released and acts locally [125]. Transportation of drugs to a specific site can eliminate side effects and also reduce the dosage required. The surfaces of these particles are generally modified with organic polymers and inorganic metals or oxides to make them biocompatible and suitable for further functionalization by the attachment of various bioactive molecules [127].

3.3.2   Bioseparation

In biomedical research, separation of specific biological entities such as DNA, proteins, and cells from their native environment is often required for analysis. Superparamagnetic colloids are ideal for this application because of their on-off nature of magnetization with and without an external magnetic field, enabling the trans-

portation of biomaterials with a magnetic field. In a typical procedure for separation, the biological entities are labeled by superparamagnetic colloids and then subjected to separation by an external magnetic field [125]. Superparamagnetic iron oxide particles have been extensively used for separation and purification of cells and biomolecules in bioprocesses [125, 126]. Due to their small size and high surface area, magnetic nanoparticles have many superior characteristics for these bioseparation applications compared to those of the conventional micrometer-sized resins or beads, such as good dispersability, and the fast and effective binding of biomolecules.

3.3.3 Magnetic resonance imaging (MRI)

One of the promising applications of magnetic nanoparticles is the medical diagnostics. Superparamagnetic iron oxide (SPIO) nanoparticles are proving to be a class of novel probes useful for in vitro and in vivo cellular and molecular imaging. Superparamagnetic contrast agents have advantage of producing enhanced proton relaxation in MRI in comparison with paramagnetic ones. Consequently, less amount of a SPIO agent is needed to dose the human body than a paramagnetic one. To apply the magnetic fluids to a MRI contrast agent, a SPIO should be dispersed into a biocompatible and biodegradable carrier. Recently, Müller and co-workers [126] reviewed applications of superparamagnetic iron oxide nanoparticles as a contrast agent. Kim et al. [128] synthesized ferrofluids for MRI contrast agents by coating them with oleic acid as a surfactant and then dispersed them in the chitosan, which is a suitable carrier for bioapplications. They compared the MRI images of the ferrofluids with the images of Resovists® (a commercially available contrast agent for MRI). Their study showed that the ferrofluids exhibited enhancement of the MRI contrasts comparable to Resovist® in vitro. Wu et al. [129] prepared multifunctional nanoparticles which possess magnetic, longlife fluorescence and bio-affinity properties. They used the nanoparticles as label for time-resolved fluorescence cell imaging of Hela cells. They found that the time-resolved fluorescence imaging technique is fa-

vorably useful to eliminate the background noises caused by cells and matrix. These properties of the silica-based magnetic-fluorescent nanoparticles lead to application advantages in biological labeling and detection, cell separation with drug and gene delivery.

3.3.4 Magnetic hyperthermia

The heating power has very long history for treatment of different diseases. Nowadays, the heat treatment reveals the promising solution for cancer therapy aside from the well-known methods of surgery, chemotherapy, and irradiation. Much research has proven that high temperatures can damage and kill cancer cells with minimal damage to normal tissues [130, 131]. Such a therapy applies the fact that cancer tissue is more susceptible to heat [130] than healthy one. Therefore, increasing the temperature of the tumor tissue to more than 42°C yields selective damaging of cancer cells and renders them more sensitive to radiation and anticancer drugs. One of the advantages of magnetic nanoparticles that it can heat under applied AC magnetic field, which opens the oppertunity to use this heat for destroying the cancer cells. This new approach is called magnetic hyperthermia for cancer therapy. In the recent years, the main research on this kind of treatment has been focused on magnetic iron oxide nanoparticles [132] which already have revealed their feasibility in animals experiments [133]. Therefore, these particles are now under test for clinical uses [134]. Here, magnetic particles are introduced into the tumor tissue and exposed to external AC magnetic fields to increase the tumor temperature more than 42 °C. Consequently, large power losses of the magnetic materials are desirable in order to reduce the amount of material to be applied to a patient.

However, there are a lot of metals and magnetic alloys which can offer advantages over their oxides due to the high saturation magnetization. The latter potentially implies higher energy losses under applied AC magnetic field. Actually, the use of pure metal nanoparticles is hindered because of their oxidation in a biological envi-

ronment. For solving this problem, one can coat the metallic core with a protecting shell against oxidation. The types of possible shells have been explained in the previous chapter. In the work at hand, carbon shells have been used for avoiding the oxidation of the metallic cores in the biological environment while their magnetic properties were retained [132]. Moreover carbon shells allow to attach various functional groups which may increase the biocombatibility of the particles or enable loading of anticancer agents exohedraly.

3.3.4.1   Heating mechanisms

Heating of magnetic nanoparticles in an external alternating (AC) magnetic field may be related to several physical mechanisms such as ferromagnetic (hysteresis) losses, superparamagnetic (relaxation) losses, eddy currents, etc [135-141]. Note that magnetic particles used for the hyperthermia are too small and AC magnetic field frequencies are too low for the generation of any substantial eddy currents [40]. In addition the eddy current can be negligable where the size of the particles is below 1 micrometer [139]. Ferromagnetic particles reveal hysteretic properties in a time varying magnetic field. The hysteresis losses caused by repeated switching of the magnetization of the magnetic particles would lead to very efficient heating. The amount of dissipated energy in this case is given by the frequency f multiplied by the area of the magnetic hysteresis loop:

$$P = \mu_0 f \oint H dM. \tag{3.1}$$

However in order to produce heat in a single domain ferromagnetic nanoparticles the magnetic moment has to be switched by a magnetic field above the respective switching field, therefore no minor loops can be used for heating. For realistic materials, this can lead to rather high required AC magnetic field strengths, which is not always compatible to medical applications.

An alternative mechanism for magnetically induced heating is associated to superparamagnetic or relaxation losses. Note that the particles are usually dispersed in aqueous solution (ferrofluid) as medium in order to apply them in a biological environment. Ferrofluids are superparamagnetic at room temperature. For small magnetic field amplitudes, and assuming minimal interaction between magnetic nanoparticles, the magnetic properties of a ferrofluid depend on the particle size and size distribution. The magnetization of magnetic nanoparticles suspended in a fluid medium and subjected to an oscillating magnetic field $H = H_0 \cos \omega \tau$ can be expressed in terms of the complex susceptibility $\hat{\chi}$ and applied field frequency ω through [135]

$$M(t) \;=\; H_0(\chi' \cos \omega \tau + \chi'' \sin \omega \tau), \tag{3.2}$$

$$\hat{\chi} \;=\; \chi' - i\chi'', \tag{3.3}$$

where χ' is the in-phase component and χ'' is the out-of-phase component of the complex susceptibility $\hat{\chi}$. For an ensemble of particles with a single relaxation time τ, the Debye model for the dynamic susceptibility [135] yields

$$\chi' \;=\; \frac{\chi_0}{1 + (\omega \tau)^2}, \quad \chi'' \;=\; \frac{\omega \tau \chi_0}{1 + (\omega \tau)^2}, \quad \chi_0 = \mu_0 M_s^2 V/(k_B T). \tag{3.4}$$

Relaxation of the nanparticles's magnetization can occur through one of two mechanisms. In Brownian relaxation, characterized by the relaxation time τ_{B}, the magnetic dipole is locked in the particle which rotates as a rigid body together with fixed magnetization vector. In Néel relaxation, the magnetic dipole switches between so called easy axes inside a non-moving particle with characteristic time τ_{N}. In a typical superparamagnetic ferrofluid the Brownian and Néel relaxations processes take place in parallel and therefore the effective relaxation time can be given by:

$$\tau_{\mathrm{B}} \;=\; 4\pi\eta r_{\mathrm{h}}^3/(k_{\mathrm{B}}T), \quad \tau_{\mathrm{N}} \;=\; \tau_0 \exp\left[\frac{KV}{k_{\mathrm{B}}T}\right], \quad \tau_{\mathrm{eff}} \;=\; \frac{\tau_{\mathrm{N}}\tau_{\mathrm{B}}}{(\tau_{\mathrm{N}} + \tau_{\mathrm{B}})} \tag{3.5}$$

where r_h is the hydrodynamic radius of the particles, η is the viscosity of the surrounding fluid, τ_0 is a characteristic time, typically assumed to have the approximate value 10^{-9} s, K is the magnetocrystalline anisotropy constant of the magnetic nanoparticles, and V is the volume of the magnetic particle core.

The magnetic relaxation involves dissipative processes which can be distinguished by the frequency dependence of the imaginary part χ'' of the complex-magnetic susceptibility. From Debye theory [136], it is known that the relaxation time τ is correlated with the angular frequency ω at which χ'' has a maximum, by the relation: $\omega\tau = 1$. In the case of pure Néel relaxation, for example, if magnetic nanoparticles are bonded to a solid medium, the measurements of the magnetic response have two temperature regimes above and below the blocking temperature T_{B}. The relaxation of the magnetization of a single particle with anisotropy constant K is characterized by the Néel relaxation time τ_{N}. If the relaxation time is short enough and the particle can achieve the thermal equilibrium in the time of measurement, the particle is in the superparamagnetic state (above T_{B}). In the opposite case the so called blocked state (below T_{B}) is realised. Since different types of experiments have different time windows over which the magnetic response is detected, the blocking temperature of the magnetic particles directly depends on the measurement method, i.e. its characteristic frequency.

Depending on the actual material, an oscillating magnetic field induces movement of the magnetic nanoparticles and/or rotation of the magnetic moment inside the particle that compose the ferrofluid, which causes energy dissipation, commonly referred to as volumetric power dissipation (P) [135], or specific loss power (SLP) [137, 138]. Rosensweig [135] has deduced an expression that describes the energy dissipation of a ferrofluid in the presence of an oscillating magnetic field by considering the thermodynamics of the system. From this analysis the power dissipation (P) is expressed as

$$P = \mu_0 \pi \chi_0 f H_0^2 \frac{2\pi f \tau}{1 + (2\pi f \tau)^2}. \tag{3.6}$$

where $\omega = 2\pi f$ is the cyclic frequency.

The power dissipation can be related to the increase in temperature with time of heating, which is commonly referred to as the specific absorption rate (SAR). This thermal dissipation can be estimated from a calorimetric method, from which the mass normalized SAR (unit: $W/g_{particle}$) is expressed by [135, 139]

$$SAR = C \, \frac{m_{\text{part.Sol.}}}{m_{\text{part.}}} \, \frac{dT}{dt}\bigg|_{t \to 0} \tag{3.7}$$

Here, $m_{\text{part.}}$, $m_{\text{part.sol.}}$, and C are the mass of the magnetic particles, the mass of the particle solution, C the heat capacity of the solution and $(dT/dt)_{t=0}$ is the initial slope of the variation $T(t)$ of temperature as a function of time.

According to clinical criteria regarding safe-tolerance of human exposition to AC magnetic fields during a magnetic hyperthermia treatment, particular therapeutic conditions for appropriate magnetic field strength and frequencies have been determined. Hergt et al. [139, 142] have estimated the clinical use limitation of the product of field amplitude H and frequency f to be about $5.0 \cdot 10^9$ $Am^{-1}s^{-1}$ in order to obtain a maximum specific loss power avoiding clinical problems. For the same reason, a commercial prototype was developed by Jordan and co-workers for the generation of an AC magnetic field is suitable for MFH treatment on human patients [143, 144].

To summarize, several parameters influence the energy dissipation of magnetic nanoparticles during the application of a magnetic field such as size and size distribution of the nanoparticles [145-149]. This is related to the dependence of magnetic properties such as coercivity and relaxation on nanoparticle size [145].

Chapter 4

Experimental Techniques

In this chapter the used experimental setup for all the measurements is presented starting with the synthesis method and followed by the applied characterization techniques including those used for assessing their feasibility for magnetic hyperthermia.

4.1 Synthesis of nanoparticles

As described in the previous chapter, a variety of methods has been used in literature for the synthesis of magnetic nanoparticles. Among all these synthesis methods, CVD is one of the best choices because of its upward scalability, low cost, and rather low production temperatures in comparison to arc discharge and laser ablation and hence has been used in the work at hand.

4.1.1 High pressure chemical vapor deposition (HPCVD)

High pressure chemical vapor deposition technique has been used for synthesis of carbon coated magnetic nanoparticles whether it is pure elements or alloys. The idea of this method is similar to the idea of HiPco device which invented by Smalley 1999 [150]. HiPco idea has worked on producing single wall carbon nanotubes SWNTs by flowing CO mixed with a small amount of $Fe(CO)_5$ through a heated reactor.
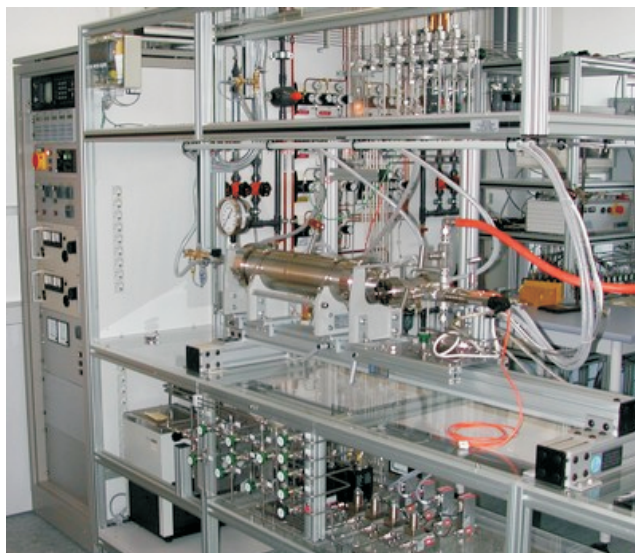
Figure 4.1: Experimental home made setup of high pressure chemical vapour deposition equipment (HPCVD).

The products of $Fe(CO)_5$ thermal decomposition (probably $Fe(CO)_n$, n= 0-4) react to produce iron clusters in gas phase. Fig.4.1. shows the experimental home made setup of HPCVD used for this process that is similar to the one used for the HiPco process [150].

In the work at hand, carbon coated Fe, Co, Ni, FeRu, CoRu, NiRu, NiPt, and CoPt magnetic nanoparticles have been synthesized using HPCVD. For production of the magnetic nanoparticles, the starting materials were metallocenes, such as ferrocene for Fe, Cobaltocene for Co, nickelocene for Ni, and Ruthenocene for Ru. In the case of Pt-containing alloys, metallorganic precursor which is trimethyl methylcyclopentadienyl platinum (IV) has been used. These precursors have been chosen because of their low sublimation and decomposition temperatures.

The main part of HPCVD device is the CVD reactor which consists of a quartz tube surrounded by an electrical heating element as shown in Fig. 4.2. Both the reactor and the quartz tube are placed within a thick-walled aluminum cylinder. The heating element itself and the space between the quartz tube and the inner wall of
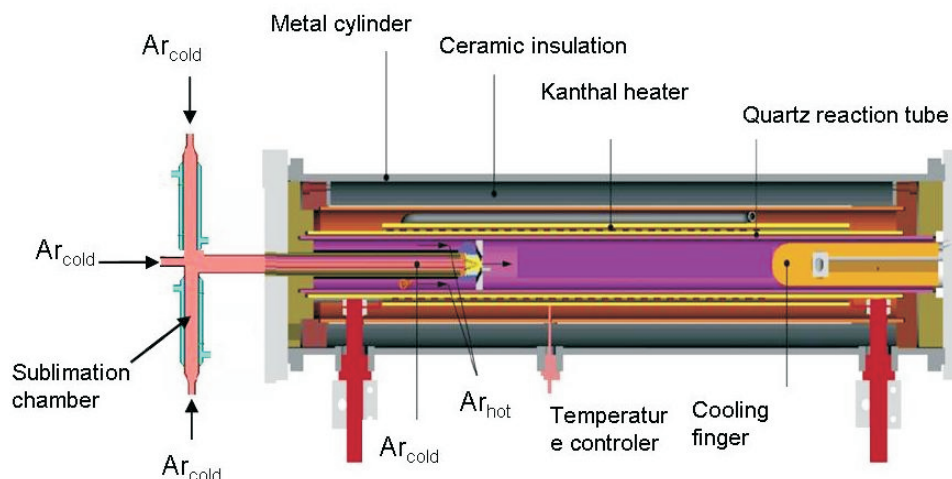
Figure 4.2: A parallel cross-section of the high-pressure CVD reactor [151, 152].

the aluminum cylinder reside under an atmosphere of argon maintained at slightly higher pressure than that inside the quartz tube. The material sources are placed into a thermostated sublimation chamber where the precursors can sublimate and become in the gas phase. The temperature of the sublimation chamber can be varied from room temperature to 200 °C. By means of argon gas flow (1400 sccm), the vapor enters the CVD reactor which consists of two different temperature zones. The first zone is called the hot zone, in which the reactions occur due to the thermal decomposition of the metallorganic precursors. The second zone is called the cold zone which consists of a copper finger connected to cooling water where the nanoparticles are deposited and collected. As explained in the previous chapter, supersaturation is required to induce homogeneous nucleation of particles. In the hot zone the precursors material enter the gas phase in order to generate a state of supersaturation. In order to control this part of the process and hence the entire synthesis process, three parameters have to be controlled: the temperature of the sublimation chambers as well as, the pressure and the temperature inside the CVD reactor. As will be pointed out in detail when discussing the experimental results, the effect of pressure change on the morphology and the properties of the synthesized alloys nanoparticles was

studied in particular detail. In addition, as trial for controlling the particle size and the composition of the alloys component, the metallorganic precursors are placed in a particular separated crucible located in a separated thermostated chambers and are sublimated and transported using high pressure argon gas flow into the reactor. Then, the effect of the sublimation temperature variation on the alloys composition, size distribution and average particle size is tested. The reason for using a high pressure of argon gas is that the frequent collisions of the gas atoms decrease the diffusion rate of atoms away from the source region. The collisions, and the Ar-flow cool the atoms. If the diffusion rate is not sufficient, then supersaturation will not be achieved and individual atoms or very small clusters of atoms will be deposited on the cooper finger. So, the high pressure is necessary for achieving the supersaturation [153]. It was found that, the optimal temperature and pressure to obtain carbon coated spherical nanoparticles amounts to be $T = 900$ °C, $P = 13$ bar or higher.

4.2 Characterization of nanoparticles

4.2.1 X-Ray diffractometer

A Miniflex X-ray diffractometer (XRD)(Philips Company, Eindhoven, Netherlands) with Cu Kα radiation was used for determining the crystallographic parameters of the produced material such as, crystal structure, the phase analysis of the synthesized samples and estimation of the mean particle size based on the broadening of the peaks in the XRD profile using the Scherrer equation [154]. The broadening of the diffraction peaks is related to the small particle size.

$$D_{\mathrm{XRD}} = \frac{K\lambda}{\Delta\, 2\theta_{\mathrm{hkl}}\cos\theta_{\mathrm{hkl}}} \qquad (4.1)$$

This equation is often used to calculate the average particle diameter D (in nm), where θ_{hkl} is the angle of a particular diffraction peak, $\Delta\, 2\theta_{\mathrm{hkl}}$ is the width at half maximum (FHWM) of the respective XRD peak, λ is the wavelength of the applied X-ray radiation Cu-Kα (in nm) and K is a constant which is very close to unity and is related to the crystallite shape.

4.2.2   Scanning electron microscope (SEM)

Scanning electron microscopy (SEM) analysis was performed by means of a Nano-SEM 200 device with acceleration voltage of 15 kV. SEM is a widely used technique for the determination of morphology and size distribution of particles in the scales of micro to nano range. The resolution of the SEM is relatively low compared to transmission electron microscopy and it is not efficient for visualizing nanoparticles with particles size lower than 20 nm. In the work at hand, the SEM has been used as a tool to initially study the shape and structure of the synthesized magnetic nanoparticles.

4.2.3   Energy dispersive X-ray (EDX) analysis

An EDAM III energy dispersive X-ray analysis (EDX) unit has been used to provide elemental analysis and determination of the chemical composition of the prepared magnetic nanoparticles. From EDX data, the ratio of the elements in the alloys nanoparticles structure can be estimated [Done with the help of Frau. S. Pichl].

4.2.4   Transmission electron microscope (TEM)

High resolution transmission electron microscopy (HRTEM) images were realised by means of a FEI Tecnai F30 TEM with field emission gun at 300 kV. HRTEM is commonly used for characterization of core/shell nanoparticles. A provided infor-

mation about the core size (crystalline and amorphous parts), the thickness and the structure of the shell. Furthermore, it provides details regarding the size distribution and the shape for small particles (below 20 nm). However, this technique needs an analysis by image treatment, and must be performed on a statistically significant large number of particles [Done by Frau. G. Kreutzer].

4.2.5 Alternating gradient magnetometer (AGM)

For investigation of the magnetic behavior of the synthesized magnetic nanoparticles as powder at room temperature, a PMC MicroMag-2900 alternating gradient magnetometer (AGM) has been used. AGM is powerful tool to measure the sample's net magnetization as afunction of the external magnetic field at room temperature. The alternating field gradient exerts an alternating force on the sample proportional to the magnitude of the gradient field and the magnetic moment of the sample. The mass of the magnetic nanoparticles powder is measured and then the powder is fixed with non magnetic glue on a glass extension and put in the magnetic field of the AGM. From this measurement, one can get information on the uniform (DC) magnetic response of the sample such as its magnetization, the remanence and the hysteresis behaviour. The external magnetic field can vary for the used AGM within $\pm$ 1 T. Based on the obtained AGM curve at room temperatures, the magnetic behaviour of the synthesized magnetic nanoparticles can be identified. In particular the saturation magnetization M_S can be determined from the plateau part of the $M - H$ curve.

4.2.6 Squid magnetometer (SQUID)

The temperature dependence of the magnetization at constant magnetic field in the temperature range 5 to 400 K was studied using a Superconducting Quantum Interference Device Magnetometer (VSM-SQUID) from Quantum Design. The samples
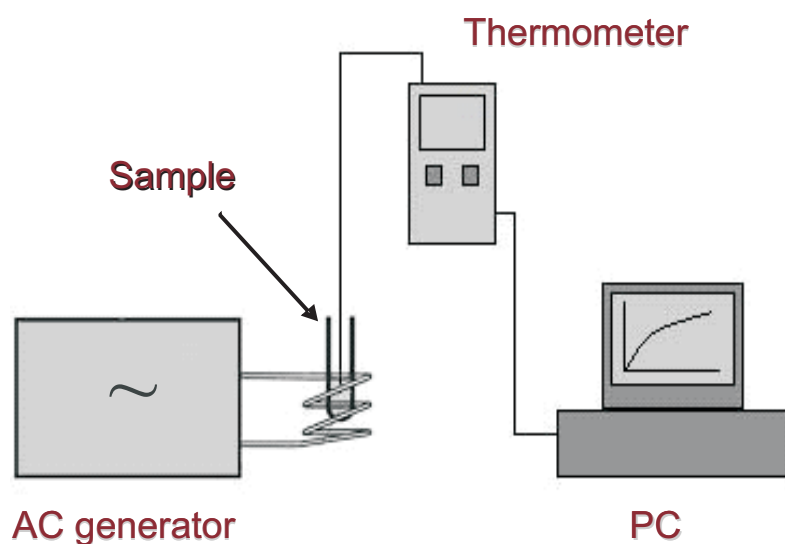
Figure 4.3: Schematic experimental setup for heating experiments.

have been investigated as dry powders. Magnetization measurements as a function of temperature on materials cooled with (FC) or without (ZFC) an applied magnetic field followed by heating the particles in the presence of a magnetic field allows to determine the characteristic blocking temperature T_{B} of superparamagnetic particles. In the case of ZFC magnetization measurements, the sample was firstly heated from room temperature up to 400 K, then cooled down to 5 K in zero magnetic field. Then, after applying the magnetic field, the magnetization measurements were performed up to 400 K. For FC magnetization measurements, the sample was cooled in the same magnetic field down to 5 K and the magnetization was measured in the warming cycle up to 400 K under applied magnetic field.

4.2.7   Alternating frequency generator (AFG)

A Hüttinger TIG 5.0/300 oscillator and AC/DC power supply have been used for measurement of the heating effect of magnetic nanoparticles in alternating magnetic fields as shown in Fig. 4.3. The AFG consists of a high frequency generator with a water-cooled magnetic coil system providing alternating magnetic fields with the

frequency $f = 120$ kHz and the magnetic field strength of 0 - 100 kA/m. Here the induced heating effect of magnetic nanoparticles in liquid medium was studied. In order to obtain a stable suspension, magnetic nanoparticles were mixed with human albumin solution and dispersed using ultra sonicator. The temperature change per time was detected using a fiber-optic temperature controller (Luxtron One), which is suitable for measurements at high frequency magnetic fields.

Chapter 5

Carbon coated Fe, Co and Ni nanoparticles

Although there is many methods have been developed for synthesis and morphological controls of nanoparticles, rods, and wires of semiconductors, carbon encapsulated magnetic nanoparticles and metal oxides, only limited success has been made in making small and uniform spherical nanoparticles with narrow size distribution [155-182]. It is therefore desirable to use smaller nanoparticles that have enhanced magnetic properties. In addition, understanding details of nano-scaled magnetic materials in complex core/shell structures is interesting from a fundamental materials science point of view since tailoring their magnetic properties requires understanding of the size effects on the relevant parameters [183]. However, several problems have to be solved before using these materials for applications [184,185]. Hence, this chapter introduces a complete study from the fundamental point of view for synthesis to the investigation of the physical properties and feasibility for hyperthermia therapy for carbon encapsulated pure Fe, Co, and Ni nanoparticles. The results of this chapter have been published in Ref. [186].

5.1   Nanoparticles synthesis

Synthesis of the carbon coated Fe, Co and Ni nanoparticles (Fe@C, Co@C, and Ni@C respectively (done by E. Ibrahim)) has been carried out by means of the high pressure chemical vapour deposition HPCVD process using ferrocene, cobaltocene and nickelocene, respectively, as precursors. The construction of the equipment has been described in chapter 4. Briefly, the corresponding metallocene is sublimated in a thermostated chamber at 95°C and transported using argon gas flow (1400 sccm) into the reactor. Due to the high flow rate of the carrier gas, the synthesized material transfers from the reaction zone and deposits on the cooling finger surface. It was found that, for given argon flow rate, temperature and pressure are crucial to obtain pure carbon coated materials. At low temperature and pressure, it was found the formation of carbon nanotubes attached to magnetic particles. By increasing the pressure and the temperature inside the reactor, the formation of the spherical magnetic particles coated with carbon have been achieved. Therefore the optimum pressure and temperature inside the CVD reactor have been found at 13 bar and 800 °C, 900 °C, 900 °C for synthesis of Fe@C, Co@C, and Ni@C respectively.

5.2   Result and discussion

5.2.1   Morphology and structure

After particles synthesis, the samples were characterized by scanning electron microscopy (SEM), transmission electron microscope (TEM), and X-ray diffraction patterns (XRD). Fig. 5.1(a-c) shows SEM images of the synthesized Fe@C, Co@C, and Ni@C nanocapsules, respectively. All images indicate the formation of spherical nanostructured material. As will be proven by the TEM images below, the particles exhibit a core-shell structure with carbon coating. Fig. 5.1(a) assumes the presence of amorphous carbon between the nanosized particles which is clear more
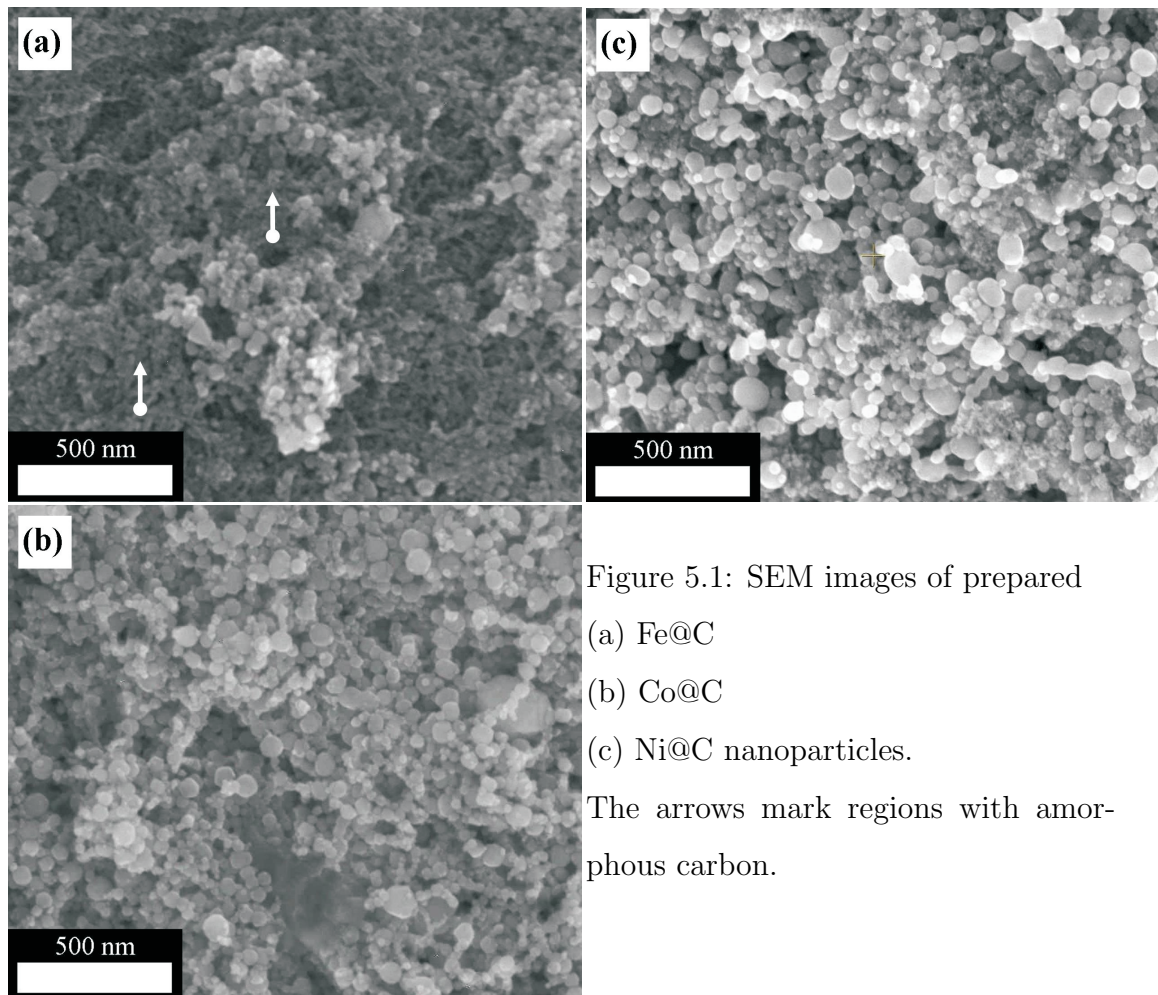
Figure 5.1: SEM images of prepared

(a) Fe@C

(b) Co@C

(c) Ni@C nanoparticles.

The arrows mark regions with amorphous carbon.

in Fig. 5.1(a) (white arrows) while no clear information about amorphous carbon can be extracted from Fig. 5.1(b,c). More detailed information can be achieved by Raman spectroscopy which was applied for investigating the crystallinity of carbon in our materials. Both the so-called G-line and D-line are found in our analysis. The Raman-active tangential G-line is observed around 1600 cm^{-1}. It can be associated to the E_{2g}-mode in graphite and thus implies the presence of graphitic carbon. The so-called D-line around 1300 cm^{-1} is known to raise a defect induced double Raman scattering process [155, 156] thereby providing direct insight into the defect concentration. It disappears for perfect carbon crystals [157]. Therefore, the ratio D/G provides information about the presence and crystallinity of carbon. For our Fe@C, Co@C, and Ni@C samples we find D/G ratios of 0.86, 0.40, and 0.78, respectively,

indicating both graphite and amorphous carbon in our samples. The data imply that Co@C exhibits the best crystallinity among our materials.In addition, in the upper right part of Fig. 5.1(a) there are some chain-like particles.

The detailed morphology of the coated particles was studied with TEM. Representative TEM images are shown in Fig. 5.2(a, b, d, e, g, h) together with the resulting size distribution based on the TEM analysis presented in Fig. 5.2(c, f, i). Note, that the material under study is magnetic which reduces the resolution of the images. As shown in the top panel of Fig. 5.2, a majority of the material exhibits the desirable core/shell structure of carbon coated metallic nanoparticles. In few cases, however, as highlighted (white circle) in Fig. 5.2(a) also carbon particles without metallic cores have been formed. A typical example of the desired core-shell Fe@C particles is displayed in Fig. 5.2(b) which shows a spherical Fe nanoparticle of about 24 nm coated by 5 nm of carbon. The average size of the Fe particles in Fe@C amounts to 22 nm with a size distribution in the range 2-58 nm as presented in Fig. 5.2(c). The thickness of the carbon layers encapsulating the core particles amounts to 3-7 nm. In the cases of Co@C and Ni@C the carbon shells are rather similar to Fe@C, but the core size distribution is slightly different. To be specific, for Co@C and Ni@C, a core size distribution in the range of 4-100 nm and of 5-50 nm, with average diameters of 27 nm and 20 nm, respectively have been observed (Fig. 5.2(f, i)). In addition to spherical carbon-coated metal particles, some amount of amorphous carbon are found (top panel of Fig. 5.2). Moreover, the images in the middle panel of Fig. 5.2 imply the presence of more than one metal particle in the same shell.

In the following, the results of XRD studies are presented. Diffraction patterns of the three materials under study are displayed in Fig. 5.3. Note, that none of the XRD patterns exhibits characteristic peaks of related oxides. In contrast, the observed peaks confirm the metallic phase of the respective transition metals. For Fe@C, we observe diffraction peaks at $2\Theta = 43.4°$ and $44.6°$ which are characteristic
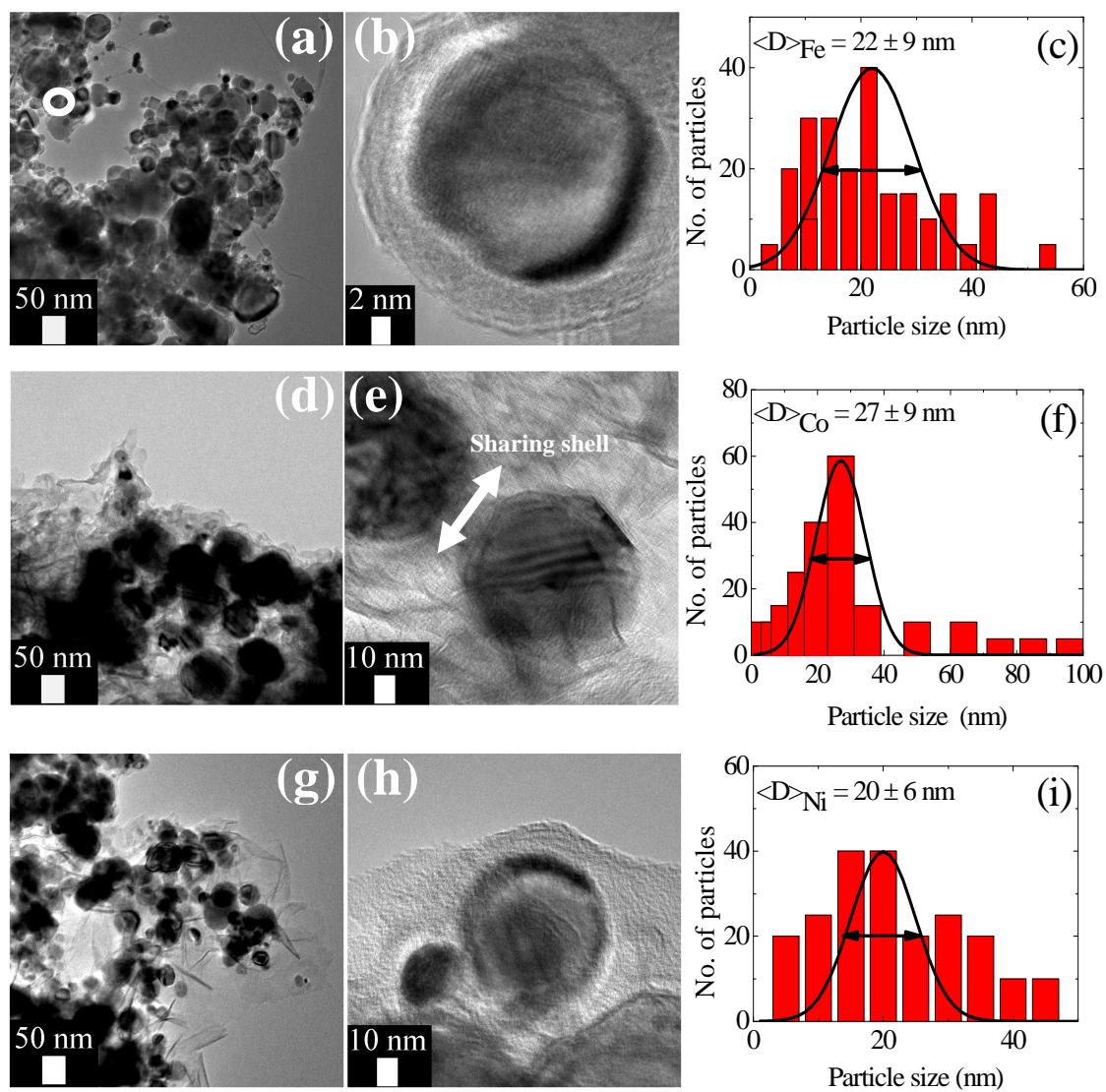
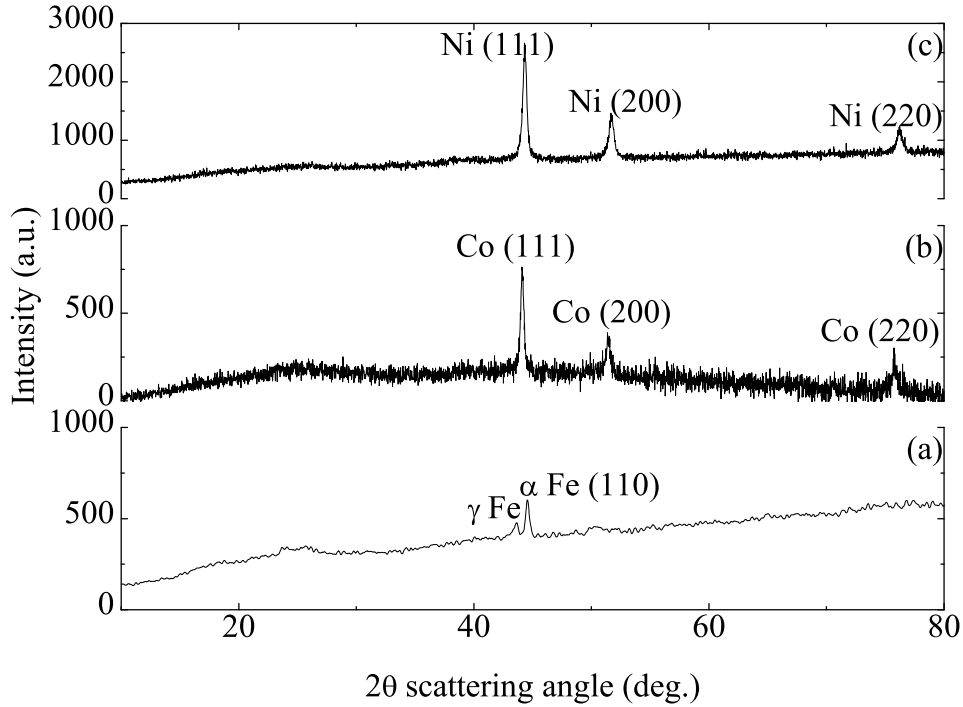Figure 5.2: TEM images and average size distribution of Fe@C (a, b, c), Co@C (d, e, f) and Ni@C (g, h, i).

Figure 5.3: X-ray diffraction spectra of (a) Fe@C , (b) Co@C and (c) Ni@C nanocapsules.

of α-Fe and γ-Fe, respectively. Analogously, the structure of the core materials is also confirmed for Co@C and Ni@C as proven by Co (111), (200), and (220) peaks at 44.1°, 51.5° and 75.7°, respectively, and Ni (111), (220), and Ni (200) peaks at $2\Theta = 44.3°$, 76.2° and 51.7°, respectively. The width of the characteristic diffraction peaks is affected by the average diameter of the nanoparticles. To be specific, the Scherrer equation Eq. 4.1 [154] allows to estimate the average particle size D_{XRD} dependent on the full width at half maximum of the characteristic peak for each sample. According to Eq. 4.1, the peak widths in Fig. 5.3 yield average diameters of around 16 nm, 21 nm, and 19 nm for Fe@C, Co@C, and Ni@C, respectively. These values fairly agree to the results of the TEM analysis. Note, however, that both results can not be compared straightforwardly since XRD can not detect very small particles and measures the bulk of the samples while the TEM analysis provides

information about a finite number of about hundred particles visible (i.e. not too thick) in the electron microscope.

5.2.2 Magnetic Properties

The magnetic properties of the prepared samples have been investigated by studies of the field dependence of the magnetization at room temperature and of its temperature dependence at constant external magnetic field. In Fig. 5.4 the full hysteresis loops of the magnetization in external fields up to 1T are presented for the three materials under study. For all samples, the data imply a ferromagnetic behavior as indicated by the open hysteresis loops, i.e. the presence of a remanent magnetization M_r. The ferromagnetic behavior is confirmed by the saturation of the magnetization curve in rather small external magnetic fields at room temperature. The quantitative analysis yields the saturation magnetization M_S of 79 ± 5, 158 ± 7 and 32 ± 7 emu/g for Fe@C, Co@C and Ni@C, respectively, while the remanent magnetization values amount to 16, 21 and 2 emu/g, respectively. Corresponding to the presence of a spontaneous magnetic moment there are finite coercive fields H_C which amount to 441 Oe (Fe@C), 249 Oe (Co@C) and 54 Oe (Ni@C). The comparison with the magnetization of the bulk materials allows estimating the mass ratio of the magnetic material in the carbon coated particles. Note that surface enhancement of the magnetization is expected to be insignificant due to the rather large size of the metallic cores. In addition the tiny diamagnetic response of the carbon shells is neglected [187, 188]. The metal mass ratio is about 36 %, 97 % and 55 % of the total sample mass was estimated for Fe@C, Co@C and Ni@C, respectively.

Our data indicate a particularly small hysteresis and a low critical field H_C for Ni@C. In bulk samples, where the particle size strongly exceeds the domain wall width, magnetization reversal is related to domain wall motion. As domain walls move through a sample, they can become pinned at grain boundaries, and additional energy is needed to continue moving. Pinning is one of the main sources of the
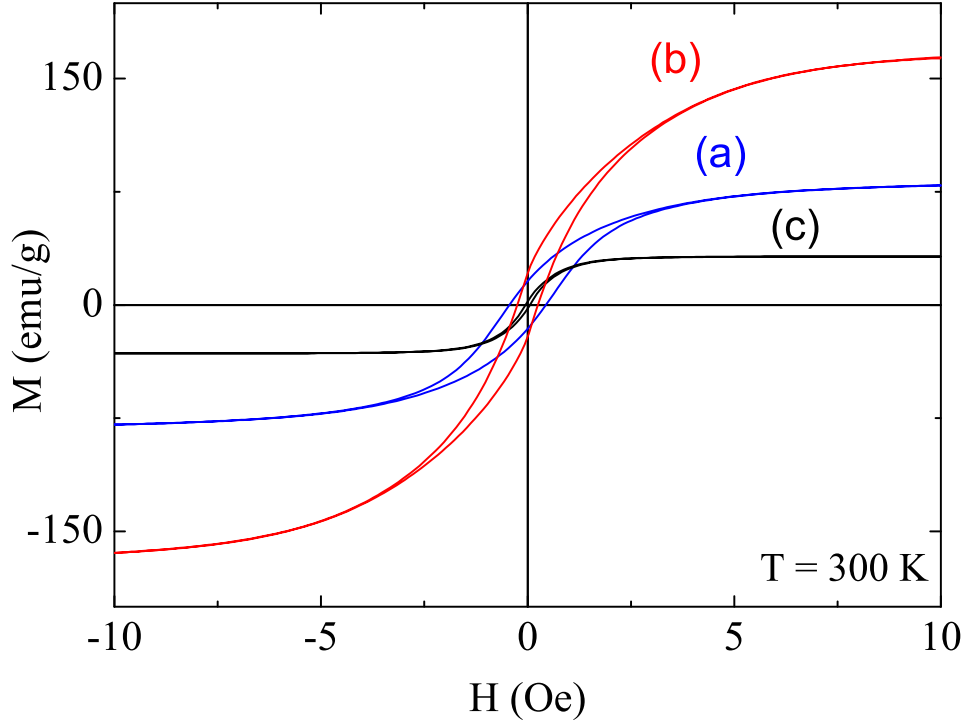
Figure 5.4: Hysteresis loops at room temperature of (a) Fe@C, (b) Co@C and (c) Ni@C nanoparticles.

coercivity [189]. Therefore, reducing the grain size in general is expected to create more pinning sites and to increase H_C. This is true for larger grain sizes, but below a certain value, H_C decreases rapidly. This threshold is the maximum size, D_C, for which coherent magnetization reversal of a single magnetic domain is feasible. The critical size is predicted to be $D_C = \pi S [J/K a_o]^{1/2}$, where S is the spin moment per atom, J is the exchange energy density, K is the magnetocrystalline anisotropy and a_o is the lattice constant [190]. Quantitatively, D_C amounts to 15, 15, 55 nm for Fe, Co and Ni, respectively [191]. In particles with $D < D_C$, the critical field H_C will decrease rapidly as the particle size decreases ($H_C \propto D^6$) [192]. In the materials at hand, the case of $D < D_C$ is realized only for Ni@C which is consistent with the observed small hysteresis. On the other hand, theory predicts ($H_C \propto D^{-1}$) for $D > D_C$ [192], which is found in our Fe@C and Co@C samples. The data in

Fig. 5.4 clearly imply a ferromagnetic behavior at room temperature. If at all, superparamagnetic behavior evolves at higher temperatures. In order to answer this question, the temperature dependence of the magnetization have been measured as presented in Fig. 5.5. Here, the samples were firstly cooled in zero magnetic field to 5 K and then a magnetic field of 10 Oe or 100 Oe was applied to the samples. In such a "zero field cooled" (ZFC) condition the measurements were performed upon heating up to 400 K. In contrast, "field cooled" (FC) data were obtained after cooling the sample in the same field which was used for the actual measurements.

As seen in Fig. 5.5 (black arrows), the ZFC magnetization increases rapidly upon heating for low temperatures below $\sim$ 75 K (Fe@C), $\sim$ 50 K (Co@C) and $\sim$ 25 K (Ni@C). At higher temperatures (red arrows), there is a region of linear increase and a sharper upturn around 400K. The ZFC magnetization is lower than the FC magnetization in the whole temperature range under study, i.e. ferromagnetism is present up to at least 400 K. For higher temperatures, due to the small size of the particles we expect superparamagnetic behavior. In this scenario, the expected blocking temperature T_B would be higher than 400 K. In a simple quantitative model, T_B amounts to $T_B = KV/25k_B$, where KV is the anisotropy energy barrier, K is the effective anisotropy constant and V is the volume of the magnetic particle [193]. Our observation of $T_B > 400$ K hence allows an estimate of the lower value of the particles mean diameter D, i.e. the data imply $D > 18$, 9 and 39 nm for Fe, Co and Ni, respectively. One might speculate whether the sharp increase of the ZFC magnetization at very low temperatures is also related to blocking of superparamagnetic particles, i.e. of smaller particles whose blocking temperatures T_B are in the temperature range of the kink in ZFC curve. This interpretation would imply the presence of particles with $D = 10$, 4 and 15 nm for Fe, Co and Ni, respectively. The magnetic studies provide indirect information about the amount of magnetic material (as deduced from M_S) and the average particle size (from T_B, H_C). It is hence reasonable to compare our results to materials produced by the arc plasma and combustion synthesis method
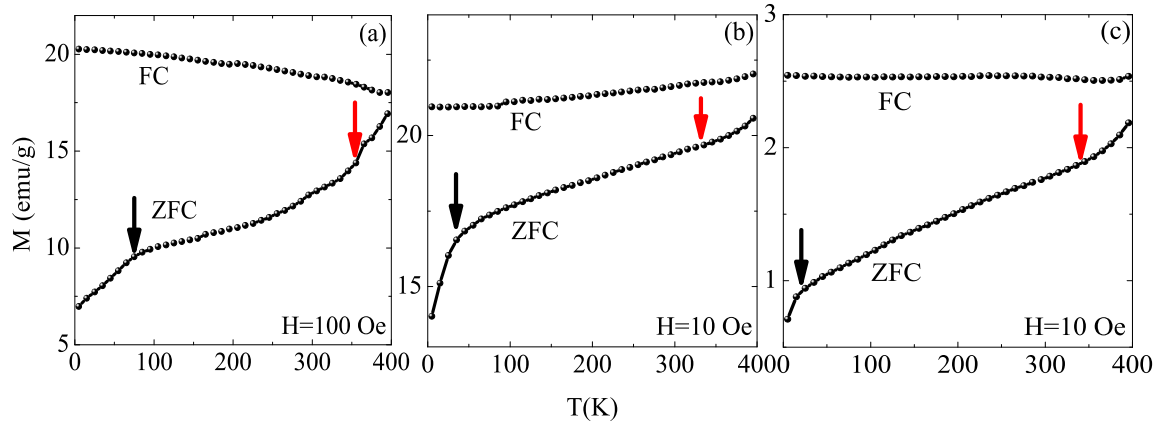
Figure 5.5: Zero-field-cooled (ZFC) and (H = 100 or 10 Oe) field-cooled (FC) magnetization curves of nanocapsules. (a) Fe@C, (b) Co@C and (c) Ni@C. The magnetization is normalized to the mass of the magnetically active materials as determined by analysis of hysteresis curves.

[79]. As seen in Table 5.1, the Fe@C sample produced using HPCVD exhibits larger values of M_{S} and H_{C}. While larger M_{S} directly implies a larger relative amount of Fe in our material, the larger value H_{C} provides evidence that our particles are smaller than the ones from Ref. [79]. Quantitatively, the relation $H_{\mathrm{C}} \propto D^{-1}$ implies that the cores of the material made by the arc plasma method are twice as large as the ones made by our HPCVD technique.

Table 5.1: Comparison of magnetic parameters at T= 300 K for Fe@C synthesised by different methods

Fe@C synthesis methods	D_{TEM} (nm)	H_C (Oe)	M_s (emu/g)
HPCVD	2-55	441	79
Arc Plasma [79]	10-100	200	53
Combustion [79]	10-100	4	11

5.2.3   Heating in AC magnetic fields

In the following section the feasibility of Fe@C, Co@C and Ni@C for magnetically induced heating is studied. In contrast to the measurements presented above, the following experiments have been performed by means of dispersed particles in an aqueous solution. In order to prepare the dispersions, human albumin has been used as a biocompatible surfactant. The particles were dispersed in a water-albumin solution using a tip sonicator for 2 minuets (10 sec on, and 1 sec off). The concentration of the particles was chosen to be 6 mg/ml and 8 mg/ml for Co@C and Ni@C respectively. The concentration of albumin in the water was in both cases approximately 5 mg/ml. Fe@C where the feasibility for magnetic hyperthermia could not be shown as discussed below. The heating effect of the particles dispersion in AC magnetic fields was studied by means of a high frequency generator with water cooled magnetic coil system. AC magnetic fields with a frequency of 120 kHz and magnetic field strengths of 0 - 100 kA/m were applied to the samples. The temperature of the sample was measured by a fiber-optical temperature sensor.

Fig. 5.6(a , c) present time-dependent calorimetric measurements at different applied magnetic fields for Co@C and Ni@C. For both samples, a significant heating effect is observed at applied magnetic fields > 25 kA/m. At the maximum applied magnetic field of 80 kA/m, the heating rate reached values of 7 °C/min and 11 °C/min for Co@C and Ni@C, respectively. The heating effect of Co@C is lower than of Ni@C although the former sample is supposed to have 97% of magnetic material and the Ni@C one only 55%. Such effects might occur if the Co particles are agglomerated stronger than Ni which can imply a different mechanism of magnetic induced heating. Possible mechanisms will be discussed later. In contrast, no heating was observed when the suspension of Fe@C is exposed to AC magnetic fields. Based on the present data one can not judge whether this is due to the agglomeration of Fe@C to larger magnetic agglomerates in the suspension or caused by a considerable amount γ-Fe particles in the material which is paramagnetic at room temperature
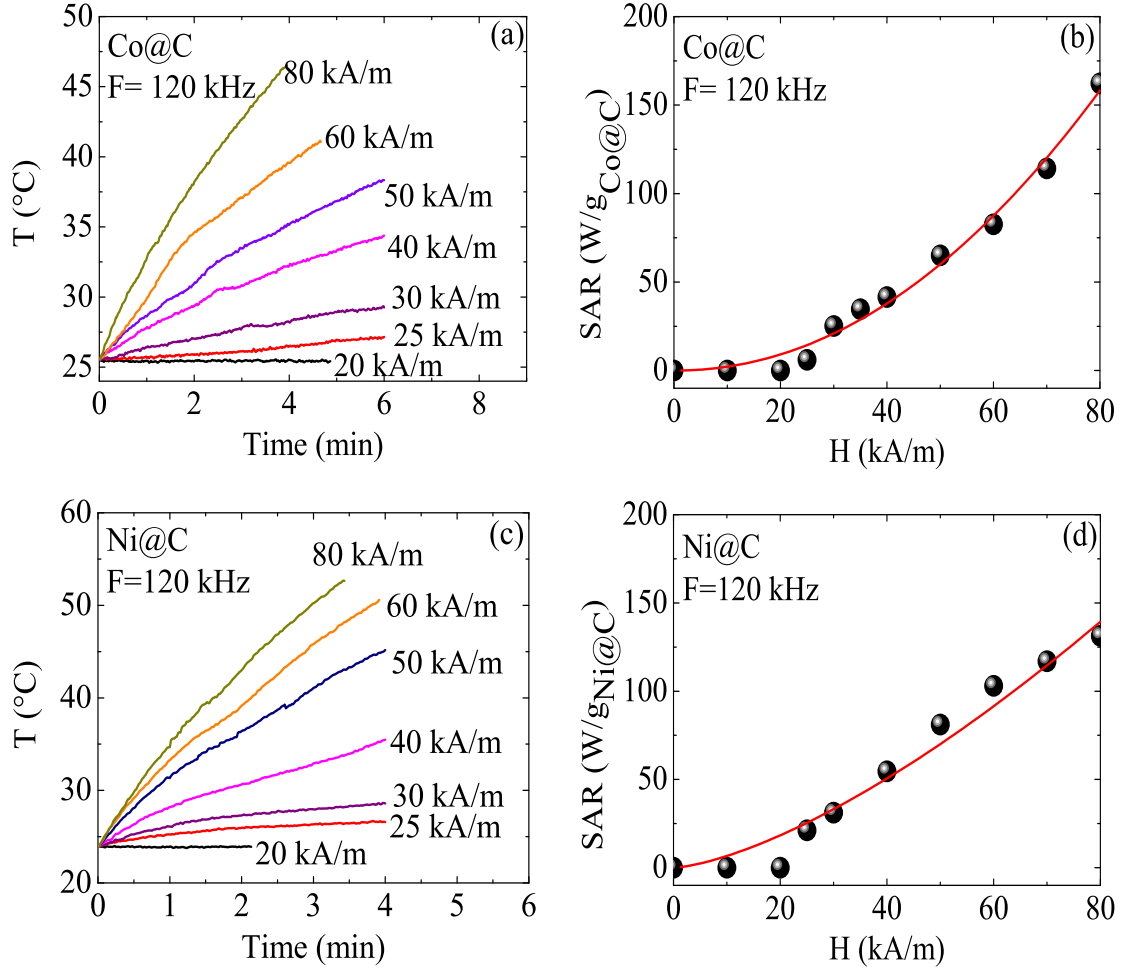
Figure 5.6: Temperature versus time upon application of AC magnetic fields and corresponding SAR values for (a, b) Co@C and (c, d) Ni@C.

and hence does not contribute to the heating process. In the following, the results for Co@C and Ni@C will be described.

Heating effectiveness of magnetic particles in AC magnetic fields is usually described in terms of the specific absorption rate (SAR). The SAR expresses the heating ability of a magnetic material and, therefore, the feasibility of a material for application in magnetic hyperthermia. The SAR value is calculated from the initial slope of the T versus t curves using Eq. 3.7 [135, 139, 194] and C the heat capacity of water ($C = 4.118$ Jg^{-1}K^{-1}). Fig. 5.6 (b, d) shows the magnetic field dependence of

the SAR for Co@C and Ni@C. At the maximum applied magnetic field of 80 kA/m, the SAR values of 162 W/g$_{Co@C}$ and 131 W/g$_{Ni@C}$ are found for Co@C and Ni@C, respectively. The observed quadratic field dependence is in agreement with the fact that the dissipated magnetic energy is proportional to H^2. Heating of magnetic particles in an alternating magnetic field may be understood in terms of several types of energetic barriers which must be overcome for reversal of the magnetic moments [194]. With decreasing particle size, these barriers decrease and the probability of jumps of the spontaneous magnetization due to the thermal activation processes increases, i.e. superparamagnetism evolves. The relatively broad size distribution in the samples implies both superparamagnetic and ferromagnetic particles at room temperature. Hence different heating mechanisms might appear concomitantly from which Néel and Brownian relaxation are expected to be the relevant processes for the observed power absorption as explained before in chapter 3 [25, 135, 195].

5.3   Conclusions

Fe@C, Co@C and Ni@C nanocapsules as produced by high pressure chemical vapour deposition (HPCVD) have been investigated with respect to their structural and magnetic properties. The SEM and TEM studies show that carbon coated particles with Fe, Co, and Ni core are formed with a size distribution from few to tens nanometers. X-ray diffraction was applied to confirm the phase of the core material. The size of the core particles has been deduced from TEM and from the width of the XRD peaks. The coated nanoparticles are ferromagnetic up to 400 K. AC magnetic heating studies of the dispersed nanoparticles yield the maximum SAR of 162 W/g$_{Co@C}$ and 131 W/g$_{Ni@C}$ at 80 kA/m and 120 kHz. The corresponding heating rates amount to 7 °C/min and 11 °C/min for Co@C and Ni@C, respectively.

Chapter 6

Carbon coated FeRu, CoRu, NiRu nanoalloys

The synthesis of metal nanoparticles of definite size and shape remains a challenging problem. This is even more difficult to synthesize bimetallic nanoparticles taking into account the size, shape, and composition must be controlled. However, recently alloy bimetallic nanoparticles have been extensively studied because they can exhibit unique electronic, optical, and catalytic properties that are absent in corresponding monometallic nanoparticles. Furthermore, the addition of second metal provides a method to control the chemical and physical properties of nanoparticle. In the last decades, the 4d transition metals Ru, Rh, and Pd and 3d transition metals Ni, Co, and Fe and their alloys have been the focus of both experimental and theoretical investigations. Because of there is only few literatures which have dealt with such nano-scaled alloys (nanoalloys), this chapter reports the synthesis of carbon coated FeRu, CoRu, and NiRu nanoalloys and the investigation of their properties have been discussed in details. Some of these results have been published in Ref. [196].

6.1   Nanoalloys synthesis

As mentioned in the previous chapter the high pressure chemical vapour deposition process (HPCVD) has been applied for the synthesis of carbon coated pure metals. It was also a challenge to use the same device for synthesis of carbon coated FeRu, CoRu, and NiRu nanoalloys. Here, ferrocene, cobaltocene, nickelocene and ruthenocene as precursors have been used for the nanoalloying constituents Fe, Co, Ni and Ru, respectively. The Fe:Ru, Co:Ru, and Ni:Ru metallocene powders with a weight ratio of 2:1 were positioned in a separated crucible located in a thermostated chamber at 95 °C, and are sublimated and transported using argon gas flow (1400 sccm) into the CVD reactor. It was found that, for all experiments Ar flow rate was fixed at 1400 sccm, temperature (T) and pressure (P) inside the reactor were varied from 200-1000 °C and 5-40 bar respectively. The optimal temperature for obtaining spherical particles has been found to be T = 900 °C for synthesis of FeRu@C, CoRu@C, and NiRu@C. In order to investigate more different compositions of the alloys the pressure inside the reactor has been varied in the range after the optimum pressure which is used for production of spherical particles. As will be shown in detail below, the variation of the pressure affects the amount of Ru inside the alloy as well as the amount of carbon in the whole material.

6.2   Result and discussion

6.2.1   Morphology and structure

The synthesized particles have been characterized using SEM which reveals the formation of spherical nanoparticles for all synthesized samples as displayed in Fig. 6.1(a, b, c). The composition of the resulting material was investigated by EDX. In general, the synthesis process yields carbon coated FeRu, CoRu, and NiRu nanoalloys (FeRu@C, CoRu@C, NiRu@C) with different compositions as listed in table 6.1,
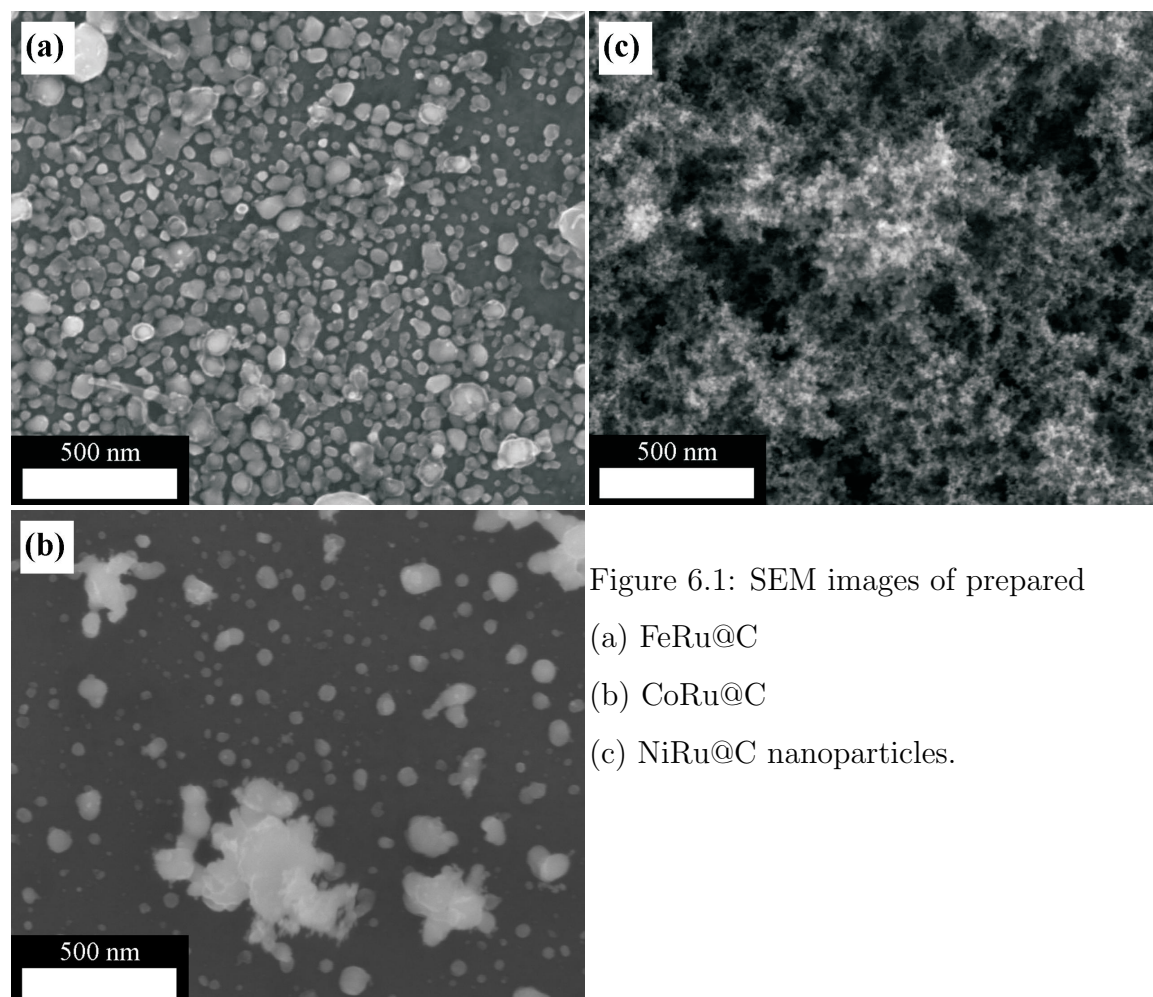
Figure 6.1: SEM images of prepared

(a) FeRu@C

(b) CoRu@C

(c) NiRu@C nanoparticles.

6.2, 6.3 for FeRu@C, CoRu@C, and NiRu@C respectively. For each batch, several EDX measurements were done at different positions of the sample in order to get average values for the core composition. As shown in table 6.1, 6.2, and 6.3 the data imply that moderately increasing the pressure yields a higher Ru content in the produced FeRu, CoRu, NiRu alloys respectively. Also, the carbon contents in the material have been observed to be increased when the pressure have been increased.

The morphology of the coated particles was studied by HRTEM which in general confirms a nanostructured material exhibiting the core/shell structure Fig. 6.2(a, d, g). A typical example of FeRu@C, CoRu@C, and NiRu@C is displayed in Fig. 6.2(b, e, h) which shows a spherical FeRu, CoRu, and NiRu core of about 26, 23, and 22 nm respectively, and a carbon shell of about 3 nm.
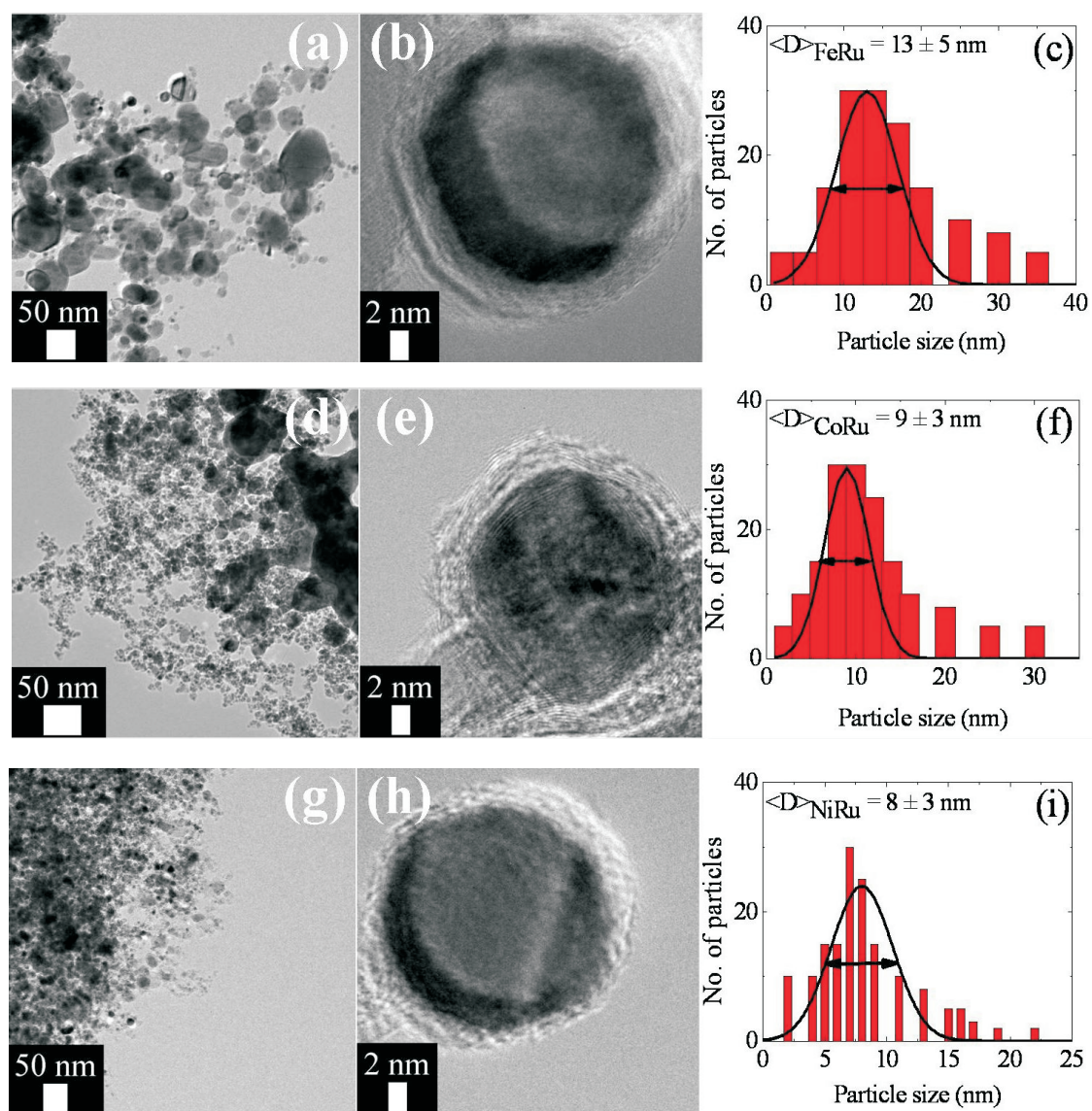
Figure 6.2: TEM images and average size distribution of FeRu@C (a, b, c), CoRu@C (d, e, f) and NiRu@C (g, h, i).

Table 6.1: Composition of the FeRu@C nanostructures synthesized at different pressures as determined by EDX analysis.

Pressure (bar)	13	21	26
Ru (wt%)	17 ± 1	28 ± 2	41 ± 2
$Fe_{100-x}Ru_x$ (x in wt%)	$Fe_{83}Ru_{17}$	$Fe_{72}Ru_{28}$	$Fe_{59}Ru_{41}$
C (wt%)	18	30	57

Table 6.2: Composition of the CoRu@C nanostructures synthesized at different pressures as determined by EDX analysis.

Pressure (bar)	13	21	26
Ru (wt%)	31 ± 1	38 ± 3	39 ± 5
$Co_{100-x}Ru_x$ (x in wt%)	$Co_{69}Ru_{31}$	$Co_{62}Ru_{38}$	$Co_{61}Ru_{39}$
C (wt%)	22	34	40

Table 6.3: Composition of the NiRu@C nanostructures synthesized at different pressures as determined by EDX analysis. The relative amount of carbon has been determined by magnetisation studies.

Pressure (bar)	13	21	26	31
Ru (wt%)	7 ± 1	8 ± 1	19 ± 1	16 ± 1
$Ni_{100-x}Ru_x$ (x in wt%)	$Ni_{93}Ru_7$	$Ni_{92}Ru_8$	$Ni_{81}Ru_{19}$	$Ni_{84}Ru_{16}$
C (wt%)	61	73	75	84
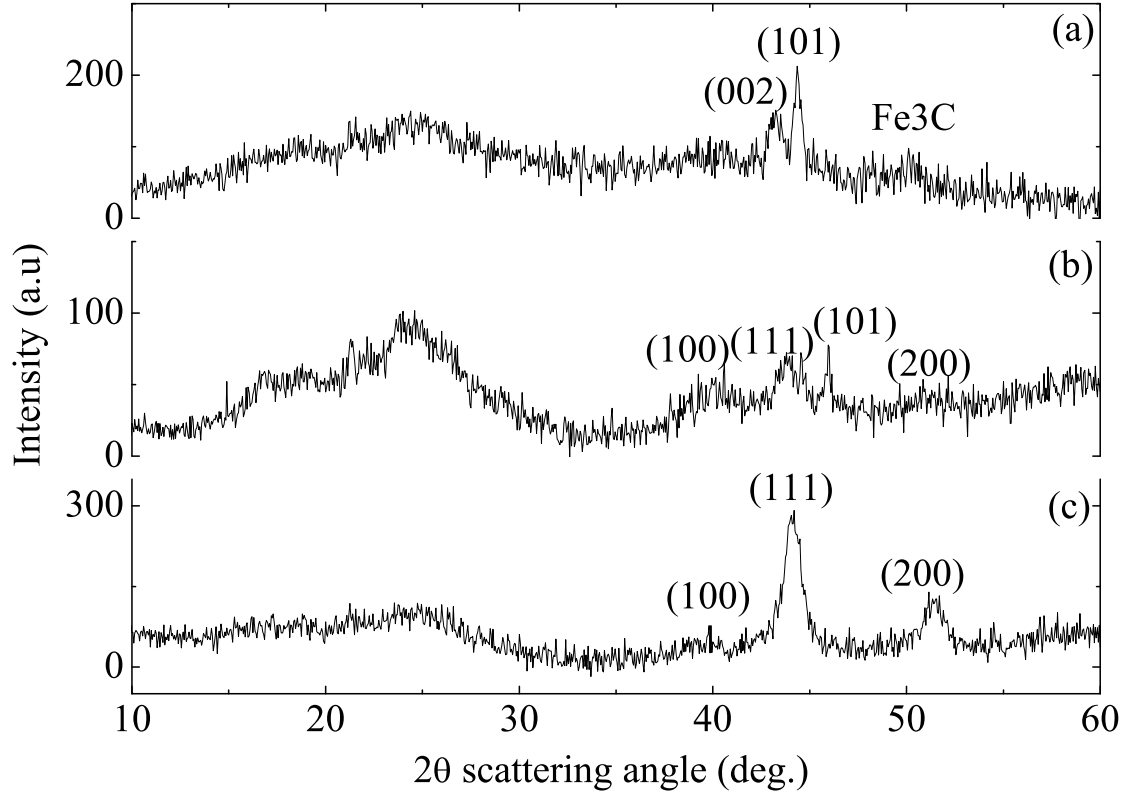
Figure 6.3: X-ray diffraction spectra of (a) FeRu@C , (b) CoRu@C and (c) NiRu@C nanocapsules.

From the TEM studies, the images yield an average size of the FeRu, CoRu, and NiRu core of $< D_{\text{TEM}} > = 13 \pm 5$, 9 ± 3, and 8 ± 3 nm with a relatively large size distribution as displayed in Fig. 6.2(c, f, i). The thickness of the carbon shells amounts to 2-3 nm.

A typical XRD diffraction pattern of the deposited material has been measured for investigation of the phase structures of the alloys as shown in Fig. 6.3. Noteworthy, characteristic peaks of other related compounds especially oxides have not been observed. The results confirm the pure metallic constitution of the nanoalloys except for the case of FeRu, where Fe_3C is formed at $50.1°$. The diffraction peaks at $2\Theta = (43.3°, 44.3°)$, $(40°, 43.7°, 46°, 51°)$, and $(39.8°, 44°, 51.5°)$, are related to the main reflexes (002, 101),(100, 111, 101, 200), and (100, 002, 111) of the FeRu, CoRu,

and NiRu alloy, respectively. The very broad peak at $2\Theta = 26°$ for all samples corresponds to graphitic carbon shells and amorphous-like carbon. As mentioned in the previous chapter the XRD pattern allows to determine the average diameter of the nanoalloys core from the width of the characteristic diffraction peaks. Evaluating the reflexes of FeRu, CoRu, and NiRu (Fig. 6.3) by means of Eq. 4.1 yields an average diameter of 9 ± 2, 6 ± 2, and 6 ± 2 nm respectively, which agrees well with the TEM results. Also, the width of the XRD peaks does not change significantly upon variation of the synthesis pressure, i.e. the mean diameters of the metallic cores do not significantly depend on the pressure. In contrast, the peak positions are slightly shifted which is in agreement with the observed changes in the composition of the nanoalloys.

6.2.2 Magnetic properties

The magnetic properties of the prepared samples have been investigated by studies of the field dependence of the magnetization at room temperature. The field dependencies for the nanoalloys synthesized at various pressure, i.e. the full hysteresis loops of the magnetization, in an external field up to 1T are presented in Fig. 6.4. For FeRu@C, CoRu@C samples, the data reveal a ferromagnetic behaviour at room temperature for all samples prepared at different pressure (open hysteresis loop) Fig. 6.4(a, b). In the case of NiRu@C samples, the data imply a ferromagnetic-like behaviour at room temperature Fig. 6.4(c), i.e. the presence of a remanent magnetization M_{r} and the saturation of the magnetization curve in rather small external magnetic fields at room temperature. The quantitative analysis of the data reveals a clear dependence of the saturation magnetization M_{S} on the synthesis pressure (table 6.4, 6.5, 6.6). In addition, corresponding to the presence of small spontaneous magnetic moments of NiRu@C samples, there are small coercive fields H_{C} close to zero. The other parameters presented in table 6.4, 6.5, 6.6 do not show a significant dependence on pressure.
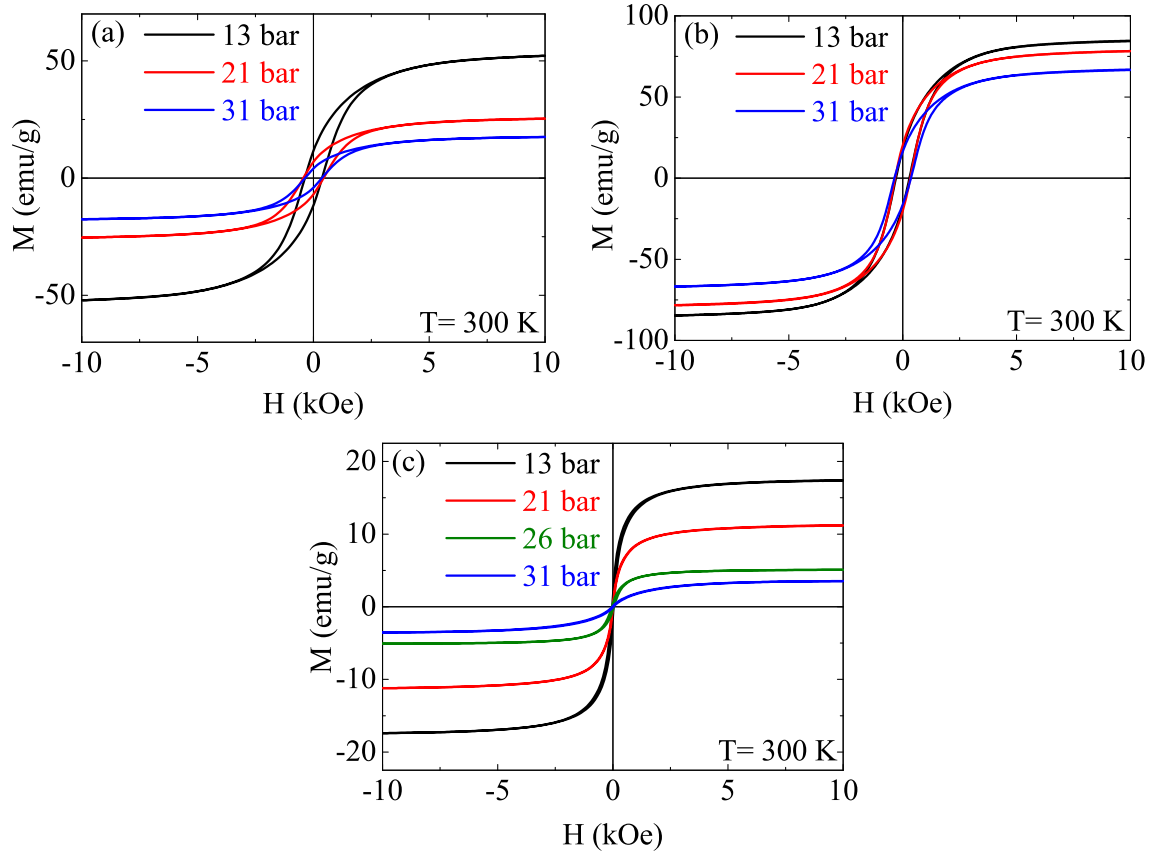
Figure 6.4: Magnetization loops at room temperature of (a) FeRu@C (b) CoRu@C (c) NiRu@C nanoalloys synthesized at different synthesis pressures.

Table 6.4: Magnetic parameters at T = 300 K for FeRu@C synthesised at different pressures.

Pressure	H_C	M_S	M_r	D_{TEM}	D_{XRD}
(bar)	(Oe)	(emu/g)	(emu/g)	(nm)	(nm)
13	373 ± 2	52	12 ± 2	13	9
21	437 ± 2	25	7 ± 2	14	10
26	363 ± 2	18	4 ± 2	13	9

Table 6.5: Magnetic parameters at T = 300 K for CoRu@C synthesised at different pressures.

Pressure (bar)	H_{C} (Oe)	M_{S} (emu/g)	M_r (emu/g)	D_{TEM} (nm)	D_{XRD} (nm)
13	339 ± 2	92	24 ± 2	9	6
21	296 ± 2	85	18 ± 2	8	6
26	362 ± 2	67	16 ± 2	9	6

The magnetization studies provide another alternative to deduce information on the size of the magnetic cores by evaluating the initial slopes of the M-H curves. The major contribution to the initial slope arises from the largest particles. Their larger magnetization vectors are more easily oriented by a magnetic field and thus, an upper boundary for the magnetic size D_{mag} can be estimated by applying Eq. 6.1 [197]. Whereas, the magnetic field dependence of the magnetization at values near the saturation is determined by the fine particles, the orientation of which requires larger fields. This equation is valid only for particles which has coercivity near to zero. So, this equation has been applied for calculation of the particle size of NiRu core.

$$D_{\mathrm{mag}} = \left[\frac{18 k_{\mathrm{B}} T \frac{dM}{dH}}{\pi \rho M_s^2} \right]^{1/3} \tag{6.1}$$

Here, k_{B} is the Boltzmann constant, dM/dH is the initial slope near zero field, and ρ is the bulk density of the sample. The analysis of the experimental data in Fig. 6.4(c) by means of Eq. 6.1 allows to estimate an upper boundary for the magnetic core size (table 6.6). In agreement with the TEM and XRD analysis, the estimated average particle size from the magnetic properties amounts 9 ± 1 nm for all samples of NiRu nanoalloys. The similar core size of all materials is also confirmed by the similar values of the coercive field H_{C}. In contrast, there are strong differences in the

Table 6.6: Magnetic parameters at T = 300 K for NiRu@C synthesised at different pressures D_{mag}, D_{TEM}, D_{XRD} denote the mean core diameters as determined by analysis of magnetization, TEM, and XRD data, respectively.

Pressure	H_{C}	M_{S}	M_{r}	D_{mag}	D_{TEM}	D_{XRD}
(bar)	(Oe)	(emu/g)	(emu/g)	(nm)	(nm)	(nm)
13	30 ± 2	17	1.0 ± 0.1	8	8	6
21	6 ± 2	11	0.2 ± 0.1	9	9	7
26	45 ± 2	5	0.5 ± 0.1	10	9	7
31	26 ± 2	4	0.1 ± 0.1	9	8	6

saturation magnetization values. This value depends both on the relative amount of magnetic core material in the samples and on its composition. Since the composition is known from our EDX analysis, the comparison of the saturation magnetization enables to deduce the nanoalloy to carbon ratio by considering the corresponding values of pure NiRu bulk material [198]. The comparison with the magnetization of the related bulk NiRu allows estimating the mass ratio of the magnetic material in the carbon coated particles (table 6.3), but in the case of FeRu, and CoRu, there was no information in the literatures for the magnetic properties of the related bulk materials regarding to the obtained compositions. In general, the saturation magnetization decreases upon increasing the pressure which is mainly associated with a decreasing relative amount of magnetic materials, i.e. an increase of the relative carbon content. As displayed in table 6.3, the relative amount of carbon sensitively depends on the applied synthesis pressure and it monotonously increases at higher pressure. Note that the actual amount of carbon in the samples implies average interparticle distances of 20-30 nm between the particle centers. This yields only small dipolar interactions in the range of a few K which can be neglected in the analysis of the room temperature magnetization.

From the data in Fig. 6.4(c), the small values of H_C and M_r indicates the existing of smaller particles at different temperature range. It is noted that due to the observed size distribution, the superparamagnetic blocking temperatures are supposed to cover a large temperature range for each sample of the NiRu@C materials. In particular, the smallest particles might exhibit superparamagnetic behavior down to lowest temperatures. However, the blocking temperature depends not only on the particle size but also on the actual magnetic anisotropy of the material. This is underlined by the fact that the mean diameter of the particles as measured by XRD and TEM is very similar for all materials. Hence, in order to study this in more detail, the temperature dependence of the magnetization for all NiRu@C samples has been measured as presented in Fig. 6.5. As explained before, here the samples were firstly cooled down to 5 K in zero magnetic fields and then a magnetic field of 100 Oe was applied to the samples. Under such ZFC conditions the measurements were performed upon heating up to 400 K. In contrast, FC data have been obtained after cooling the sample in the same field.

Fig. 6.5 exhibits a cusp in the ZFC magnetization which might be attributed to the blocking temperature, T_B. However, the ZFC-FC curves depart from each other already at temperatures far beyond the peak in the ZFC curve. On the other hand, the FC magnetization continues to increase without indication of saturation below the peak in the ZFC, which distinguishes the system from the canonical spin-glass systems [199]. The broad size distribution of our nanoparticles already implies a broad distribution of blocking temperatures so that one can attribute the observed ZFC maxima with the average blocking temperature of the mean particles diameter. In general, for superparamagnetic particles, the blocking temperature T_B is linked to particle size and effective anistropy constant via the Néel-Brown equation as explained in the previous chapters [193]. By assuming average blocking temperature at the ZFC maxima associated with the mean diameter as given above, the data yield magneto crystalline anisotropy constants of 0.3-2.6 · 10^5 J/m^3 for the samples pre-
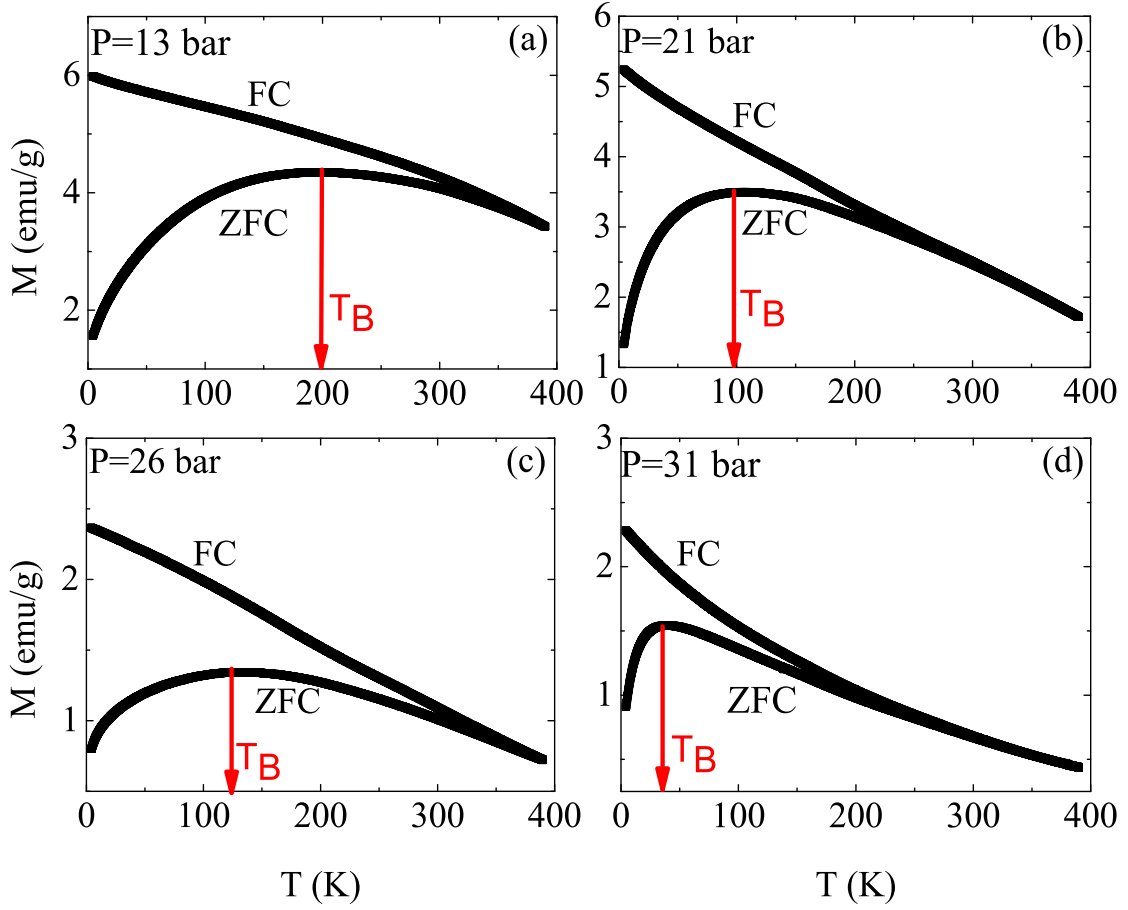
Figure 6.5: Zero-field-cooled (ZFC) and field-cooled (FC) magnetisation curves of NiRu@C nanocapsules at H = 100 Oe, prepared at a pressure of (a) 13 bar , (b) 21 bar, (c) 26 bar and (d) 31 bar, respectively.

sented in Fig. 6.5(a-d). On the other hand, the broad size distribution implies that a considerable amount of particles is ferromagnetic at room temperature in which case the coercivity is given by Eq. 6.2 [200].

$$H_{\mathrm{C}} = \frac{2K_{\mathrm{eff}}}{M_{\mathrm{S}}} \left[1 - \left[\frac{25k_{\mathrm{B}}T}{K_{\mathrm{eff}}V} \right]^{1/2} \right] \qquad (6.2)$$

By knowing the values of H_c, M_{S} and the volume of the magnetic particles, our data yield anisotropy constants of 3.8 - 0.2 · 10^5 J/m^3 for the four samples which is in

the same order of the estimated values by using Néel-Brown formula. Similar high values of compared to the bulk materials have also been observed for other magnetic nanoparticles and are often ascribed to the surface anisotropy effects of the clusters [201].

6.2.3   Heating in AC magnetic fields

In order to test the samples potential for hyperthermia therapy, the feasibility of the highest magnetization NiRu@C nanocapsules for magnetically induced heating has been investigated. In contrast to the measurements presented above, the following experiments have been performed by means of dispersed particles in an aqueous solution. For the sake of preparing the dispersions, the particles were dispersed in a water-albumin solution using a tip sonicator for 2 minuets (10 sec on, and 1 sec off). The concentration of the particles was chosen to be 3 mg/ml. The concentration of albumin in the water was 5 mg/ml. The heating effect of the particles dispersion in AC magnetic fields was studied using applied AC magnetic fields with a frequency of 120 kHz and magnetic field strengths of 0 - 80 kA/m to the highest magnetization sample. The temperature of the sample was detected in dependence of time as shown in Fig. 6.6(a) which presents time-dependent calorimetric measurements at different applied magnetic fields for NiRu@C nanocapsules. A significant heating effect has been observed at applied magnetic fields larger than 20 kA/m. At the maximum applied magnetic field of 80 kA/m, the heating rate reached values of 0.4 °C/min. The specific absorption rate (SAR) has been calculated from the initial slope of the T versus t curves using Eq. 3.7. Fig. 6.6(b) shows the magnetic field dependence of the SAR for NiRu@C. At the maximum applied magnetic field of 80 kA/m, the SAR value of 23 W/g_{NiRu}@C was determined for NiRu@C. The observed quadratic field dependence fits to the fact that the dissipated magnetic energy is proportional to H^2. The relatively broad size distribution in our sample implies both superparamagnetic and ferromagnetic particles at room temperature. So, different heating mechanisms
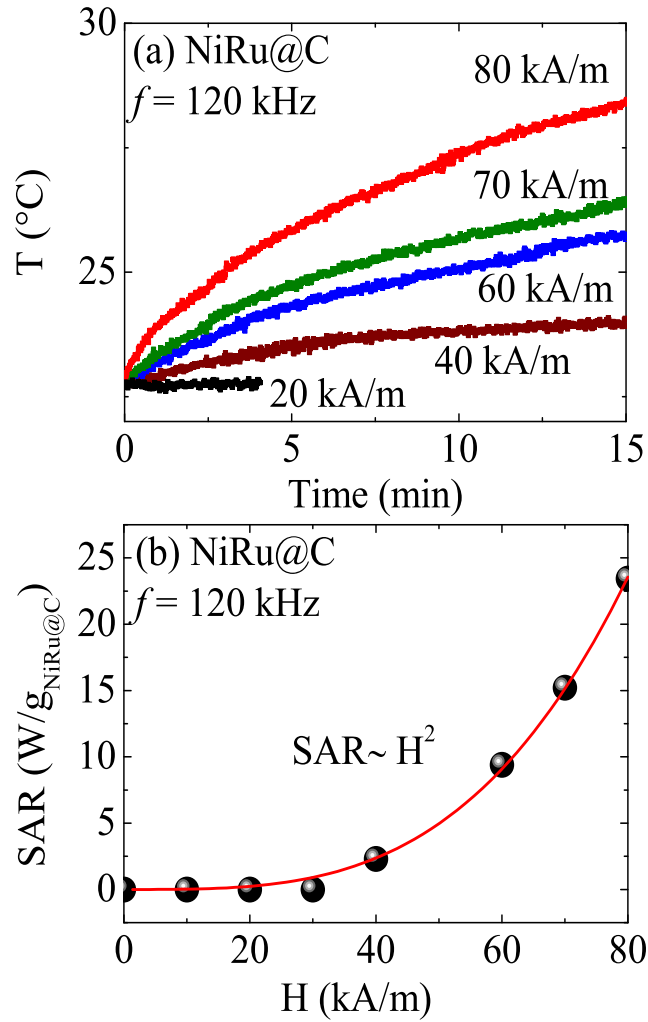
Figure 6.6: (a) Temperature versus time upon application of AC magnetic fields, and (b) corresponding SAR values for the highest magnetization sample of NiRu@C.

can appear from which Néel and Brownian relaxation are expected to be the relevant processes for the observed power absorption [195].

6.3 Conclusions

The synthesis of FeRu@C, CoRu@C, and NiRu@C nanoalloys using the HPCVD technique has been successfully done. The samples have been investigated with respect to their morphology and magnetic properties. Core/shell nanostructures

of FeRu@C, CoRu@C, and NiRu@C have been revealed from the analysis of our HRTEM and XRD data. X-ray diffraction studies reveal FeRu, CoRu, NiRu binary alloys and no oxidized metals. It is to be particularly mentioned that the content of carbon in the deposited nanoalloy material clearly depends on the synthesis pressure while the average sizes of the nanoparticles do not significantly change. Hence, this leads to control the composition of the produced alloys by controlling the pressure during the synthesis process as well as control of the magnetic properties, too. For FeRu@C and CoRu@C samples, the magnetization curves show ferromagnetic behaviour, while NiRu@C samples show ferromagnetic-like behavior for samples prepared at the lowest pressure and typical superparamagnetic behaviour for the sample made at highest pressure. Different values for the saturation magnetization are obtained by variations in the chemical composition of the alloy core but primarily are caused by different carbon contents in the deposited material, especially by more amorphous-like carbon while the thickness of the graphitic shells is relatively constant. On the other hand, the mean superparamagnetic blocking temperatures are mainly associated with the changing of the chemical composition of the core material. A large anisotropy has been noticed from the analysis of (ZFC) magnetization curve of NiRu nanoalloys. The AC heating studies for the dispersed NiRu@C sample displayed induced heat inside the sample solution which yields SAR of 23 $W/g_{NiRu@C}$ at 80 kA/m.

Chapter 7

Carbon coated NiPt and CoPt nanoalloys

When aiming at realizing the promises of applied nanoscience, the production of uniform nanoparticles with controlled particle size is still one of the main challenges. Here, it is demonstrated how carbon-shielded NiPt and CoPt nanoparticles (NiPt@C, CoPt@C) can be progressively synthesized under precise size-control.

7.1 Size-controlled NiPt@C nanoalloys

In this section, the ability of synthesis different sizes of carbon coated NiPt nanoalloys has been achieved by HPCVD technique using different metallorganic precursors of Pt and Ni which can be sublimated in a thermostated sublimation chamber. The particle size of the synthesized NiPt nanoalloys has been controlled by varying the sublimation temperature of the precursors.

7.1.1 Nanoalloys synthesis

HPCVD has been applied for the synthesis of carbon coated NiPt nanoalloys. Here, nickelocene and (trimethyl) methylcyclopentadienyl platinum (IV) precursors have been used as starting materials for the nanoalloying constituents Ni and Pt, respectively. The advantage of using these types of precursors is that they can sublimate at

low temperature range. These allow to have large range of sublimation temperature variation. The metallorganic precursors (weight ratio Ni:Pt = 2:1) have been placed in a particular separated crucible located in a separated thermostated chambers and are sublimated and transported using argon gas (1400 sccm) into the reactor. The temperature and the pressure inside the CVD reactor can be varied in the range of 200-1000 °C and 5-40 bar respectively. Actually, in order to control the synthesis process, three main parameters have to be controlled as mentioned in chapter 4. The first parameter is the temperature inside the CVD reactor which is adjusted and fixed at 900 °C as the optimum temperature for production of the spherical nanoparticles. The second parameter is the change of the pressure inside the CVD reactor which already have been tested for FeRu@C, CoRu@C, and NiRu@C where no observable size variation has been occurred. So, the pressure has been fixed at the optimum value for producing spherical nanoparticles which amounts 13 bar. The last main parameter is the sublimation temperature of the precursors which affects mainly the particle size of the produced NiPt alloy and partially the alloy composition as well as the amount of carbon in the whole material. Here the temperature can be varied for both sublimation chambers in the range of 30-95°C and 95-170°C for Pt and Ni chambers respectively. However, when the temperature of any chamber is fixed and the other is varied, one can get alloys with different compositions as well as different particle sizes.

7.1.2   Result and discussion

7.1.2.1   Morphology and structure

In the vapour-phase synthesis of nanoparticles, the molecules are in the gas phase and under certain conditions, the particles will be formed and the re-evaporation of the particles will be prevented. This is the situation of a supersaturated vapour which has been discussed in chapter 2. After production of the samples, it is expected to

obtain various samples with different particle sizes and physical properties when the sublimation temperature sources be varied. However, the composition, the particle size, and the core/shell morphology of the resulting material were investigated by EDX, and HRTEM as shown in table (7.1, 7.2) and Fig. 7.1. The EDX data (table 7.1, 7.2) imply that moderately increasing the temperature of the sublimation chambers of Ni or Pt yields a higher Ni or Pt content respectively in the produced samples. From these results, It is clear that at low sublimation temperatures the amount of the sublimated particles is small which leads to formation of low Ni or Pt content in the alloys composition as well as the carbon content in the whole sample. In contrast at high sublimation temperature the amount of the sublimated particles is large which leads to the formation of high Ni or Pt content in the alloys composition as well as the carbon content in the whole sample.

Table 7.1: Composition of the NiPt@C nanoparticles synthesized at different sublimation temperatures of Ni ($T_{\mathrm{S}}^{\mathrm{Ni}}$) and constant sublimation of Pt ($T_{\mathrm{S}}^{\mathrm{Pt}}$) at 95 °C determined by EDX analysis. Particle size is evaluated by TEM.

$T_{\mathrm{S}}^{\mathrm{Ni}}$ (°C)	(a,b) 95	(d,e) 110	(j,k) 130
Ni (wt%)	4 ± 1	8 ± 1	17 ± 1
D_{TEM} (nm)	13 ± 5	9 ± 3	2 ± 1
C (wt%)	21	36	90

As shown in the TEM images of Fig. 7.1(a, d, g, j), the formation of different particle sizes has been observed for all samples which prepared at different temperatures of the sublimation chambers. Also examples of particles coated with carbon have been displayed for all samples in Fig. 7.1(b, e, h, k). From the TEM studies, an average size of the NiPt core of 13 ± 5, 9 ± 3, 6 ± 2, and 2 ± 1 nm has been extracted with a relatively small size distribution for the samples prepared at higher
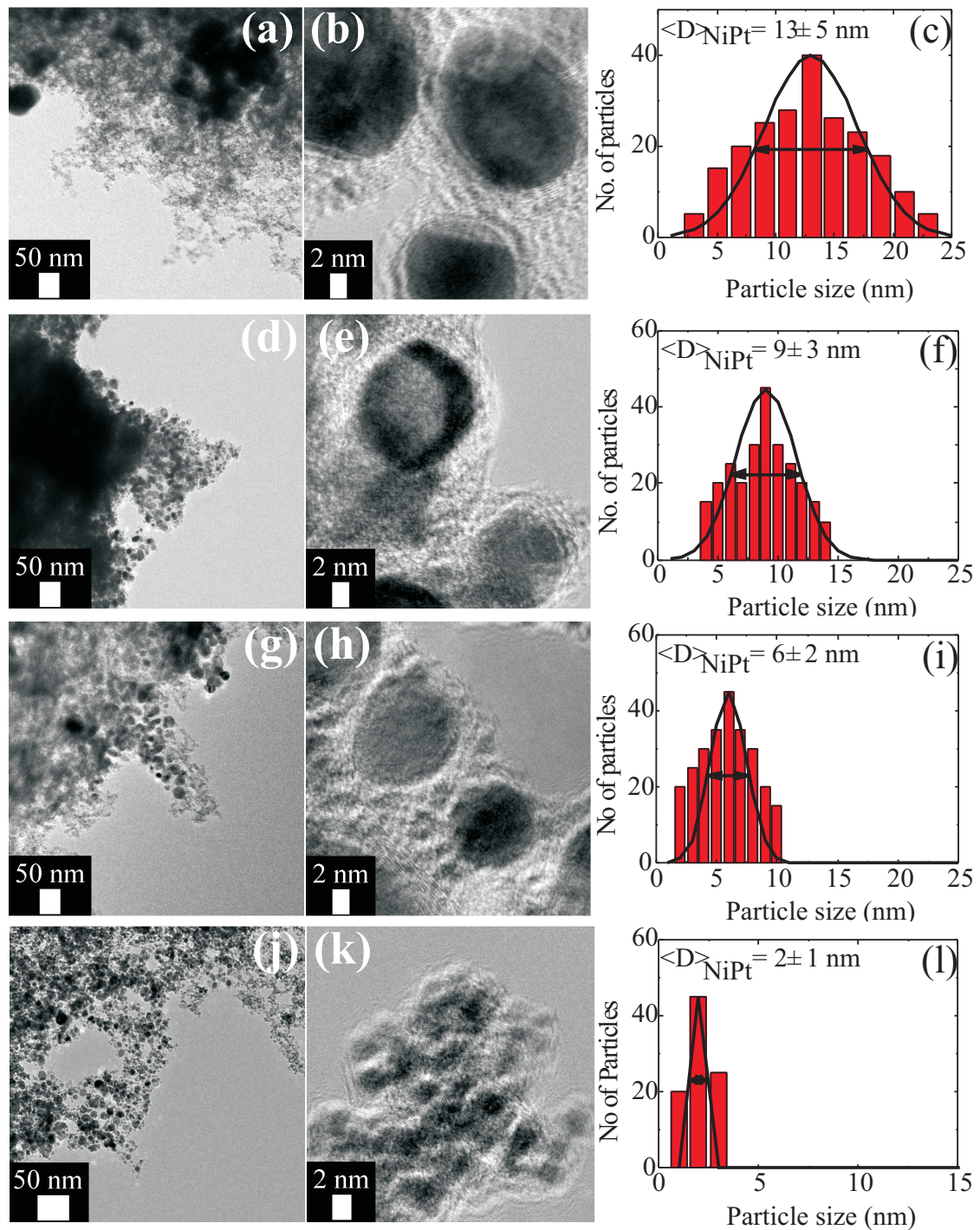
Figure 7.1: TEM images of (a, d, g, j) NiPt coated with carbon shells prepared at different sublimation temperature chamber with different particle size listed in table (5.1, 5.2). (b, e, h, k) Assembly of carbon coated NiPt. (c, f, i, l) Size distribution for each sample.

Table 7.2: Composition of the NiPt@C nanoparticles synthesized at different sublimation temperature of Pt ($T_{\mathrm{S}}^{\mathrm{Pt}}$) and constant sublimation temperature of Ni ($T_{\mathrm{S}}^{\mathrm{Ni}}$) at 130 °C determined by EDX analysis. Particle size is evaluated by TEM. The relative amount of carbon has been determined by magnetization studies.

$T_{\mathrm{S}}^{\mathrm{Pt}}$ (°C)	(g,h) 50	(g,h) 60	(j,k) 95
Pt (wt%)	69 ± 1	73 ± 1	83 ± 1
$\mathrm{D_{TEM}}$ (nm)	6 ± 2	6 ± 2	2 ± 1
C (wt%)	28	57	90

sublimation temperature as shown in Fig. 7.1(c, f, i, l). Note that the thickness of the carbon shells amounts to 1-2 nm. The data in table (7.1, 7.2) and Fig. 7.1 imply the increasing of the particle size when the sublimation temperature of any chamber increases. The resultant smaller particles at higher sublimation temperatures (low supersaturation ratio) confirm the surface growth mechanism. This is resulting in a good crystalline structure and therefore homogeneous nucleation of NiPt@C spherical nanocapsules. While the larger particles which is synthesized at lower sublimation temperatures (high supersaturation ratio) confirm the agglomeration growth mechanism. Hence, a clear dependence of the NiPt particle size as well as of the alloy composition on the sublimation temperature is indeed evident from the obtained data which is shown in Fig 7.2. Here, the inversely linear dependance of the particle size on the sublimation temperature of one chamber where the other chamber is fixed and vice versa has been shown.

In order to explore the structure of the prepared samples, a typical XRD diffraction pattern of the deposited material has been measured as shown in Fig. 7.3. The XRD pattern of the samples prepared at different sublimation temperatures of Pt ($T_{\mathrm{S}}^{\mathrm{Pt}}$) at fixed sublimation temperatures of Ni ($T_{\mathrm{S}}^{\mathrm{Ni}}$)= 130 °C are shown in Fig.
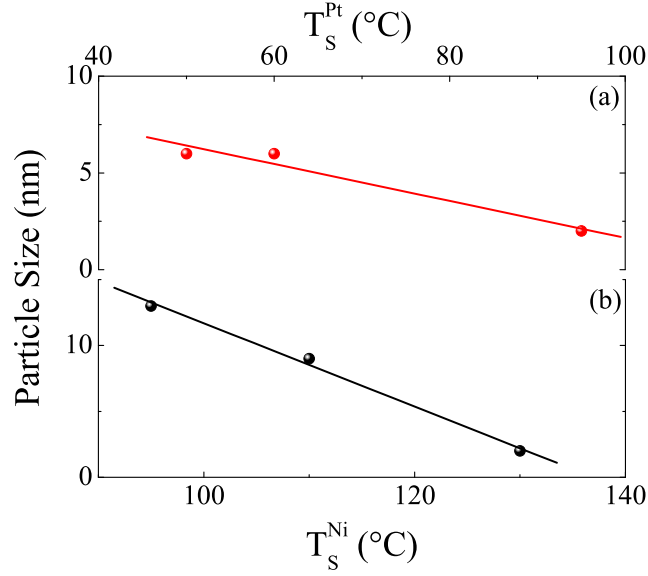
Figure 7.2: Particle size dependence on sublimation temperatures of (a) Pt at $T_S^{Ni} = 130$ °C and (b) Ni at $T_S^{Pt} = 95$ °C of NiPt@C nanostructures.

7.3(a, b) and at different (T_S^{Ni}) at constant (T_S^{Pt})= 95 °C as shown in Fig. 7.3(c). The results confirm the elementarily pure constitution of the nanoalloy core. The diffraction peaks at $2\Theta = 40°$, $46°$, $68°$ and $82°$ are related to the main reflexes (111), (200), (220) and (311) in which NiPt alloy crystallize in bulk. From the width of the characteristic diffraction peaks, evaluating the four main reflexes of NiPt by means of Scherrer equation yield an average diameter of 7 ± 4, 7 ± 4 and 3 ± 1 nm for samples prepared at different (T_S^{Pt}) and constant (T_S^{Ni})= 130 °C as shown in Fig. 7.3(a, b) and 15 ± 7, 10 ± 5, and 3 ± 1 nm for samples prepared at different (T_S^{Ni}) and constant (T_S^{Pt})= 95 °C as seen in Fig. 7.3(c). These results are in good agreement with the TEM results. In contrast, the peak positions are slightly shifted which is in agreement with the observed changes in the composition of the nanoalloys.
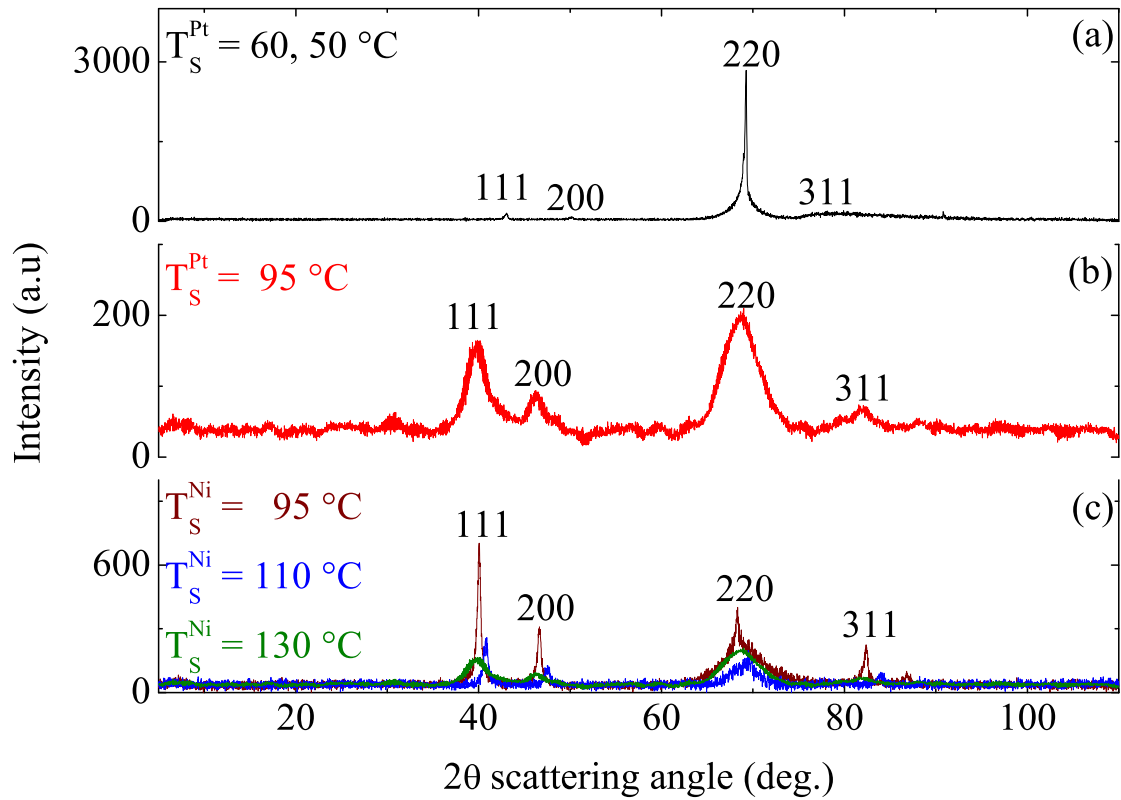
Figure 7.3: X-ray diffraction spectrum of NiPt@C nanostructures for samples prepared at different sublimation temperatures of (a, b) Pt at $T_S^{Ni} = 130\,°C$ and (c) Ni at $T_S^{Pt} = 95\,°C$.

7.1.2.2 Magnetic properties

The magnetic properties of NiPt@C have been studied by means of studies of the field dependence of the magnetization at room temperature and of the temperature dependence at a constant field of $H = 100$ Oe. The field dependencies for the nanoalloys synthesized at different sublimation temperature, i.e. the full hysteresis loops of the magnetization, in an external field up to 1 T are presented in Fig. 7.4.

The figure shows ferromagnetic-like behaviour at room temperature for all samples prepared at different sublimation temperatures, i.e. the presence of a remanent magnetization M_r and coercivity H_C in rather small external magnetic fields at room
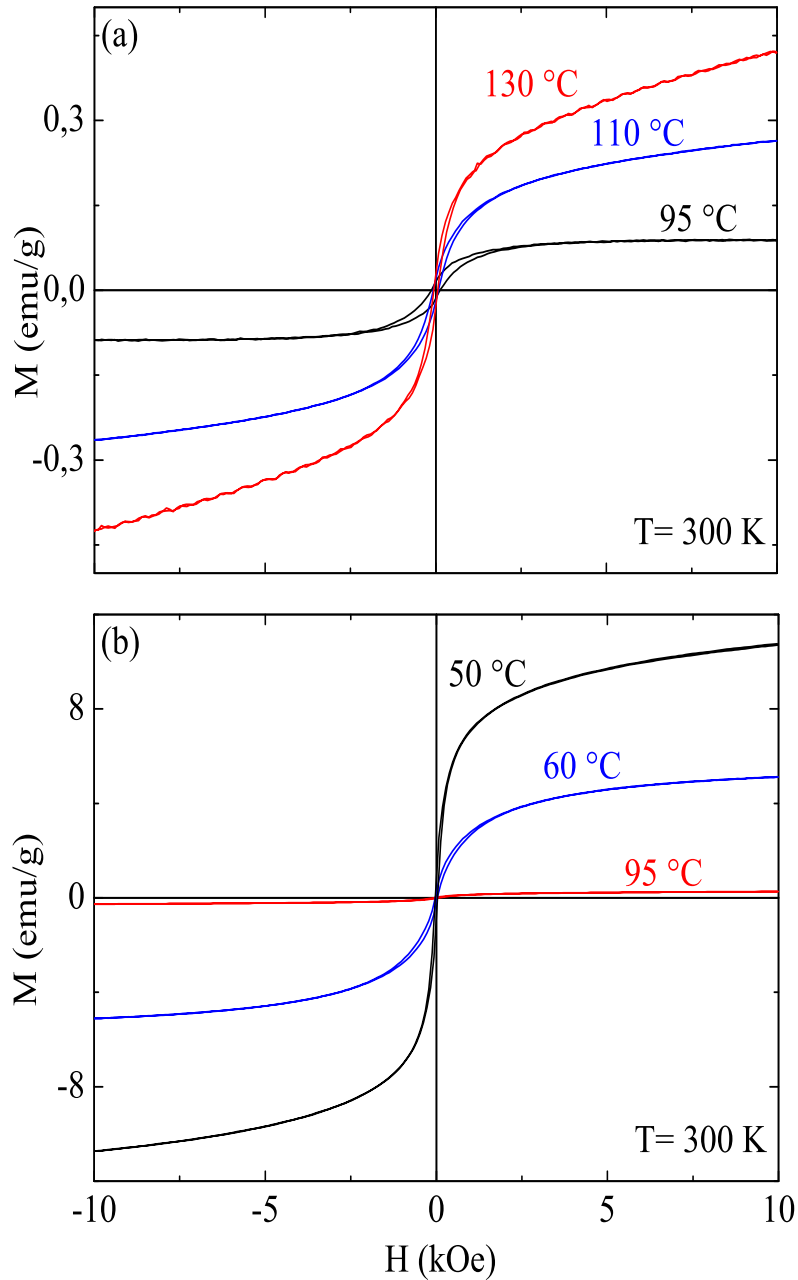
Figure 7.4: Magnetization loops at room temperature of NiPt@C nanoalloys synthesized at different sublimation temperatures of (a) Ni at $T_\mathrm{S}^\mathrm{Pt} = 95$ °C, and (b) Pt at $T_\mathrm{S}^\mathrm{Ni} = 130$ °C.

temperature. The quantitative analysis of the data reveals a clear dependence of the magnetization on the sublimation temperature (table 7.3, 7.4). It is clear from Fig. 7.4 (a, b) that the magnetization decreases with increasing the Pt-content and increases with increasing the Ni-content of the alloy. Corresponding to the presence of a small M_r, there are small coercive fields H_C close to zero indicates the existence of small particle size of the magnetic cores which confirms the results from TEM and XRD. All the magnetic parameters have been listed in table (7.3, 7.4).

Table 7.3: Magnetic parameters at $T = 300$ K for NiPt@C synthesized at different T_S^{Ni} and at constant $T_S^{Pt} = 95$ °C.

T_S^{Ni}	H_C (Oe)	$M(1$ T$)$	M_r	D_{TEM}	D_{XRD}
(°C)	(Oe)	(emu/g)	(emu/g)	(nm)	(nm)
95	126 ± 2	0.09	0.02	13 ± 5	15 ± 7
110	75 ± 2	0.26	0.02	9 ± 3	10 ± 5
130	58 ± 2	0.42	0.03	2 ± 1	3 ± 1

Table 7.4: Magnetic parameters at $T = 300$ K for NiPt@C synthesised at different T_S^{Pt} and at constant $T_S^{Ni} = 130$ °C.

T_S^{Pt}	H_C (Oe)	$M(1$ T$)$	M_r	D_{TEM}	D_{XRD}
(°C)	(Oe)	(emu/g)	(emu/g)	(nm)	(nm)
50	32 ± 2	11	0.8	6 ± 2	7 ± 4
60	31 ± 2	5	0.2	6 ± 2	7 ± 4
95	58 ± 2	0.42	0.03	2 ± 1	3 ± 1

The formation of different core sizes for all samples is confirmed by the observed different values of the coercive field H_C. Also, there are differences in the magnetization values $M(1$ T$)$, which depends both on the relative amount of magnetic
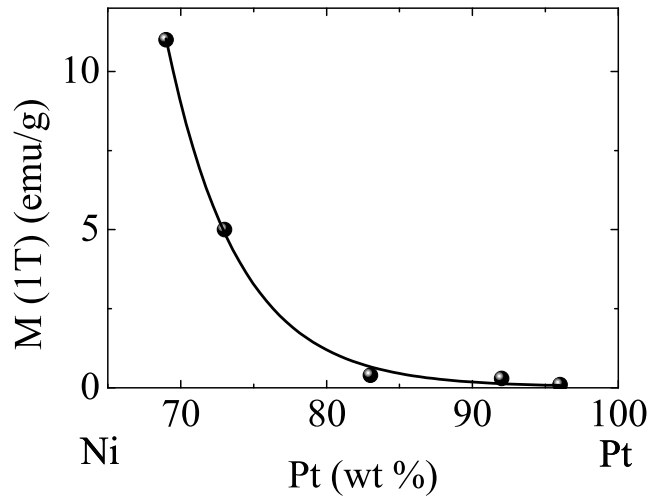
Figure 7.5: Magnetization of NiPt@C independence on the Pt content.

core material in the samples and on its composition. Fig. 7.5 shows an decreasing in the magnetization value according to the increasing of the Pt content inside the alloy which fits to an exponential dependance of the magnetization on Pt content is increasing. So, the comparison of the magnetization values to the corresponding values of pure NiPt bulk material with the same Ni:Pt ratio [198] enables to deduce the nanoalloy to carbon ratio. As displayed in table 7.2, the relative amount of carbon sensitively depends on the sublimation temperature and it monotonously increases at higher sublimation temperatures. Note that the actual amount of carbon in the samples implies average interparticle distances of 8-20 nm between the particle centers. At these distances, only small dipolar interactions in the range of a few K are expected which can be neglected in our analysis of the room temperature magnetization.

The magnetization data imply small values of H_C and TEM data show narrow size distribution of the particles which indicate the existence of superparamagnetic particles. This already announces that the superparamagnetic blocking temperature (T_B) is smaller than 300 K for most of the samples. In contrast, for some samples large finite H_C was found at room temperature which may exhibit a blocking temperature

$T_\mathrm{B} > 300$ K especially for the sample which showed broad size distribution. Hence, due to the observed size distribution from TEM analysis for all samples prepared at different sublimation temperatures, the superparamagnetic blocking temperatures are supposed to cover a large temperature range for the material prepared at lower sublimation temperatures. The smallest particles might exhibit superparamagnetic behavior down to lowest temperatures for the material prepared at higher sublimation temperatures and shows narrow size distribution.

In order to investigate T_B, the temperature dependence of the magnetization has been measured as shown in Fig. 7.6. For these measurements, the samples were firstly cooled down to 5 K in zero magnetic fields and then a magnetic field of 100 Oe was applied to the samples. Fig. 7.6 exhibits a cusp in the zero-field cooled (ZFC) magnetization which might be attributed to the blocking temperature T_B. However, the ZFC-FC curves depart from each other already at temperatures far beyond the peak in the ZFC curve. On the other hand, the FC magnetization continues to increase without indication of saturation below the peak in the ZFC, which distinguishes the system from the spin-glass systems [199]. However, the separation of ZFC and FC branches of magnetization curves on decreasing the temperature is a characteristic feature of an agglomeration of superparamenetic particles. The broad size distribution for some of our samples already implies a broad distribution of blocking temperatures such as for the sample which was prepared at T_S^Ni, T_S^Pt = 95, 95 °C (Fig. 7.6(a)). One might conclude that the observed ZFC maxima are attributed to the average blocking temperature of the particles with the mean diameter. The maxima of the ZFC curve at Fig. 7.6(a) indicates the blocking temperatures T_B of 395, 45, 10 K for samples prepared at T_S^Ni, T_S^Pt = (95, 95), (110, 95), and (130, 95) °C, respectively. The ZFC maxima at Fig. 7.6(b) imply that T_B amounts to 10, 25, and 215 K for samples prepared at T_S^Ni, T_S^Pt = (130, 95), (130, 60), and (130, 50) °C respectively. Therefore, the blocking temperature dependance on the sublimation temperature is clear as shown in Fig. 7.7. Here the data show that T_B
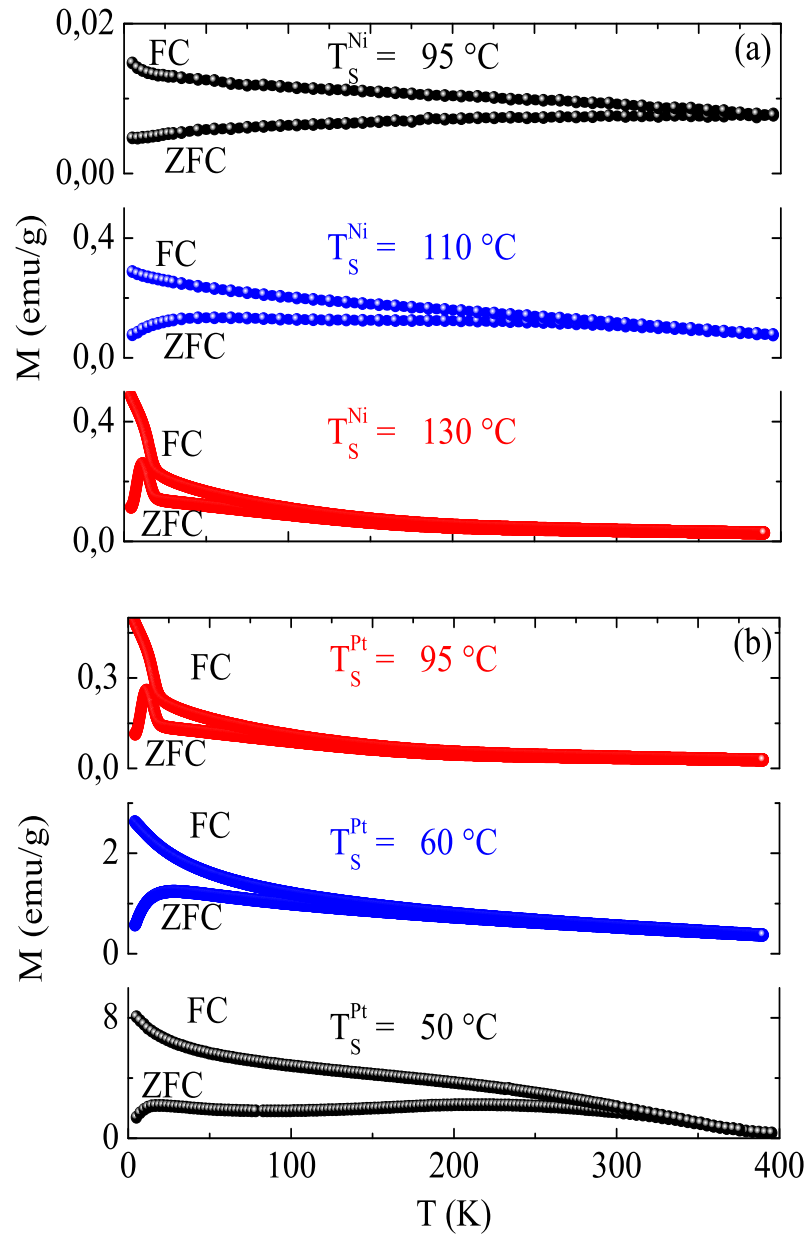
Figure 7.6: Zero-field-cooled (ZFC) and field-cooled (FC) magnetisation curves of NiPt@C nanocapsules at $H = 100$ Oe, prepared at different sublimation temperature of (a) Ni at $T_S^{Pt} = 95$ °C, and (b) Pt at $T_S^{Ni} = 130$ °C.
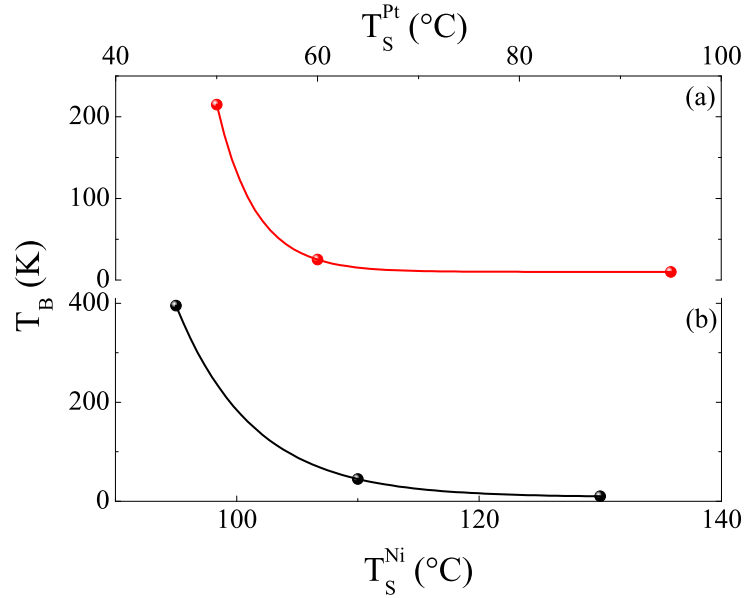
Figure 7.7:   Blocking temperature dependence on sublimation temperature of NiPt@C nanocapsules prepared at at different sublimation temperature of (a) Pt at $T_S^{Ni} = 130$ °C and (b) Ni at $T_S^{Pt} = 95$ °C.

decreases exponentially according to the increasing of the sublimation temperature of one chamber where the other chamber is fixed (Fig. 7.7).

As known from the Ref. [202], the obtained particle sizes are still linked to T_B via the Neel-Brown equation $T_B = KV/25k_B$ [193]. Then, by assuming a mean blocking temperature at the ZFC maxima associated with the mean diameter as given above, the data yield magneto-crystalline anisotropy constants K of 0.3-4 $\cdot$ 10^5 J/m^3 for all samples presented in Fig. 7.6(a, b). These large values of the magnetocrystaline anisotropy is useful to keep the magnetic energy barriers (KV) sufficiently high which motivate the potential of NiPt@C nanocapsules for the recording media applications.

7.2 Size-controlled CoPt@C nanoalloys

In this section the synthesis of different CoPt@C particle sizes, alloy compositions, and carbon to metal ratio by varying the temperature of the sublimation chamber of Co are studied.

7.2.1 Nanoalloys synthesis

The synthesis of carbon coated CoPt nanoalloys has been performed using the same HPCVD technique which is used for synthesis of NiPt@C samples. During the synthesis of CoPt@C samples, the temperature and the pressure inside the CVD reactor have been fixed at 900 °C and 13 bar respectively. These conditions was the optimum for production of spherical particles coated with carbon. The two different metallorganic precursors of copaltocene for Co and trimethylmethylcyclopentadienyl platinum (IV) for Pt have been located in a separated thermostated chambers (weight ratio Co:Pt = 2:1) and are sublimated and transported using argon gas (1400 sccm) into the CVD reactor. The temperatures of the sublimation chambers have been varied in the range of 95-170°C for Co chamber, while is fixed at 95 °C for Pt chamber. Here only the sublimation temperature of the Co chamber is varied in order to increase the Co content inside the alloy, therefore one can get samples with higher magnetic properties. In addition, in order to synthesis Co rich content in the CoPt alloy, the temperature of the sublimation chambers for Co and Pt have been adjusted at 170 °C, 60 °C respectively. It is expected that the change of the temperatures of the sublimation chambers will lead to production of various samples with different particle sizes, alloy compositions, and carbon to metal ratio as well as characteristic magnetic properties.

7.2.2   Result and discussion

7.2.2.1   Morphology and structure

The synthesis of different particle sizes for CoPt@C has been done based on the principle of the particle surface growth in the gas phase which has been discussed in details in chapter 2 and in the previous section. It is also clear here that at higher sublimation temperature one can get smaller particles (surface growth mechanism), and larger particles at lower sublimation temperature (agglomeration mechanism). However, the alloy composition, the particle size, and the core/shell morphology of the synthesized material have been investigated using EDX and HRTEM as shown in table 7.5 and Fig. 7.8. The EDX data give information regarding the alloy composition for all the prepared samples. According to the increase of the sublimation temperature of Co T_S^{Co}, the amount of the sublimated particles increase. Therefore, the Co content inside the alloy increases as well as the carbon content in the whole sample.

Table 7.5: Composition of the CoPt@C nanoparticles synthesized at different T_S^{Co} and at constant $T_S^{Pt}= 95$ °C determined by EDX analysis. Particle size is evaluated by TEM.

T_S^{Co} (°C)	(a,b) 95	(d,e) 110	(g,h) 130	(j,k) 150	(m,n) 170
Co (wt%)	5 ± 1	7 ± 1	11 ± 1	13 ± 1	15 ± 1
D_{TEM} (nm)	18 ± 6	14 ± 5	6 ± 1.5	2 ± 1	2 ± 0.5
C (wt%)	15	20	22	37	42

The formation of spherical CoPt@C nanocapsules with different particle sizes have been observed from TEM images and are listed in table 7.5 for all prepared
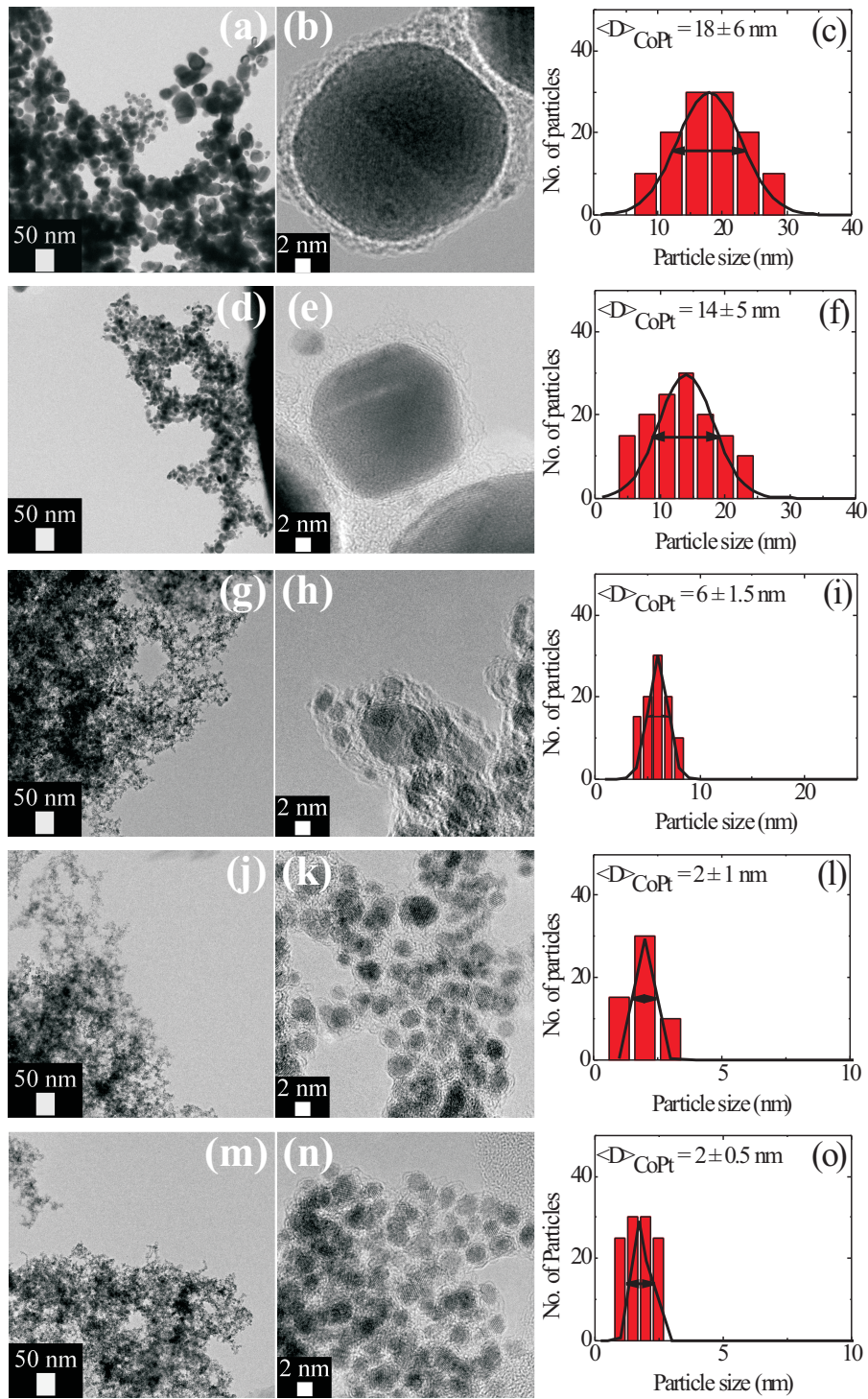
Figure 7.8: TEM images of (a, d, g, j, m) CoPt@C prepared at different T_S^{Co} and at constant $T_S^{Pt} = 95$ °C. (b, e, h, k, n) Assembly of carbon coated CoPt. (c, f, i, l, o) Size distribution for each sample.
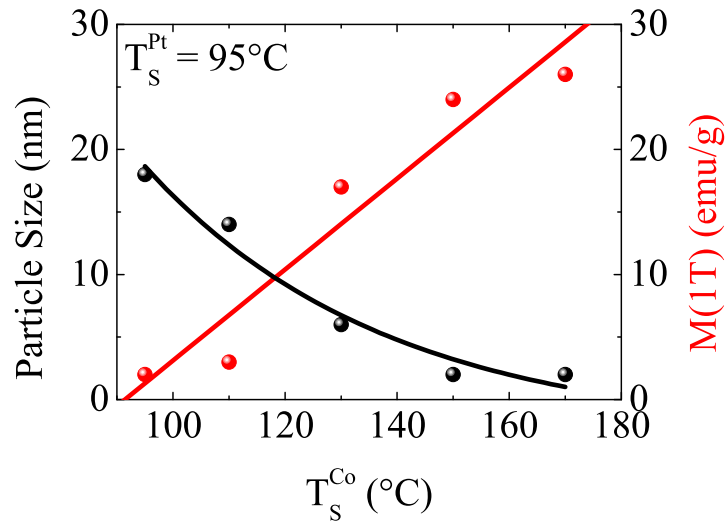
Figure 7.9: Particle size and magnetization dependence of T_S^{Co} at $T_S^{Pt} = 95$ °C.

samples at different sublimation temperatures of Co at fixed $T_S^{Pt} = 95$ °C as shown in Fig. 7.8(a, d, g, j, m). In order to display the core/shell structure, an examples of CoPt alloys coated with carbon for all samples have been presented in Fig. 7.8(b, e, h, k, n). The TEM studies revealed an average size of the CoPt core of 18 ± 6, 14 ± 5, 6 ± 1.5, 2 ± 1 and 2 ± 0.5 nm with narrow size distribution for the samples prepared at higher sublimation temperature as shown in Fig. 7.8(c, f, i, l, o) respectively. The thickness of the carbon shells has been determined to be 1-2 nm. So, it is clear from the TEM images that the particle size depends on T_S^{Co} at fixed $T_S^{Pt} = 95$ °C (Fig. 7.9). Fig. 7.9 shows that the particle size decreases exponentially versus the increasing of the sublimation temperature of the Co. In addition, the figure shows the magnetization dependance on the sublimation temperature which will be discussed in the next subsection.

In order to get higher content of Co in the alloy system, another composition has been synthesized at lower sublimation temperature of Pt (60 °C), and at higher sublimation temperature of Co (170 °C). The Co composition has been analyzed using EDX to be 40 wt% and the carbon contents amounts 18 wt%. The core/shell
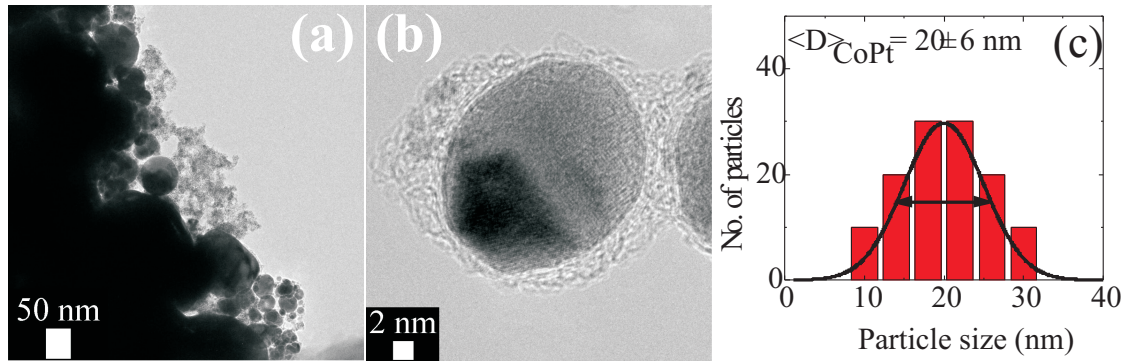
Figure 7.10: TEM images of (a) CoPt coated with carbon shells prepared at $T_S^{Co} = 170\,°C$, and $T_S^{Pt} = 60\,°C$ (b) Assembly of carbon coated CoPt. (c) Size distribution of the prepared sample.

structure, the particle size distribution have been investigated by TEM and the average core size was found to be 20 ± 6 nm as shown in Fig. 7.10(a-c).

After investigation of the morphology of the samples, the structure has been explored. Typical XRD diffraction patterns of the deposited materials are shown in Fig. 7.11. The results confirm the elementarily pure constitution of the nanoalloys cores. The diffraction peaks at $2\theta = 33°, 41°, 48°, 61°, 69°$, and $82°$ are related to the main reflections (100), (111), (200), (210), (220) and (311) of the CoPt alloy. The average diameter of the nanoparticles as determined by using Scherrer equation amount to 18 ± 10, 17 ± 10, 9 ± 4, 6 ± 3, 4 ± 2 and 19 ± 10 nm for all the samples from (a) to (f), respectively. These values confirm the obtained values from TEM images. Note that the peak positions are slightly shifted due to the changes in the composition of the nanoalloys.
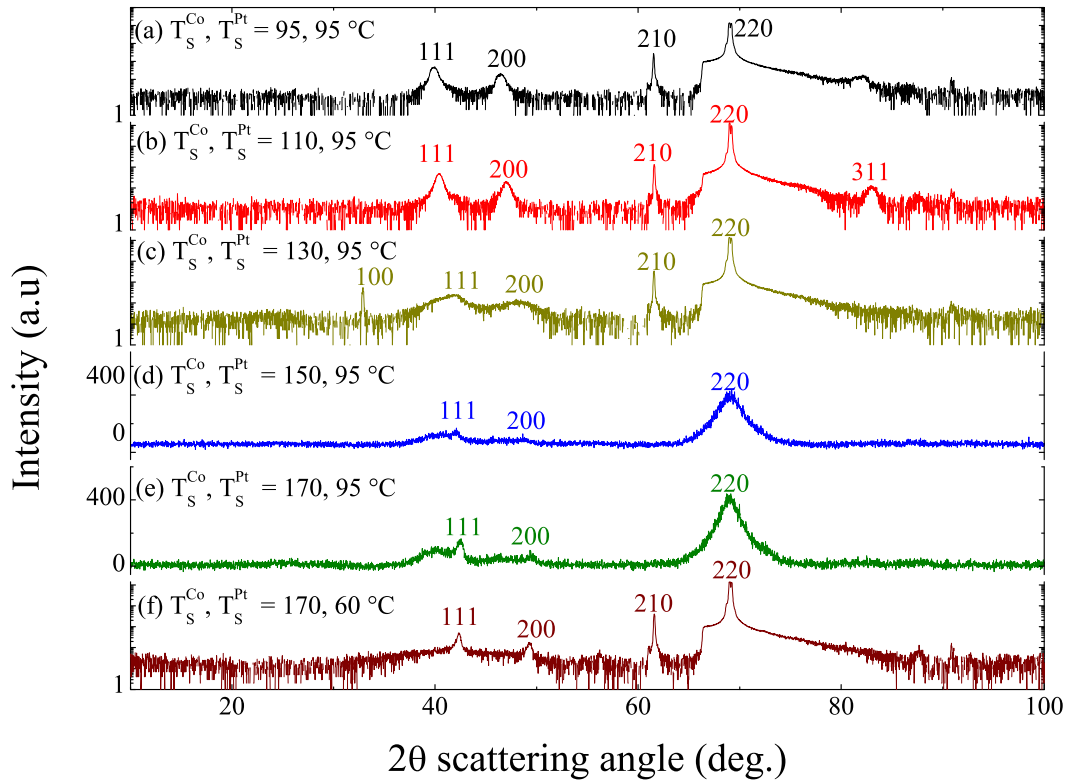
Figure 7.11: X-ray diffraction specta of CoPt@C nanostructures for samples prepared at different sublimation temperatures of Co, and Pt ($T_{\mathrm{S}}^{\mathrm{Co}}$, $T_{\mathrm{S}}^{\mathrm{Pt}}$).

7.2.2.2 Magnetic properties

In order to investigate the magnetic properties of the synthesized CoPt nanoalloys, the field dependence of the magnetization at room temperature has been measured in external fields up to 1 T (Fig. 7.12). Here Fig. 7.12 shows open hysteresis curves so that already from a first glance it can be concluded that samples exhibit ferromagnetic-like response at room temperature.

The result shows a clear dependence of the magnetization on the sublimation temperature and on the platinum content inside the alloy (Fig. 7.9, 7.13, table 7.6).
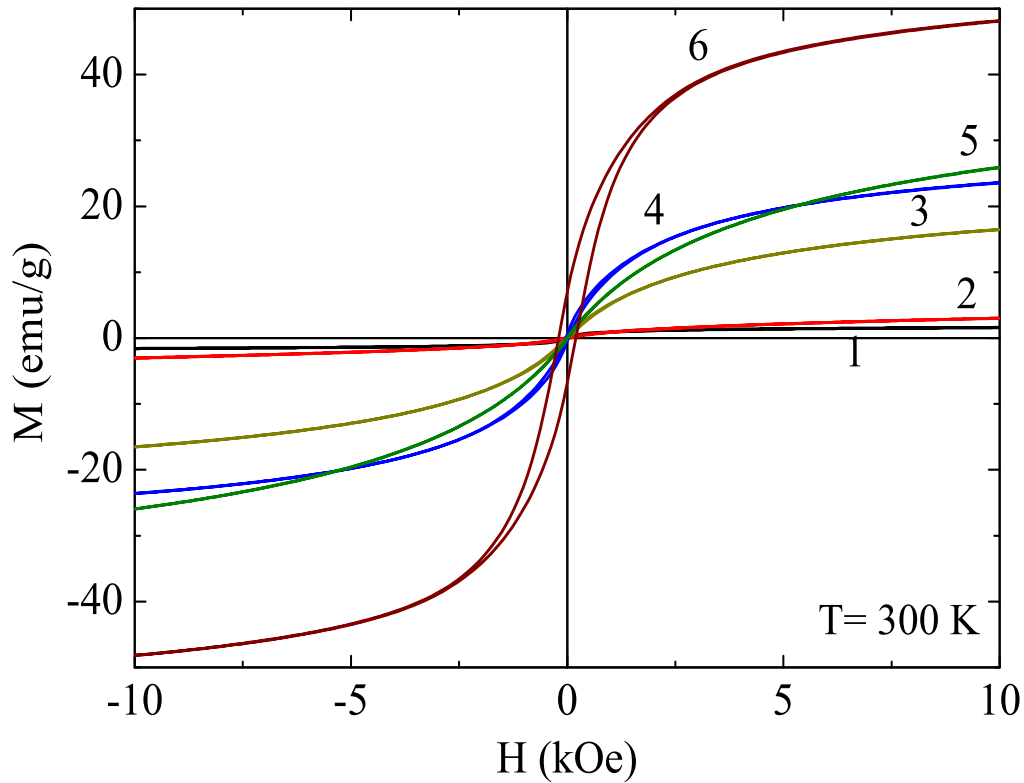
Figure 7.12: Magnetization loops at room temperature of CoPt@C nanoalloys synthesized at (1-5) different T_S^{Co} at fixed $T_S^{Pt} = 95$ °C and at (6)$T_S^{Pt} = 60$ °C and $T_S^{Co} = 170$ °C.

Fig. 7.9 shows linear dependence of $M(1 \text{ T})$ on T_S^{Co} which can be expected from the increase of the Co content inside the alloy due to the increasing of the T_S^{Co} which leads to an increase in the magnetization of the alloy under applied external magnetic field. In contrast the situation when the Pt content increases inside the alloy, the magnetization of the alloys decreases under applied external magnetic field as shown in Fig. 7.13. Corresponding to the presence of a small remnant magnetization M_r, there are small coercive fields H_C which are close to zero. The different core sizes of all materials which are observed in TEM are confirmed by the different values of the coercive field H_C. Also, the magnetization depends both on the relative amount of magnetic core material and on its composition. Note that interparticle interaction

Table 7.6: Magnetic parameters at $T = 300$ K for CoPt@C synthesized at different $T_{\mathrm{S}}^{\mathrm{Co}}$ and $T_{\mathrm{S}}^{\mathrm{Pt}}$.

$T_{\mathrm{S}}^{\mathrm{Co}}, T_{\mathrm{S}}^{\mathrm{Pt}}$	H_{C} (Oe)	$M(1$ T$)$	M_{r}	D_{TEM}	D_{XRD}
(°C)	(Oe)	(emu/g)	(emu/g)	(nm)	(nm)
(1) 95, 95	51 ± 2	2	0.1	18 ± 6	18 ± 12
(2) 110, 95	51 ± 2	3	0.1	14 ± 5	17 ± 10
(3) 130, 95	27 ± 2	17	0.2	6 ± 1.5	9 ± 4
(4) 150, 95	31 ± 2	24	0.5	2 ± 1	6 ± 3
(5) 170, 95	14 ± 2	26	0.1	2 ± 0.5	4 ± 2
(6) 170, 60	199 ± 2	46	7	20 ± 6	19 ± 10

can be neglected in the data interpretation due to rather larger interparticle distances of 12-20 nm.

From the obtained data in table 7.6, the small values of H_{C}, M_{r} and the narrow size distribution of the particles one can already expect the existence of superparamagnetic behavior at lower temperature range. This is in deep confirmed by the magnetization data shown in Fig. 7.14. Here, the temperature dependence of the magnetization at constant magnetic fields of 50, 100, or 150 Oe is presented. The figure includes two types of measurements are carried out namely zero-field cooling (ZFC) and field cooling (FC). The FC procedure differs from ZFC only by the fact that the sample is cooled in a nonzero magnetic field. For magnetic nanoparticles, the FC (T) and ZFC (T) curves usually coincide at relatively high temperatures but start to differ below a certain temperature.

As seen in Fig. 7.14, there is a peak in ZFC-magnetization which usually is related to the average blocking temperature T_{B}. At temperature beyond T_{B} the ZFC-FC depart from each other. This separation of the ZFC and FC curves is
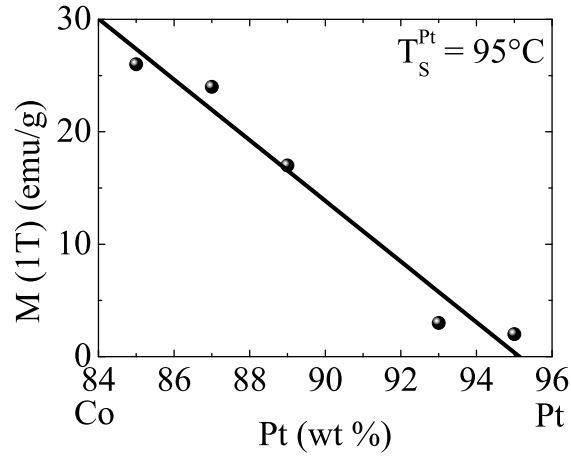
Figure 7.13: Magnetization of CoPt@C independence on the Pt content.

an indication for an agglomeration of the superparamagnetic particles. Here Fig. 7.14(a, b, f) display a broad ZFC curve which is a characteristic feature for broad distribution of T_B. This is usually due to the broad size distribution of the particular synthesized particles at lower sublimation temperature. In contrast Fig. 7.14(c, d, e) exhibit the relative narrow ZFC curve which is characteristic feature for the narrow distribution of T_B. This is according to the narrow size distribution of the particular synthesized particles at higher sublimation temperatures. Hence from Fig. 7.14 one can attribute the observed ZFC maxima as the average blocking temperature of the particles according to the mean particle size. So that the average blocking temperature T_B amounts to 231, 50, 37, 11, 8, and 82 K for the samples shown in Fig. 7.14(a-f) respectively. However, one can conclude the dependence of T_B on the synthesis sublimation temperature as well as the particle size as shown in Fig 7.15. Here the blocking temperature shows an exponential decay versus the synthesis sublimation temperature which confirms the same behaviour in the case of NiPt@C samples. Since, the blocking temperature depends not only on the particle size but also on the actual magnetic anisotropy of the material, one can use the Neel-Brown equation for estimation of the magneto crystalline anisotropy constant. By assuming a mean blocking temperature with the mean diameter as mentioned above, the data
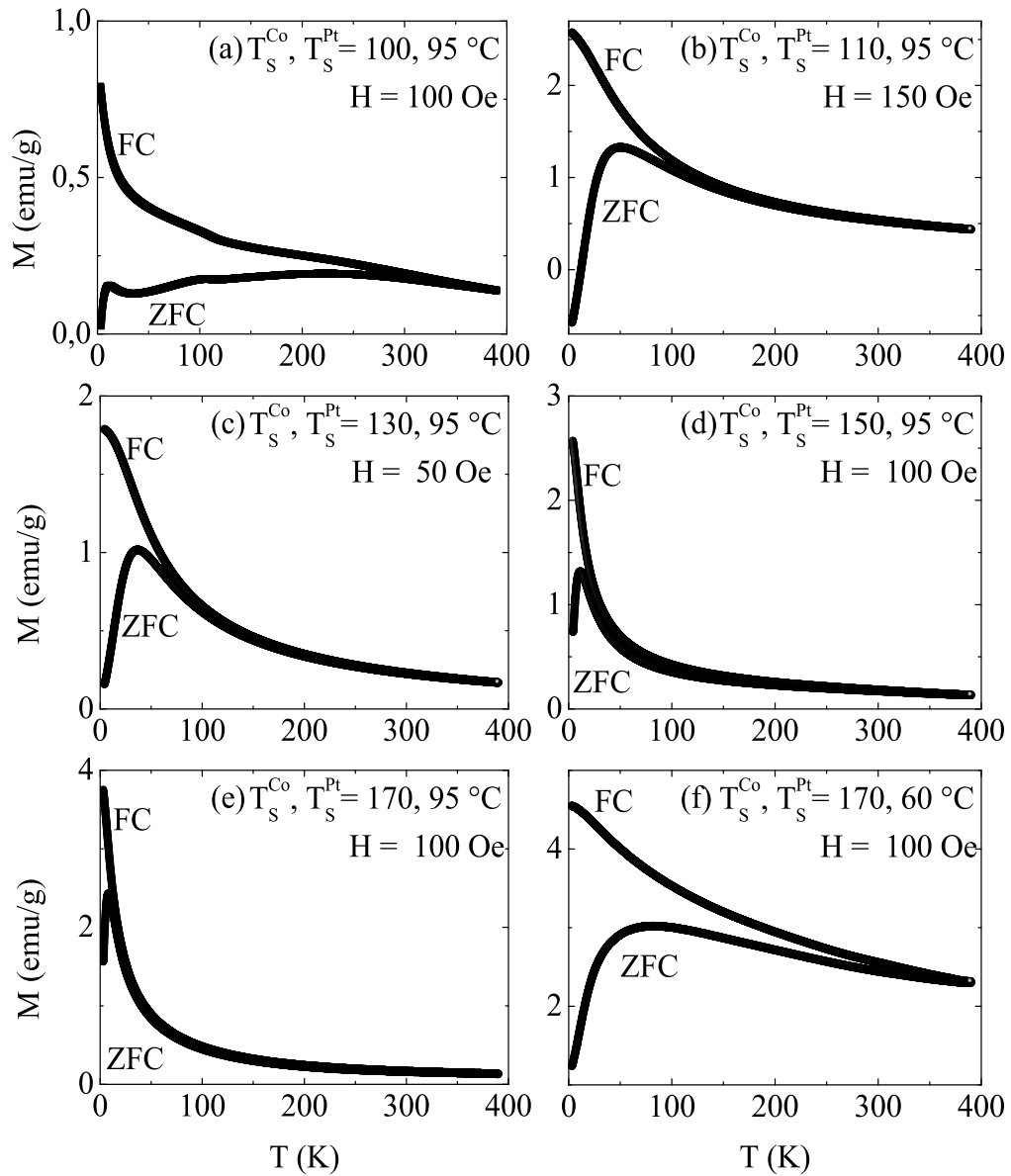
Figure 7.14: Zero-field-cooled (ZFC) and field-cooled (FC) magnetization curves of (a-f)CoPt@C nanocapsules prepared at different T_S^{Co}, T_S^{Pt}.
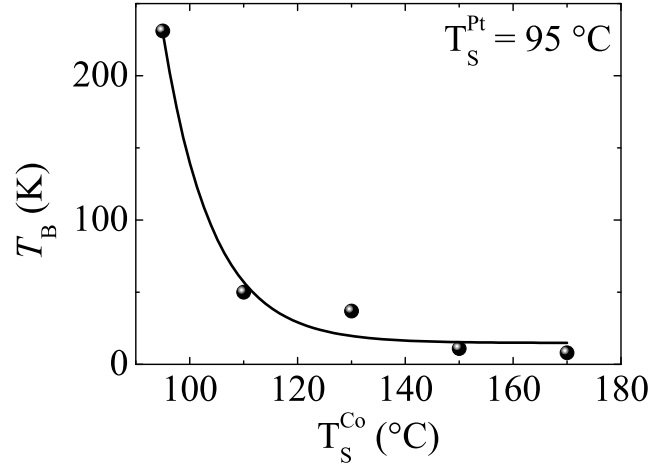
Figure 7.15: Blocking temperature dependence on sublimation temperature of CoPt@C nanocapsules prepared at different sublimation temperature of Co at T_S^{Pt} = 95 °C.

yield anisotropy constants of 0.2-6.7 $\cdot 10^5$ J/m^3 for all samples presented in Fig. 7.14(a-f). These values is large which open the potential of the synthesized particles for recording media application.

7.2.2.3 Heating in AC magnetic fields

The feasibility of the $Co_{40}Pt_{60}$@C sample for magnetically induced heating has been investigated under applied AC magnetic field. For the sake of preparing the dispersions, carboxy methyl cellulose (CMC) has been used as a biocompatible surfactant. The particles were dispersed in a water-CMC solution using a tip sonicator for 2 minuits (10 sec. on, and 1 sec off). The concentration of the particles was chosen to be 5.5 mg/ml. The concentration of CMC in the water was approximately 5 mg/ml. AC magnetic fields with a frequency of 120 kHz and magnetic field strengths of 0-80 kA/m were applied to the highest magnetization sample. The experiment was performed as described in chapter 4. In Fig. 7.16(a), the time-dependent calorimetric measurements at different applied magnetic fields for CoPt@C nanocapsules are

shown. A heating effect has been observed at applied magnetic fields > 20 kA/m. At the maximum applied magnetic field of 80 kA/m, the heating rate reached values of 4 °C/min.

The specific absorption rate (SAR) usually displays the heating ability of a magnetic material and, therefore, the feasibility of a material for application in magnetic hyperthermia therapy. The SAR values have been calculated from the initial slope of the T versus t curves using Eq. 3.7 but here C is the heat capacity of CMC solution ($C = 4.4$ $\text{Jg}^{-1}\text{K}^{-1}$) had to be used [203]. The resulting SAR values for CoPt@C are shown as a function of the applied AC magnetic field strength are shown in Fig. 7.16(b). The observed quadratic field dependence is in agreement with the fact that the dissipated magnetic energy is proportional to H^2.

At the maximum applied magnetic field of 80 kA/m, the SAR value amount to 69 $\text{W/g}_{\text{CoPt@C}}$ for CoPt@C. This value is not large in order to be used for real application. But it can be large if the sample being chemically functionalized to get better dispersions of the magnetic nanoparticles in the liquid. In contrast there was no observable induced heating in the case of NiPt@C samples. The reason is due to the large magnetization of the CoPt@C samples in comparison to the NiPt@C samples. The relatively broad size distribution in CoPt@C sample implies both superparamagnetic and ferromagnetic particles at room temperature. However, heating mechanisms which responsible for the observed power absorption might appear concomitantly from Néel and Brownian relaxation. This is because of the behaviour of dispersed particle in liquid induce heating via the movement of the particle in the solution (Brownian relaxation) and the rotation of the entire magnetic moment of the particles (Néel relaxation).
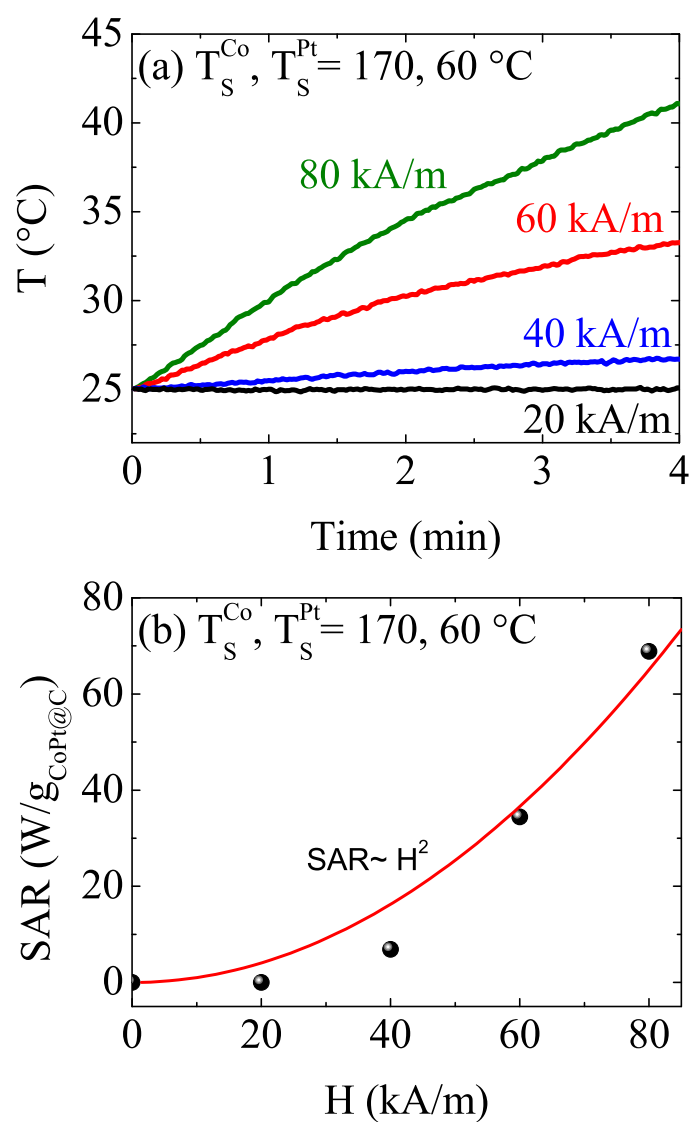
Figure 7.16: (a) Temperature vs. time upon application of AC magnetic fields, and (b) corresponding SAR values for the highest magnetization sample of CoPt@C.

7.2.3 Conclusions

NiPt@C and CoPt@C nanoalloys have been synthesized under controlled conditions using the high pressure chemical vapor deposition technique. The samples have been investigated with respect to their morphology and magnetic properties. Core/shell nanostructures of NiPt@C and CoPt@C have been formed with a controlled mean core size range from 3 to 15 nm, and 2 to 20 nm, respectively. X-ray diffraction measurements reveal NiPt and CoPt binary alloys only. It is to be particularly mentioned that the content of carbon in the deposited nanoalloy material as well as the actual Ni:Pt and Co:Pt ratio clearly depend on the synthesis sublimation temperature Also the average sizes of the nanoparticles do significantly change with the variation of the sublimation temperature. Hence the produced particle size can be controlled by monitoring the sublimation temperature of each precursor. This also directly affects the magnetic properties. The magnetization curves show ferromagnetic-like behavior at room temperature for all samples. Different values for the magnetization M(1 T) are obtained by variations in the chemical composition of the NiPt, and CoPt core but primarily caused by different carbon contents in the deposited material. The thickness of the carbon shells is relatively constant. In contrast, the mean superparamagnetic blocking temperatures are mainly associated with the changing of the particle size of the core material. This dependence has been observed from the exponential decay of the blocking temperature versus the sublimation temperature which is also inversely proportional to the particle size of the core material. In addition a relatively large anisotropy for NiPt@C and CoPt@C have been noticed from the analysis of (ZFC) magnetization curve which opens the opportunity of using this samples for the recording media applications. In order to suggest the use of CoPt@C for the medical application, their feasibility for magnetic hyperthermia therapy has been studied. This was resulting in observed induced heating under applied AC magnetic field larger than 20 kA/m.

Summary

The work at hand covers the development of new synthesis procedures for carbon coated magnetic nanoparticles and their detailed investigation with respect to potential biomedical applications. In order to achieve these aims, a novel gas phase synthesis process for carbon coated magnetic nanoparticles using a high pressure chemical vapor deposition technique has been developed. Hence, a main part of the thesis describes the synthesis of the core/shell structure with the magnetic nanoparticle as core and carbon layers as shell, protecting the magnetic core from oxidation. In addition the detailed investigation of the structural morphology, the structure, the magnetic properties, and the feasibility for hyperthermia therapy as one of the most important applications of the synthesized materials is described.

A new procedure was developed to synthesize carbon coated magnetic nanoparticles such as Fe@C, Co@C, Ni@C, FeRu@C, CoRu@C, NiRu@C, NiPt@C, and CoPt@C nanocapsules. The high pressure chemical vapor deposition technique was applied for this purpose. As material sources, different metallorganic precursors such as metallocenes (ferrocene, cobaltocene, nickelocene, ruthenocene) and trimethyl methylcyclopentadienyl platinum (IV) were chosen. These precursors have advantage that they can sublimate and decompose at relatively low temperatures. The synthesis procedures were developed via controlling three main parameters. These parameters are the temperature and the pressure inside the CVD reactor and the

sublimation temperature of the thermostated chambers.

In the case of Fe@C, Co@C, and Ni@C nanocapsules production, the temperature and pressure of the CVD reactor were varied and adjusted while the sublimation chamber temperature was fixed at 95 °C. Therefore, the optimum temperature and pressure conditions for the production of spherical Fe@C, Co@C, and Ni@C nanocapsules was found to be 900 °C and 13 bar.

These optimum conditions for the temperature and the pressure inside the CVD reactor were the limit for spherical nanostructures production. In order to extend the synthesis procedure from pure metals to alloys nanostructures production, the synthesis parameters were further developed. Actually it was found that the optimum condition of producing spherical Fe, Co, and Ni are the same optimum conditions as for alloys production. This was the case of FeRu@C, CoRu@C, and NiRu@C production. In addition the pressure inside the CVD reactor was examined within the range 13-31 bar in order to get alloys with different compositions. Therefore, according to the change in pressure, different alloy compositions of FeRu@C, CoRu@C, and NiRu@C have been obtained.

For the sake of expanding the use of HPCVD for producing more materials with controlled properties, NiPt@C, and CoPt@C nanocapsules have been synthesized. Here the temperature and the pressure inside the CVD reactor were fixed at 900°C and 13 bar, while the temperature of the sublimation chambers was changed. Therefore, various samples with different compositions were obtained.

In order to investigate the structural morphology and the magnetic properties of all the synthesized samples, many tools such as SEM, HRTEM, EDX, XRD, AGM, SQUID, and the alternating frequency generator (AFG) have been used.

In the case of Fe@C, Co@C, and Ni@C samples, the SEM and TEM studies show that carbon coated particles with a Fe, Co, and Ni core are formed with a size distribution from few to tens nanometers. X-ray diffraction was applied to confirm the phase of the core material. The size of the average core particles was deduced

from TEM and from the width of the XRD peaks to be in the range of 25 nm for all the samples. The coated nanoparticles are ferromagnetic up to 400 K. AC magnetic heating studies of the dispersed nanoparticles yield a maximum SAR of 162 $W/g_{Co@C}$ and 131 $W/g_{Ni@C}$ at 80 kA/m and 120 kHz. The corresponding heating rates amount to 7 °C/min and 11 °C/min for Co@C and Ni@C, respectively.

For carbon coated FeRu, CoRu, and NiRu nanoalloys samples, core/shell nanostructures and the alloy's composition were revealed from the analysis of our HRTEM and EDX data. X-ray diffraction studies reveal FeRu, CoRu, NiRu binary alloys and no related oxidized metals. The average particle sizes were determined from HRTEM and XRD to be 9, 6, and 6 nm for FeRu, CoRu, and NiRu respectively. It is worth mentioning that the content of carbon in the deposited nanoalloy material clearly depends on the synthesis pressure while the average sizes of the nanoparticles do not significantly change. Hence, this leads to control of the composition of the produced alloys by controlling the pressure during the synthesis process. This uprightly affects the magnetic properties, too. For FeRu@C and CoRu@C samples, the magnetization curves show ferromagnetic behaviour, while for NiRu@C samples, ferromagnetic-like behavior was found for samples prepared at the lowest pressure and typical superparamagnetic behaviour for the sample made at highest pressure. Different values for the saturation magnetization were obtained for different chemical composition of the alloy core but primarily are caused by different carbon contents in the deposited material. On the other hand, the mean superparamagnetic blocking temperatures are mainly associated with the changing of the chemical composition of the core material. A large anisotropy was noted from the analysis of the (ZFC) magnetization curve of NiRu nanoalloys. The AC heating studies for the dispersed NiRu@C sample displayed induced heat inside the sample solution which yields a SAR of 23 $W/g_{NiRu@C}$ at 80 kA/m.

In the last part of the thesis, the investigated properties of carbon coated NiPt and CoPt nanoalloys were discussed. The core/shell nanostructures of NiPt@C and

CoPt@C have been formed with a controlled mean core size range from 3 to 15 nm, and 2 to 20 nm, respectively. X-ray diffraction measurements reveal NiPt and CoPt binary alloys only. It is to be particularly mentioned that the content of carbon in the deposited nanoalloy material and the average particle sizes as well as the actual Ni:Pt, and Co:Pt ratio clearly depend on the synthesis sublimation temperature. Also the average sizes of the nanoparticles do significantly change with the variation of the sublimation temperature. Hence the produced particle size can be controlled by monitoring the sublimation temperature of each precursor. This also directly affects the magnetic properties. The magnetization curves showed ferromagnetic-like behavior at room temperature for all samples. Different values for the magnetization are affected by variations in the chemical composition of the NiPt, and CoPt core but are primarily caused by different carbon contents in the deposited material. In contrast, the mean superparamagnetic blocking temperatures are mainly associated with the changing of the particle size of the core material. This dependence has been observed from the exponential decay of the blocking temperature versus the sublimation temperature which is also inversely proportional to the particle size of the core material. In addition a relatively large anisotropy for NiPt@C and CoPt@C was noticed from the analysis of the (ZFC) magnetization curve which opens the opportunity of using these samples for recording media applications. In order to test the feasibility of CoPt@C for magnetic hyperthermia therapy, AC heating studies for the dispersed CoPt@C were conducted. Induced heating under applied AC magnetic field larger than 20 kA/m was observed. Hence, due to the particular magnetic properties of NiPt, and CoPt nanoalloys, their small particle size, narrow size distribution, high magnetocrystaline anisotropy and uniform coating by carbon shells, these materials are a promising candidate for industrial and biomedical applications such as magnetic data storage, magnetic hyperthermia and contrast agent for magnetic resonance imaging.

Bibliography

[1] Chen JP, Sorensen CM, Klabunde KJ, and Hadjipanyis GC. Phys. Rev. B 1995, 51, 11527.

[2] Wolf EL. Nanophysics and Nanotechnology an Introduction to Modern Concepts in Nanoscience. Wiley-VCH Verlag GmbH Co. 2004.

[3] Schmid G, Talapin DV, and Shevchenko EV. Nanoparticles: From Theory to Application, ed. G. Schmid. Wiley- VCH Verlag, Weinheim 2004.

[4] Klabunde KJ. Nanoscale Materials in Chemistry. John Wiley & Sons Inc. 2001.

[5] Berry CC. J. Mater. Chem., 2005, 15, 543.

[6] Tartaj P, Morales M.P, González-Carreño T, Veintemillas-Verdaguer S, Serna CJ. J. Magn. Magn. Mater. 2005, 290-291, 28.

[7] Megens M and Prins M. J. Magn. Magn. Mater. 2005, 293, 702.

[8] Owens FJ, Introduction to Nanotechnology. Wiley 2003.

[9] Kirschvink JL, Kobayashi AK, Woodford BJ. Proc. Natl. Acad. Sci. 1992, 89, 7683.

[10] Jeong U, Teng X, Wang Y, Yang H, Xia Y. Adv. Mater. 2007, 19, 33.

[11] Blundell S. Magnetism in condensed matter, Oxford university press, UK 2001.

[12] Getzlaff M. Fundamentals of magnetism, Springer-verlag, Berlin, 2008.

[13] Mathew DS, and Juang R-S. Chem. Eng. J. 2007, 129, 51.

[14] Morrish AH. The Physical Principles of Magnetism, Wiley, New York 1965.

[15] Lu A-H, Salabas EL, Schüth F. Angew. Chem. Int. Ed. 2007, 46, 1222.

[16] Skomski R and Coey JMD. Permanent Magnetism. Institute of Physics Publishing, Bristol and Philadelphia 1999.

[17] Cullity BD. Introduction to Magnetic Materials. Addison-Wesley Publishing CompanyReading MA 1972.

[18] Spaldin NA. Magnetic materials. Campredge university press 2003.

[19] Néel LCR. Acad. Sci. 1949, 228, 664.

[20] Bean CP. J. Appl. Phys. 1955, 26, 1381.

[21] Majetich SA, Sachan M. J. Phys. D: Appl. Phys. 2006, 39, R407.

[22] Frey NA, Peng S, Cheng K, and Sun S. Chem. Soc. Rev. 2009, 38, 2532.

[23] Stoner EC, Wohlfarth EP. Philos Trans R Soc London, Ser A 1948, 240:599-642.

[24] Bedanta S and Kleemann W. J. Phys. D: Appl. Phys. 2009, 42, 013001.

[25] Jordan A. J. Nano. Part. Res. 2003, 5, 597.

[26] Pankhurst QA, Connolly J, Jones SK, Dobson J. J. Phys. D: Appl. Phys. 2003, 36, R167.

[27] Hansen MF and Morup S. J. Magn. Magn. Mater. 1999, 203, 214.

[28] Hanson M, Johansson C, and Morup S. J. Phys. Condens. Matter. 1995, 7, 9263.

[29] Dormann JL, Fiorani D and Tronc E. Adv. Chem. Phys. 1997, 98, 283.

[30] Chikazumi S. Physics of Ferromagnetism. Oxford University Press, New York 1999.

[31] Farle M. Rep. Prog. Phys. 1998, 61, 755.

[32] Chikazumi S. Physics of Magnetism. Robert E. Kriger Publishing Company Malabar, Florida 1964.

[33] Chen C. Magnetism and Metallurgy of Soft Magnetic Materials, Dover Publications, Inc. New York 1986.

[34] Scheinfein MR, Schmidt KE, Heim KR and Hembree GG. Phys. Rev. Lett. 1996, 76, 1541.

[35] Ruderman MA and Kittel C. Phys. Rev. 1954, 96, 99.

[36] Dormann JL, Cherkaoui R, Spinu L, Nogue´s M, Lucari F, D´orazio F, Fiorani D, Garcia A, Tronc E, and Jolivet JP. J. Magn. Magn. Mater. 1998, 187, L139.

[37] Weller D, and Doerner ME. Annu. Rev. Mater. Sci. 2000, 30, 611.

[38] Sun S, Murray CB, Weller D, Folks L, Moser A. Science 2000, 287, 1989.

[39] Li J, Wang ZL, Zeng H, Sun S, Liu JP. Appl. Phys. Lett. 2003, 82, 3743.

[40] Pankhurst QA, Thanh NKT, Jones SK, Dobson J. J. Phys. D: Appl. Phys. 2009, 42, 224001.

[41] Puntes VF, Krishnan KM, and Alivisatos AP. Science, 2001, 291, 2115.

[42] Liu G, Yan X, Lu Z, Curda SA, and Lal J. Chem. Mater. 2005, 17, 4985.

[43] Murray CB, Sun S, Doyle H, and Betley T. MRS Bulletin, 2001, 26, 985.

[44] Lisiecki I and Pileni MP. Langmuir. 2003, 19, 9486.

[45] Frommen C, Rösner H, Fenske D. J. Nanosci. Nanotech. 2002, 2, 509.

[46] Shevchenko EV, Talapin DV, Rogach AL, Kornowski A, Haase M, Weller H. J. Am. Chem. Soc. 2002, 124, 11480.

[47] Wang Y and Yang H. J. Am. Chem. Soc. 2005, 127, 5316.

[48] Ely TO, Pan C, Amiens C, Chaudret B, Dassenoy F, Lecante P, Casanove M-J, Mosset A, Respaud M, Broto J-M. J. Phys. Chem. B. 2000, 104, 695.

[49] Klem MT, et al. Adv. Funct. Mater., 2005. 15: p. 1489-1494.

[50] Park S-J, Kim S, Lee S, Khim Z, Char K, Hyeon T. J. Am. Chem. Soc. 2000, 122, 8581.

[51] Sun X, Gutierrez A, Yacaman MJ, Dong X, Jin S. Mater. Sci. Eng. A 2000, 286, 157.

[52] Neveu S, Bee A, Robineau M, Talbot D. J. Colloid Interface Sci. 2002, 255, 293.

[53] Grasset F, Labhsetwar N, Li D, Park DC, Saito N, Haneda H, Cador O, Roisnel T, Mornet S, Duguet E, Portier J, Etourneau J. Langmuir. 2002, 18, 8209.

[54] Sun S and Zeng H. J. Am. Chem. Soc. 2002, 124, 8204.

[55] Hu J, Lo IMC, Chen G. Sep. Purif. Technol. 2007, 56, 249.

[56] Park J, An K, Hwang Y, Park J-G, Noh H-J, Kim J-Y, Park J-H, Hwang N-M, Hyeon T. Nat. Mater. 2004, 3, 891.

[57] Pellegrino T, Manna L, Kudera S, Liedl T, Koktysh D, Rogach AL, Keller S, Rädler J, Natile G, Parak WJ. Nano Letters, 2004, 4, 703.

[58] Hong R, Fischer NO, Emrick T, Rotello VM. Chem. Mater. 2005, 17, 4617.

[59] Kim BS, Qiu J-M, Wang J-P, Taton TA. Nano Letters. 2005, 5, 1987.

[60] Lazzari M and Lopez-Quintela MA. Adv. Mater. 2003, 15, 1583.

[61] Wasa K, Kitabatake M, and Adachi H. Thin film materials technology: sputtering of compound materials, Publisher William Andrew, New York 2004.

[62] Elshabini-Riad A, and Barlow F D. Thin Film Technology Handbook, McGraw-Hill, New York 1997.

[63] Murray CB, Kagan CR, and Bawendi MG. Ann. Rev. Mater. Sci. 2000, 30, 545.

[64] LaMer VK, and Dinegar RH. J. Am. Chem. Soc. 1950, 72, 4847.

[65] Iida H, Takayanagi K, Nakanishi T, and Osaka T. J. Coll. Inter. Sci. 2007, 314, 274.

[66] Liu ZL, Wang HB, Lu QH, Du GH, Peng L, Du YQ, Zhang SM, Yao KL. J. Magn. Magn. Mater. 2004, 283, 258.

[67] Lopez Perez JA, Lopez Quintela MA, Mira J, Rivas J, Charles SW. J. Phys. Chem. B. 1997, 101, 8045.

[68] Dresco PA, Zaitsev VS, Gambino RJ, Chu B. Langmuir. 1999, 15, 1945.

[69] Liu C, Zou B, Rondinone AJ, Zhang ZJ. J. Phys. Chem. B. 2000, 104, 1141.

[70] Santra S, Tapec R, Theodoropoulou N, Dobson J, Hebard A, Tan W. Langmuir. 2001, 17, 2900.

[71] Vidal-Vidal J, Rivas J, López-Quintela MA. Coll. Surf. A. 2006, 288, 44.

[72] Chen Y, Peng D-L, Lin D, and Luo X. Nanotechnology. 2007, 18, 505703.

[73] Davar F, Fereshteh Z, Salavati-Niasari M. J. Alloys Compd. 2009, 476, 797.

[74] Hyeon T, Lee SS, Park J, Chung Y, Na HB. J. Am. Chem. Soc. 2001, 123, 12798.

[75] Kwon SG, Piao Y, Park J, Angappane S, Jo Y, Hwang N-M, Park J-G, Hyeon T. J. Am. Chem. Soc. 2007, 129, 12571.

[76] Tokoro H, Fujiia S, Oku T. J. Mater. Chem. 2004, 14, 253.

[77] Yelsukov EP, Ul´yanov AI, Zagainov AV, and Arsent´yeva NB. J. Magn. Magn. Mater. 2003, 513, 258.

[78] Zalich MA, Baranauskas VV, Riffle JS, Saunders M, and Pierre TGST. Chem. Mater. 2006, 18, 2648.

[79] Borysiuk J, Grabias A, Szczytko J, Bystrzejewski M, Twardowski A, Lange H. Carbon 2008, 46, 1693.

[80] Bystrzejewski M, Huczko A, Lange H, Cudzi´o S, Kicínski W. Diamond Relat. Mater. 2007, 16, 225.

[81] Martirosyan KS, Chang L, Rantschler J, Khizroev S, Luss D, Litvinov D. IEEE Trans. Magn. 2007, 43, 157.

[82] Stark WJ and Pratsinis SE. Powder Technol. 2002, 126, 103.

[83] Pierson HO. Handbook of Chemical Vapor Deposition: Principles, Technology and Applications, William Andrew Inc. 1999.

[84] Tavakoli A, Sohrabi M, and Kargari A. Chem. Pap. 2007, 61, 151.

[85] Powell C, Oxley J, and Blocher J. Vapor Deposition, John Wiley & Sons, New York 1966.

[86] Flahaut E, Agnoli F, Sloan J, O´Connor C, Green MLH. Chem. Mater. 2002, 14, 2553.

[87] Wang ZH, Choi CJ, Kim BK, Kim JC, Zhang ZD. Carbon 2003, 41, 1751.

[88] Liu BH, Ding J, Zhong ZY, Dong ZL, White T, Lin JY. Chem. Phys. Lett. 2002, 358, 96.

[89] Dravid VP, Host JJ, Teng MH, Eillott B, Hwang JH, Johnson DL. Nature. 1995, 374, 602.

[90] Hirano T, Oku T, and Suganuma K. Diamond Related Mater. 2000, 9, 476.

[91] Morales MP, Bomati-Miguel O, Perez de Alejo R, Ruiz-Cabello J, Veintemillas-Vendaguer S, Ogrady K. J. Magn. Magn. Mater. 2003, 102, 266.

[92] Ye E, Liu B, and Fan WY. Chem. Mater. 2007, 19, 3845.

[93] Park JB, Jeong SH, Jeong MS, Kim JY, Cho BK. Carbon 2008, 46, 1369.

[94] McDonald JE. Am. J. Phys. 1962, 30, 870.

[95] McDonald JE. Am. J. Phys. 1963, 31, 31.

[96] Ohring M. The materials science of thin films: deposition and structure, Academic Press, San Diego, CA 2002.

[97] Lieser KH. Angew. Chem. Internat. Ed. 1969, 8, 188.

[98] Sun S, and Murray CB. J. Appl. Phys. 1999, 85, 4325.

[99] Zhang Q, Wang C, Qiao L, Yan H, Liu K. J. Mater. Chem. 2009, 19, 8393

[100] Farrell D, Majetich SA, and Wilcoxon JP. J. Phys. Chem. B. 2003, 107, 11022.

[101] Bönnemann H, Brijoux W, Brinkmann R, Matoussevitch N, Waldoefner N, Palina N, Modrow H. Inorg. Chim. Acta 2003, 350, 617.

[102] Chen C-T, Chen Y-C. Anal. Chem. 2005, 77, 5912.

[103] Lo C-Y, Chen W-Y, Chen C-T, Chen Y-C. J. Proteome Res. 2007, 6, 887.

[104] Chen C-T, Chen W-Y, Tsai P-J, Chien K-Y, Yu J-S, Chen Y-C. J. Proteome Res. 2007, 6, 316.

[105] Shukla R, Bansal V, Chaudhary M, Basu A, Bhond RR, Sastry M. Langmuir 2005, 21, 10644.

[106] Sun Q, Wang Q, Rao BK, and Jena P. Phys. Rev. Lett. 2004, 93, 186803.

[107] Rivas J, Sánchez RD, Fondado A, Izco C, GarcYa-Bastida AJ, García-Otero J, Mira J, Baldomir D, González A, Lado I, López-Quintela MA,Oseroff SB. J. Appl. Phys. 1994, 76, 6564.

[108] Park J-I, and Cheon J. J. Am. Chem. Soc. 2001, 123, 5743.

[109] Sun Q, Reddy BV, Marquez M, Jena P, Gonzalez C, Wang Q. J. Phys. Chem. C 2007, 111, 4159.

[110] Lu Y, Yin Y, Mayers BT, and Xia Y. Nano Lett. 2002, 2, 183.

[111] Scott JH and Majetich SA. Phys. Rev. B. 1995, 52, 12564.

[112] Teng MH, Tsai SW, Hsiao CI, and Chen YD. J. Alloys Compd. 2007, 678, 434.

[113] Todorovic M, Schultz S, Wong J, and Scherer A. Appl. Phys. Lett. 1999, 74, 2516.

[114] Horng HE, Hong C-Y, Yang SY, Yang HC. J. Phys. Chem. Solids 2001, 62, 1749.

[115] Zboril R, Mashlan M, and Petridis D. Chem. Mater. 2002, 14, 969.

[116] Teja AS and Koh P-Y. Prog. Crys. Growth Char. Mater. 2009, 55, 22.

[117] Cornell RM and Schwertmann U. The Iron Oxides: Structure, Properties, Reactions, Occurrences and Uses, 2th ed., Wiley-VCH, Weinheim 2003.

[118] Lam UT, Mammucari R, Suzuki K, and Foster NR. Ind. Eng. Chem. Res. 2008, 47, 599.

[119] Ang KH, Alexandrou I, Mathur ND, Amaratunga GAJ, Haq S. Nanotechnology 2004, 15, 520.

[120] Sun Y, Li X, Cao XJ, Zhang W, Wang HP. Adv. Colloid Interface Sci. 2006, 120, 47.

[121] Tratnyek PG and Johnson R.L. Nanotoday 2006, 1, 44.

[122] Zhang W-X. J. Nanopart. Res. 2003, 5, 323.

[123] Blowes DW, Ptacek CJ, Benner SG, McRae Che WT, Bennett TA, Puls RW. J. Contam. Hydrol. 2000, 45, 123.

[124] LaConte L, Nitin N, and Bao G. Mater. Today 2005, 8, 32.

[125] Jeong U, Teng X, Wang Y, Yang H, Xia Y. Adv. Mater. 2007, 19, 33.

[126] Rosengart AJ, Kaminski MD, Chen H, Caviness PL, Ebner AD, Ritter JA. J. Magn. Magn. Mater. 2005, 293, 633.

[127] Berry CC, Curtis ASG. J. Phys. D: Appl. Phys. 2003, 36, R198.

[128] Kim EH, Lee HS, Kwak BK, and Kim B-K. J. Magn. Magn. Mater. 2005, 289, 328.

[129] Wu J, Ye Z, Wang G, and Yuan J. Talanta 2007, 72, 1693.

[130] Yanase M, Shinkai M, Honda H, Wakabayashi T, Yoshida J, Kobayashi T. Japan. J. Cancer Res. 1998, 89, 463.

[131] Chan DCF, Kirpotin DB, Bunn PA. J. Magn. Magn. Mater. 1993, 122, 374.

[132] Jordan A, Scholz R, Wust P, Fahling H, Felix R. J. Magn. Magn. Mater. 1999, 201, 413.

[133] Karmakar S, Sharma SM, Mukadam MD, Yusuf SM, Sood AK. J. Appl. Phys. 2005, 97, 054306.

[134] Johannsen M, Gneveckow U, Taymoorian K, Thiesen B, Waldoefner N, Scholz R, Jung K, Jordan A,Wust P, and Loening SA. Int. J. of Hyperthermia 2007, 23, 315.

[135] Rosensweig R. J. Magn. Magn. Mater. 2002, 252, 370.

[136] Debye P. Polar Molecules. The Chemical Catalog Company, New York 1929.

[137] Hergt R, Hiergeist R, Hilger I, Kaiser W, Lapatnikov Y, Margel S, Richter U. J. Mag. Mag. Mater. 2004, 270, 345.

[138] Hiergeist R, Andra W, Buske N, Hergt R, Hilger I, Richter U, Kaiser W. J. Mag. Mag. Mater. 1999, 201, 420.

[139] Ramprasad R, Zurcher P, Petras M, Renaud P, and Miller M. J. Appl. Phys. 2004, 96, 519.

[140] Hergt R, Dutz S, Muller R, and Zeisberger M. J. Phys.: Cond. Matter, 2006, 18, S2919.

[141] Lao L and Ramanujan V. J. Mater. Sci.: Mater. Med. 2004, 15, 1061.

[142] Hergt R. and Dutz S. J. Mag. Mag. Mater. 2007, 311, 187 .

[143] Jordan A, Scholz R, Maier-Hauff K, Johannsen M, Wust P, Nadobny J, Schirra H, Schmidt H, Deger S, Loening S, Lanksch W, Felix R. J. Mag. Mag. Mater. 2001, 225, 118.

[144] Landeghem Fv, Maier-Hauff K, Jordan A, Hoffman K, Gneveckow U, Scholz R, Thiesen B, Bruck W, von Deimling A. Biomaterials 2009, 30, 52.

[145] Hergt R, Dutz S, and Roder M. J. Phys.: Cond. Matter 2008, 20, 1.

[146] Ma M, Wu Y, Zhou J, Sun Y, Zhang Y, Gu N. J. Mag. Mag. Mater. 2004, 268, 33.

[147] Wada S, Tazawa K, Furuta I, and Nagae H. Oral Diseases, 2003, 9, 218.

[148] Dutz S, Clement J, Eberbeck D, Gelbrich T, Hergt R, Müller R, Wotschadlo J, and Zeisberger M. J. Mag. Mag. Mater. 2009, 321, 1501.

[149] Glockl G, Hergt R, Zeisberger M, Dutz S, Nagel S, Weitschies W. J. Phys.: Cond. Matter 2006, 18, S2935.

[150] Nikolaev P, Bronikowski MJ, Bradley RK, Rohmund F, Colbert DT, Smith KA, Smalley RE. Chem. Phys. Lett. 1999, 313, 91.

[151] Barreiro A, Hampel S, Ruemmeli MH, Kramberger C, Grüneis A, Biedermann K, Leonhardt A,Gemming T, Büchner B, Bachtold A, Pichler T. J. Phys. Chem. B 2006, 110, 20973.

[152] Khavrus VO, Ibrahim EMM, Leonhardt A, Hampel S, Oswald S, Tschner C, Büchner B. J. Phys. Chem. C 2010, 114, 843.

[153] Edelstein AS and Cammarata RC. Nanomaterials: Synthesis, Properties and Applications. IOP Publishing Ltd. 1996

[154] Patterson AL. Phys. Rev. Lett. 1939, 56, 978.

[155] Kuramochi H, Akinaga H, Semba Y, Kijima M, Uzumaki T, Yasutake M, Tanaka A , Yokoyama H. Jpn. J. Appl. Phys. 2005, 44, 2077.

[156] Fonseca FC, Ferlauto AS, Alvarez F, Goya GF, Jardin RF. J. Appl. Phys. 2005, 97, 044313-1.

[157] Wang H, Wong SP, Cheung WY, Ke N, Chiah MF, Liu H, Zhang XX. J. Appl. Phys. 2000, 88, 2063.

[158] Delaunay JJ, Hayashi T, Tomita M, Hirono S, Umemura S. Appl. Phys. Lett. 1997, 71, 3427.

[159] Vyalikh A, Wolter A, Hampel S, Haase D, Ritschel M, Leonhardt A, Grafe H-J, Taylor A, Krämer K, Büchner B, Klingeler R. Nanomedicine 2008, 3, 321.

[160] Taylor A, Kraemer K, Hampel S, Fuessel S, Klingeler R, Ritschel M, Büchner B, Grimm MO, Wirth MP. The Journal of Urology 2008, 179, Nr. 4, Supplement, S. 392.

[161] Dobson J. Gene Ther. 2006, 13, 283.

[162] Grundy PJ. J. Phys. D: Appl. Phys. 1998, 31, 2975.

[163] Weller D and Moser A. IEEE Trans. Magn. 1999, 35, 4423.

[164] Robinson I, Zacchini S, Tung LD, Maenosono S, Thanh NTK. Chem. Mater. 2009, 21, 3021.

[165] Sun SH, Anders S, Hamann HF, Thiele JU, Baglin JEE, Thomson T, Fullerton EE, Murray CB, Terris BDJ. Am. Chem. Soc. 2002, 124, 2884.

[166] Sun SH, Fullerton EE, Weller D, and Murray CB. IEEE Trans. Magn. 2001, 37, 1239.

[167] Kiely CJ, Fink J, Zheng JG, Brust M, Bethell D, Schiffrin D. J. Adv. Mater. 2000, 12, 640.

[168] Li Y, Zhang XL, Qiu R, Qiao R, Kang YS. J. Phys. Chem. C 2007,111, 10747.

[169] Mandal M, Kundu S, Ghosh S K , Sau TK, Yusuf SM , Pal T. J. Coll. Inter. Sci. 2003, 265, 23.

[170] Mandal M, Kundu S, Tapan K. Sau TK, Yusuf SM , Pal T. Chem. Mater. 2003, 15, 3710.

[171] Rosensweig RE. Chem. Eng. Prog. 1989, 85, 53.

[172] Sounderya N and Zhang Y. Use of Core/Shell Structured Nanoparticles for Biomedical Applications. Recent Patents on Biomedical Engineering 2008, 1, 34.

[173] Lu AH, Li EC, Matoussevitch N, Spliethof B, Bönnemann H, Schüth F. Chem Commun 2005, 1, 98.

[174] Host JJ, Block JA, Parvin K, Dravid VP, Alpers JL, Sezen T, Laduca R. J. Appl. Phys. 1998, 83, 793.

[175] Makarewicz M, Podsiadly M, and Balanda M. Acta Physica Polonica A. 2009, 115, 568.

[176] He CN, Du XW, Ding J, Shi CS, Li JJ, Zhao NQ, Cui L. Carbon 2006, 44, 2330.

[177] Li H, Zhao N, He C, Shi C, Du X, Li J. J. Alloys and Compounds 2008, 458, 130.

[178] Liu X, Gurel V, Morris D, Murray D, Zhitkovich A, Kane AB, Hurt RH. Adv. Mater. 2007, 19, 2790.

[179] Guo L, Morris D, Liu X, Vaslet C, Hurt RH, Kane AB. Chem. Mater. 2007, 19, 3472.

[180] Taylor A, Lipert K, Krämer K, Hampel S, Füssel S, Meye A, Klingeler R, Ritschel M, Leonhardt A, Büchner B, Wirth MP. J. Nanosci. and Nanotech. 2009, 9, 1.

[181] Vittorioa O, Raffaa V, and Cuschieria A. Nanomedicine: Nanotechnology, Biology and Medicine 2009, 5, 424.

[182] Harris PJF and Tsang SC. Chem. Phys. Lett. 1998, 293, 53.

[183] Klingeler R, Hampel S, Büchner B. Int. J. Hyperthermia 2008, 24, 496.

[184] Klingeler R and Sim RB. Carbon Nanotubes for Biomedical Applications. Springer 2011.

[185] Johannsen M, Gneveckow U, Taymoorian K, Thiesen B, Waldöfner N, Scholz R, Jung K, Jordan A, Wust P, Loening SA. Int. J. Hyperthermia 2007, 23, 315.

[186] El-Gendy A A, Ibrahim EMM, Khavrus VO, Krupskaya Y, Hampel S, Leonhardt A, Büchner B, Klingeler R. Carbon 2009, 47, 2821.

[187] Heremans J, Olk CH, and Morelli DT. Phys. Rev. B 1994, 49, 15122.

[188] Lipert K, Kretzschmar F, Ritschel M, Leonhardt A, Klingeler R, Büchner B. J. Appl. Phys. 2009, 105, 063906-1.

[189] Herzer G. J. Magn. Magn. Mater. 1992, 112, 258.

[190] Luborsky FE. J. Appl. Phys. 1961, 32, S171.

[191] Ma M, Wu Y, Zhou J, Sun Y, Zhang Y, Gul N. J. Magn. Magn. Mater. 2004, 268, 33.

[192] Majetich SA, Scott JH, Kirkpatrick EM, Chowdary K, Gallagher K, McHenry ME. Nanostr. Mater. 1997, 9, 291.

[193] Zhang XX, Hernandez JM, Tejada J, Sole R, Ruiz X. Phys. Rev. B 1996, 53, 3336.

[194] Andrä W and Nowak H. Magnetism in Medicine, A Handbook, 2nd ed. Wiley-VCH 2007.

[195] Tejada J, Ziolo RF, and Zhang XX. Chem. Mater. 1996, 8, 1784.

[196] El-Gendy AA, Khavrus VO, Hampel S, Leonhardt A, Büchner B, Klingeler R. J. Phys. Chem. C 2010, 114, 10745.

[197] Glaspell G, Abdelsayed V, Saoud KM, El-Shall MS. Pure Appl. Chem. 2006, 78, 1667.

[198] Crangle J and Parsons D. Proceedings of the Royal Society of London. Series A, Mathematical and Physical Sciences 1960, 255, 509.

[199] Binder K and Young AP. Rev. Mod. Phys. 1986, 58, 801.

[200] Peng DL, Chena Y, Shea H, Katoh R, Sumiyama K. J. Alloys and Compounds 2009, 469, 276.

[201] Ammar S, Helfen A, Jouini N, Fievet F, Rosenman I, Villain F, Molinie P, Danot M. J. Mater. Chem. 2001, 11, 186.

[202] Hergt R, Dutz S, and Zeisberger M. Nanotechnology 2010, 21, 015706.

[203] Semmar N, Tanguier JL, and Rigo MO. Thermochimica Acta 2003, 402, 225.

List of Publications

- M.U. Lutz, K. Lipert, Y. Krupskaya, S. Bahr, A. Wolter, **A. A. El-Gendy**, S. Hampel, A. Leonhardt, A. Taylor, K. Kraemer, B. Buechner, R. Klingeler. Feasibility of magnetically functionalised carbon nanotubes for biological applications: From fundamental properties of individual nanomagnets to nanoscaled heaters and temperature sensors, in: Carbon Nanotubes for Biomedical Applications, R. Klingeler, R.B. Sim (eds.), Springer-Verl. (2011), 97-124.

- **A. A. El-Gendy**, V.O. Khavrus, S. Hampel, A. Leonhardt, B. Büchner, R. Klingeler. Morphology, structural control, and magnetic properties of carbon-coated nanoscaled NiRu- alloys. Journal of Physical Chemistry C (2010) 114, 10745.

- **A. A. El-Gendy**, E.M.M. Ibrahim, V.O. Khavrus, Y. Krupskaya, S. Hampel, A. Leonhardt, B. Büchner, R. Klingeler. The synthesis of carbon coated Fe, Co and Ni nanoparticles and an examination of their magnetic properties. Carbon (2009) 47, 2821.

Acknowledgements

Pursuing a PhD project is a both painful and enjoyable experience. It's just like climbing a high peak, step by step, accompanied with bitterness, hardships, frustration, encouragement and trust, and with so many people's kind help. When I found myself at the top enjoying the beautiful scenery, I realized that it was, in fact, teamwork that got me there. Though it will not be enough to express my gratitude in words to all those people who helped me, I would still like to give my many, many thanks to all these people.

First of all, I would like to give my sincere thanks to my supervisor, Prof. Rüdiger Klingeler, who accepted me as PhD student in his group without any hesitation. Thereafter, he offered me so much advice, patiently supervising me, and always guiding me in the right direction. His friendly soul has motivated me all the time to finish my work with the best way. I have learned a lot from him, without his help I could not have finished my dissertation successfully. His encouragement and continuous support made me feel confident to fulfill my desire and to overcome every difficulty I encountered. It is not sufficient to express my gratitude with only a few words.

Special thanks are also given to Prof. Bernd Büchner. He is the one who invited me to work and finish my PhD studies at IFW-Dresden. His continuous support, advices, and suggested ideas have led me to get nice results. His encouraging words

help.

Special thanks to my friend and my colleague, Matthias Lutz, his help for language check of some parts of my dissertation enabled me to present it more fluently and clearly.

My sincere thanks go to all magnetism and CVD group members at IFW-Dresden.

I give my sincere thanks to my friends inside and outside Germany, Ehab, Mohamed, Mohamed, Alexey, Kristofer, Diana, Kamil, Anja, Carsten, Sebastian, Carmen, Arthur, Vijay, Peter, Hanene, Ahmed, Shady, Ashraf, Tamer, Akram, Ayman, Ayman, and Rafael, just for being friends, which is invaluable.

I would like to convey my heartfelt thanks to my parent, sister, and niece. Their understanding and their love encouraged me to work hard and to continue pursuing a Ph.D. project abroad. Special thanks go to my father who is the closest person to my heart. His kind-hearted personality has affected me to be steadfast and never bend to difficulty and he always lets me know that he is proud of me which motivates me to work harder and do my best.

Last but not least, I am greatly indebted to my wife Mai and my son Omar. They form the backbone and origin of my happiness. Their love and support without any complaint or regret has enabled me to complete this PhD project. Being both a father and mother while I was busy with writing my thesis was not an easy thing for my wife. She took every responsibility and suffered all the bitterness to take care of my son and my family. She created quite and nice atmosphere in order to enable me to concentrate on my research. I owe my every achievement to both of them.

Ahmed El Gendy

Heidelberg June 2011